Formation of seasonal upper-ocean stratification and its variability

	Yamaguchi Ryohei
	Tohoku University
	11301 18441
URL	http://hdl.handle.net/10097/00128432

博 士 論 文

Formation of seasonal upper-ocean stratification and its variability

（海洋表層における季節成層の形成とその変動性）

山 口 凌 平

平成 30 年

Doctoral Thesis

Formation of seasonal upper-ocean stratification and its variability

海洋表層における季節成層の形成とその変動性

Ryohei Yamaguchi
（山口 凌平）

Department of Geophysics
Graduate School of Science
Tohoku University

Thesis Committee Members

Professor Toshio Suga (Chair, Supervisor)
Professor Shuji Aoki
Professor Kelvin J. Richards
　　　　　(University of Hawai'i at Mānoa)
Professor Bo Qiu
　　　　　(University of Hawai'i at Mānoa)
Associate Professor Shoichi Kizu
Associate Professor Futoki Sakaida
Associate Professor Shusaku Sugimoto

2018

Abstract

In the upper ocean from the surface to several hundred meters, there is a predominant seasonal cycle of the vertical structure of the temperature and salinity, and thus the density stratification. During the warming season, the upper-ocean seasonal stratification develops on the winter surface mixed layer (ML) formed by convection due to surface cooling. Stabilizing the upper-ocean water column, the seasonal stratification regulates the vertical exchange of water and, therefore, plays an important role in the air-sea interaction during the warming season and also on the biogeochemical processes of the upper ocean. Although the seasonality of the upper-ocean stratification is ubiquitous from low to high latitudes in the global ocean, the characteristics such as the amplitude of the seasonality and the depth range where the seasonality is evident are remarkably different depending on the ocean region.

Historically, studies about the physical processes in the upper ocean have progressed mainly focusing on the surface ML processes, because the thickness of the ML that provides the thermal and mechanical temporary inertia with regard to oceanic direct response to the atmospheric forcing is important for understanding ocean's behavior. On the other hand, the formation of the seasonal stratification under the thin summertime ML, including various physical processes, has been poorly understood. Although some fundamental processes of the formation of the seasonal stratification have been studied based on numerical models with the recently enhanced performances of computers, its quantitative observational descriptions for comparison with the model studies have been scarcely done, especially in the open ocean where the time series data with high vertical resolution are hard to be obtained. For that reason, in the present dissertation, I addressed to clarify the mechanism of the development of the seasonal stratification quantitatively from the observational dataset (Chapter 2). Moreover, I also aimed to obtain a better understanding of the roles of the upper-ocean stratification in the climate systems through investigating its long-term change and interannual/decadal variability (Chapter 3 and 4).

In Chapter 2, through quantification of the strength of the seasonal stratification using the Potential Energy Anomaly (PEA; required energy to make the density stratified water column vertically homogeneous), I described the development of the stratification quantitatively with use of the time-dependent equation of PEA. In the North Pacific, the PEAs computed from the temperature and salinity profiles collected by the Argo floats show the regional differences in the amplitude and phase of the development of the seasonal stratification. I performed the PEA budget

analysis to clarify which processes dominantly contribute to the development and how those processes are balanced. As a result, I found that the seasonal stratification develops, in a large part of the North Pacific, under a vertical one-dimensional balance between the creation by the atmospheric buoyancy forcing and the destruction by the vertical mixing in the water column. During the warming season when the vertical mixing is considered to be much weaker than the cooling season, estimated vertical diffusivities indicate the occurrence of strong mixing in the seasonal stratification, reaching the order of 10^{-4} m^2 s^{-1}, and show significant spatial and seasonal variability. On the other hand, the contribution from lateral process is significant in limited regions. PEA advection and vertical shear of horizontal current contribute to the development of the stratification in the Kuroshio Extension region and the region of the trade wind.

From the comparison of PEA budgets in two regions which have the similar total buoyancy gain in the North Pacific, I demonstrated that spatial distribution of the "composition" of buoyancy forcing, in addition to the "total magnitude", is important for producing the regional difference in the development of the seasonal stratification. In the case of the North Pacific, it the condition, satisfied in its northern part, that both the penetrating component (shortwave radiation) and the non-penetrating components (other buoyancy fluxes) contribute to the total buoyancy gain is more favorable for the formation of more intense PEA, i.e. sharper, stratification.

In Chapter 3, I introduced the potential vorticity (PV) framework to understand the impact of summertime preconditioning by the seasonal stratification on the development of the winter ML. I first addressed the formalization for the estimation of the sea surface PV flux from the observational dataset and then the description of its climatological features. To reduce estimation bias, I revised the scaling laws with considerations of the penetration of the shortwave radiation at the base of the ML and wind-driven mixing in the warming season. Newly estimated surface PV flux was significantly improved, being more consistent with independently calculated variation in the PV of ocean interior. In the annual mean field, I demonstrated well-known classical pictures of air-sea PV exchange: PV gain (loss) occurs in low (high) latitude in both the North Pacific and the North Atlantic. On the other hand, I also found that the balance between diabatic and mechanical contribution to the net PV flux is different among the ocean regions: the mechanical term is more significant in the North Pacific, and the diabatic term is dominant in the high-latitude region of the North Atlantic.

The annual mean PV flux consists of summertime PV input and wintertime PV extraction. To investigate which variability (summertime input or wintertime extraction) contributes to the interannual variability in the annual mean PV flux, I computed their interannual variabilities

separately and compared them in each ocean region. As a result, I found that the interannual variabilities in summertime PV forcing (input) are significantly larger than that of winter (extraction) in the regions where the summertime atmospheric forcing has an impact as preconditioning on the interannual variability in the winter ML depth.

In Chapter 4, I investigated globally the long-term change and variability in the upper-ocean stratification defined here as the difference between the surface and subsurface density. To resolve spatial patterns of the trends and superposed decadal variability, I used temperature and salinity observations with as spatial and temporal coverage as wide as possible. As a result, strengthening trends of the upper-ocean stratification associated with global warming were detected over most of the global ocean, except for the Arctic Ocean. In the global average, the speed of strengthening is 0.0365 kg m^{-3} decade^{-1}, corresponding to an increase of 6.6–11.8% of the mean stratification from the 1960s. I also found that, in addition to the well-mentioned effect of surface intensification of the global warming signal, the subsurface temperature changes and haline stratification changes also have significant impacts on the long-term changes in the upper-ocean stratification. In some ocean regions, the decadal/interannual variabilities in the upper-ocean stratification associated with each particular climate mode are detected: the time series indicate a positive correlation with the Niño 3.4 index in the tropical Pacific, a negative lagged correlation with the North Atlantic Oscillation (NAO) index in the North Atlantic, and correspondences with SST variations associated with the Pacific Decadal Oscillation (PDO) in the North Pacific.

In the present dissertation, I described the seasonal cycle of the upper ocean from two different perspectives with the use of newly introduced concepts. I applied the concept of PEA to the seasonal stratification in the open ocean for the first time and shows its utility for quantitative analysis. The methodology and results of the PEA budget analysis can be utilized for quantifying and understanding the impacts of physical variability on the upper-ocean biogeochemical phenomena. Moreover, the estimation of the surface PV flux improved in this study has the potential to be used not only for the description of the upper-ocean seasonal cycle but also for understanding the fundamental ocean dynamics. In the next decade, Biogeochemical Argo floats that have additional biogeochemical property sensors will become widespread and thus will enable us to investigate the physical-biogeochemical interaction with denser and broader spatiotemporal coverage. I believe that the present results facilitate advances in understanding of not only the ocean's thermal role in the climate system but also its roles in ecological system and material cycle in the earth system.

Acknowledgments

This dissertation has been carried out in the Physical Oceanography Laboratory at Tohoku University and has accomplished with much help from the people around me. I would like to take this part to show my appreciation.

First of all, I would like to express my heartfelt appreciation to Professor Toshio Suga, who is my supervisor, for giving me fundamental guidance of mentality as a scientist and of methodology to expand my view. He also gave me great and precious opportunities to discuss with researchers within and outside of Japan and to experience many fields of study even other than the physical oceanography. All he gave me and learned from him is crucial for this dissertation and will be a core of my life as a scientist.

I owe deep gratitude to members of the physical oceanography group. Professor Kimio Hanawa told me about his perspective and gave me many insightful suggestions. Dr. Shoichi Kizu taught me important knowledge about analyses and presentation of my studies. Dr. Shusaku Sugimoto always gave me advice about from scientific to technical issues throughout this study and always encouraged me. Many constructive comments in our group seminar from Dr. Futoki Sakaida were greatly appreciated.

I would like to thank my senior, graduates, and students in our group. Dr. Daiki Ito kindly looked after me contentiously from the beginning of my laboratory life. Mr. Mochamad Riza Iskandar, Ms. Tong Wang, Mr. Kazuki Hidaka, Ms. Mizuki Iida, Ms. Fumika Sanbe, Mr. Suguru Hanzawa, Mr. Satoshi Nitta, Mr. Shunsuke Okada, Mr. Asuto Sakai, Mr. Shota Sera, Mr. Yusuke Miura, Mr. Hanani Adiwira, Ms. Emelie Breunig, and graduates chatted about interesting topics with a cup of coffee and cheered me up.

I am deeply grateful to Ms. Sachie Prestel, Ms. Akane Oikawa and secretaries of the Division for Interdisciplinary Advanced Research and Education (DIARE) and the International Joint Graduate Program in Earth and Environmental Science (GP-EES) for providing a comfortable working environment and supporting my research activities.

I also would like to express my gratitude to scientists for giving me much advice to accomplish this dissertation outside of our laboratory. Professor Kelvin J. Richards and Professor Bo Qiu at the University of Hawai'i had many times for discussion and gave me many invaluable comments and suggestions during my stay at International Pacific Research Center in the University of Hawai'i. Dr. Eitaro Oka at the University of Tokyo gave me great opportunities to join research cruises and to interact with other researchers. Dr. Shinaya Kouketsu and Dr. Shigeki

Ryohei Yamaguchi
January 2019, Sendai

Contents

Chapter 1
General introduction

1.1 Background
1.1.1 Seasonal stratification during the warming season

In the upper ocean from the surface to several hundred meters, there is a predominant seasonal cycle of the water column, mainly driven by the seasonality of the atmospheric forcing (Fig. 1.1). Because the upper ocean is unstable due to surface cooling in winter, a deep surface mixed layer where the temperature and salinity (i.e., the density) are vertically uniform develops by convection. When it becomes summer in turn, seasonal stratification develops under the remnant thin surface mixed layer because the water column becomes warmer and thus lighter from its upper part by predominant surface heating.

The seasonal stratification developed during the warming season stabilizes the water column, regulates the vertical exchange of the water and, therefore, discriminates between relatively warmer and nutrient-poor near-surface water and cooler and nutrient-rich water below. In other words, the seasonal stratification characterizes the "difficulty in mixing" of the water column during the warming season. Indeed, recent observational studies show that the vertical mixing below the mixed layer is controlled by the strength of the seasonal stratification (Qiu et al. 2004; Cronin et al. 2013) and the modulated mixing is thought to have a significant impact on the determination of the sea surface temperature during the warming season (Hosoda et al. 2015; Lee et al. 2015). It has also been pointed out that the stability due to the seasonal stratification plays an important role in the biogeochemical processes such as the occurrence of spring phytoplankton bloom (Dale et al. 1999), vertical supply of the nutrients (Sukigara et al. 2011), and the formation of subsurface oxygen maximum layer (Shulenberger & Reid 1981).

Although the seasonality of the upper-ocean water column is a ubiquitous feature in the global ocean from low to high latitudes, the vertical structure of the seasonal stratification differs regionally (Fig. 1.2). The amplitude of the seasonality and the depth range where the seasonality is apparent are remarkably different depending on the ocean region and/or latitude. These different features suggest that the seasonal stratifications are formed reflecting the result of regional differences in the dominant processes and the balance between them and, moreover, the stratifications play different physical and biogeochemical roles in the respective regions.

Historically, in understanding the ocean response to the atmospheric forcing (heat, freshwater, and momentum), the thickness of the mixed layer, that temporarily responses directly

to the forcing, has been thought to be one of the most important variables. Hence, studies about the physical processes in the upper ocean have been progressed focusing around the mixed layer process. As one of the results, recent one-dimensional mixed layer models can successfully reproduce the observations and are implemented in many of the general ocean circulation models and climate models. On the other hand, the formation processes of the seasonal stratification under the mixed layer, including various physical processes (propagation and breaking of the internal wave and shear instability etc.: e.g., Johnston & Rudnick 2009) and thus being difficult to be modeled, currently has been less well understood. Recently, as enhanced performances of computers such as the appearance of the Large Eddy Simulation that can directly compute the small-scale physical process, some studies about the elementary process of the formation of seasonal stratification have been done (e.g., Goh & Noh 2013). However, the quantitative observational descriptions of the development of the seasonal stratification for comparison with the model studies have been scarcely made, especially in the open ocean where time series observation of high vertical resolution temperature and salinity profile are hard to be obtained.

Moreover, recent observational studies pointed out that, in the warming season, only the mixed layer depth does not always determine the temporary thermal inertia of ocean in response to the atmospheric forcing because the mixed layer is extremely thin (Hosoda et al. 2015). Unlike previously thought, this suggests that the direct response of the layer below the mixed layer, that is, the formation of the seasonal stratification also has to be considered to understand the air-sea interaction during warming season. From the above background, it is thought that detailed descriptions of the formation of the seasonal stratification from observations and quantitatively clarifying the mechanism of the development are needed for an advance of our understanding about the air-sea interaction in the warming season and the upper-ocean biogeochemistry.

1.1.2 Variability in the upper-ocean stratification and its impact

Influences due to stabilization of the upper-ocean water column by the seasonal stratification are not limited in the warming season. In the seasonal cycle of the upper ocean, the winter mixed layer develops as destroying the seasonal stratification formed during prior warming season (c.f., Fig. 1.1). Therefore, the strength of the upper-ocean stratification at the end of the warming season (called as summertime preconditioning) affects the development of the following winter mixed layer (e.g., Qiu & Chen 2006; Sugimoto & Kako 2016). Indeed, a case that anomalously strengthened seasonal stratification at end of summer prevented the mixed layer from developing in the following winter has also reported in a formation region of a major water mass (Kako &

Kubota 2007). Although in limited regions of the water mass formation, interannual variability in the strength of the seasonal stratification significantly contributes to that of the winter mixed layer depth (Toyoda et al. 2011).

The formation and subduction of the water mass in winter play an important role of the driver on the ocean ventilation process, which is essential role of ocean in climate system and results in oceanic uptake of heat, carbon, and oxygen. The late winter mixed layer depth is one of the key factors that controls the volume of the water mass formation. Therefore, the interannual variability in the strength of the seasonal stratification in the warming season also has the possibility of playing an important role in the climate system, through the ocean ventilation process.

In recent years, long-term variability in the upper-ocean stratification has also received a lot of attention in the context of climate change. Future projections by the state-of-the-art climate models (Coupled Model Intercomparison Project; CMIP) shows the long-term strengthening of the upper-ocean stratification due to the surface intensification of the ocean warming associated with global warming (Cabré et al. 2014). The strengthened stratification will reduce vertical nutrient supply from the subsurface by more stabilizing the upper-ocean water column, and then the primary production of whole ocean is concerned to decrease (Fu et al. 2016).

From the observational perspective, strengthening trend of the upper-ocean thermal stratification due to the surface intensification of the warming signals has been detected from an estimation using globally-averaged sea surface and subsurface temperature time series (Rhein et al. 2013). On the other hand, some observational studies focusing on some specific regions or using relatively short time series demonstrate that the upper-ocean stratifications are weakening in recent decades, rather than strengthening associated with global warming (Dave & Lozier 2013; Somavila et al. 2017). Therefore, large uncertainties of the observational estimate of the long-term change in the upper-ocean stratification, probably due to the regional difference in the change and/or prevailing decadal variability, still remain.

1.2 Objectives and organization of the present dissertation

According to the above background, the objectives of the present dissertation are quantitatively to clarify the formation mechanism of the seasonal stratification from observational data (Chapter 2), and gain a further understanding of roles of the upper-ocean stratification on the climate system through describing these spatiotemporal variabilities (Chapter 3 and 4). To achieve these objectives, we have done three quasi-independent works and summarized them into the present

dissertation. The organization of the present dissertation is as follows.

As mentioned in Subsection 1.1.1, a detailed description of the seasonal stratification is not enough yet because of its historical and observational background. In Chapter 2 of this dissertation, focusing on the North Pacific, we provide the detailed description of the development of the seasonal stratification based on the temperature and salinity profiles measured by Argo float from the international Argo program (Riser et al. 2016). To represent "difficulty in mixing" of the seasonal stratification, which is one of the essential properties of the stratification as mentioned above, we use the Potential energy anomaly (PEA) advocated by Simpson (1981) as the indicator of the strength of the seasonal stratification. Performing the budget analysis of PEA to the seasonal development of the stratification in the open ocean, we quantitatively clarify the formation mechanism of the seasonal stratification and discuss the cause of the regional differences in the development.

The impacts of the interannual variability in the strength of seasonal stratification at the end of warming season on the development of winter mixed layer have been reported by different approaches in previous studies about the interannual variability in the winter mixed layer depth of formation regions of the major water mass. In Chapter 3 of the present dissertation, we introduce and discuss the potential vorticity (PV) framework to interpret comprehensively these previous results (especially, about why the impact of summertime preconditioning is apparent in limited regions). Using the PV framework, we able to treat together the development of the seasonal stratification during warming season and the development of the mixed layer during cooling season uniformly as oceanic PV gain and loss, respectively, which have been represented commonly by different indicators. Moreover, diabatic (heating/cooling, freshwater exchange, etc.) and mechanical (wind friction etc.) forcing that drives the development of the seasonal stratification and the mixed layer are elegantly put together within a single representation of the sea surface PV flux.

In Chapter 4, we examine the long-term change and variability in the global upper-ocean stratification form observations. We use observational data with as great a spatial and temporal coverage as possible, to consider the influences from the regional difference of the change and simultaneous decadal variability, causing uncertainties of its estimates. Using observational time series which has been the longest ever, we elucidate the impact of the global warming on the upper-ocean stratification at the present time. We also investigate the relative contribution of the thermal and haline structure changes on the long-term change in density stratification and the relationship between the long-term detrended variability and climate modes prevailing in the

respective ocean regions.

Finally, we summarize the results and show the prospect of the next in Chapter 5.
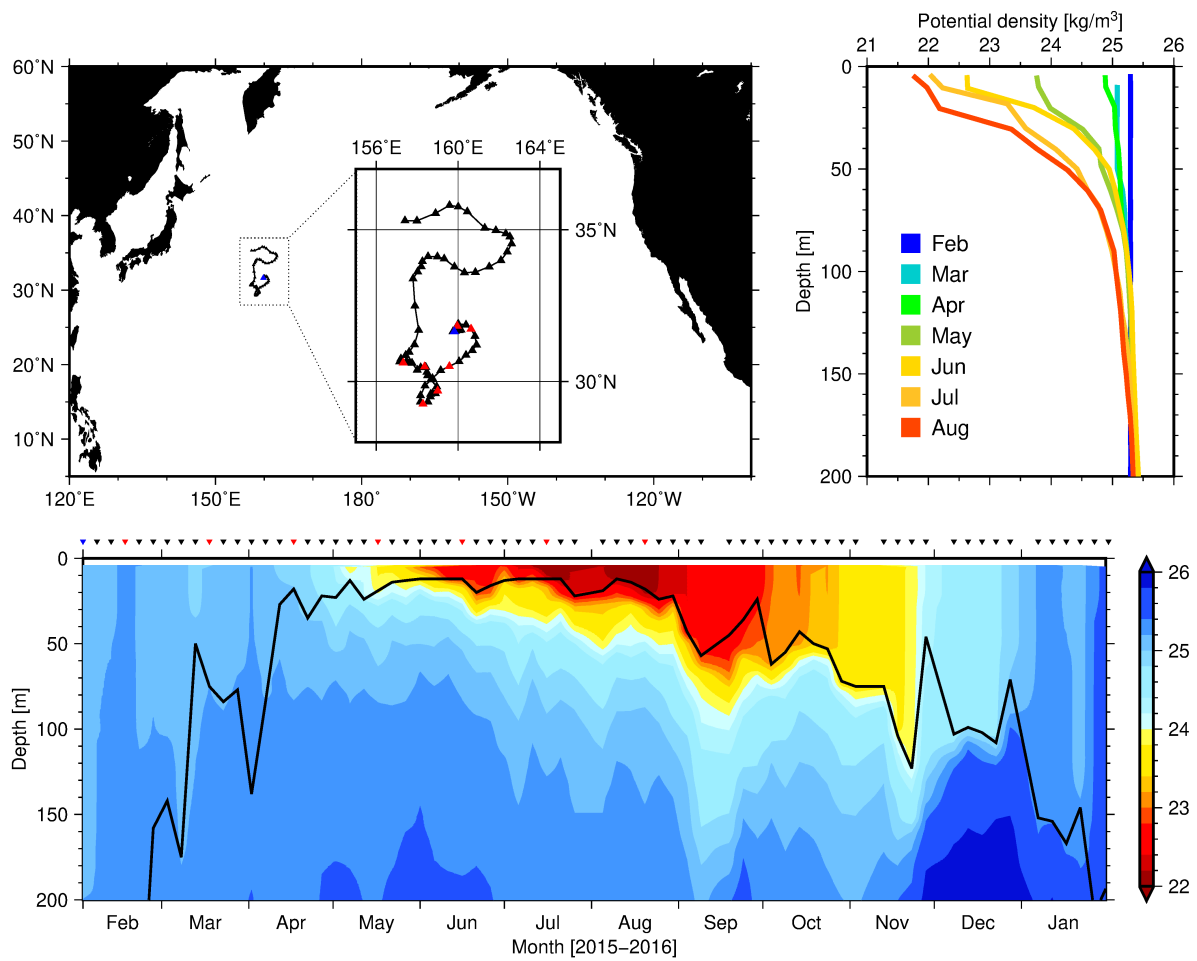
Figure 1.1. (upper right) Vertical profiles and (lower) time-depth section of potential density observed by an Argo float (WMO No. 2902488) and (upper left) their locations. Red colored triangles indicate the locations and date of vertical profiles shown in the upper right panel.

Figure 1.2. The climatological seasonal cycle of upper ocean potential density (kg m^{-3}) from Roemmich–Gilson Argo climatology (Roemmich & Gilson 2009). The profiles are averaged in 30° (longitude) × 20° (latitude) area centered at labeled location (longitude [°E], latitude [°N]).

Chapter 2
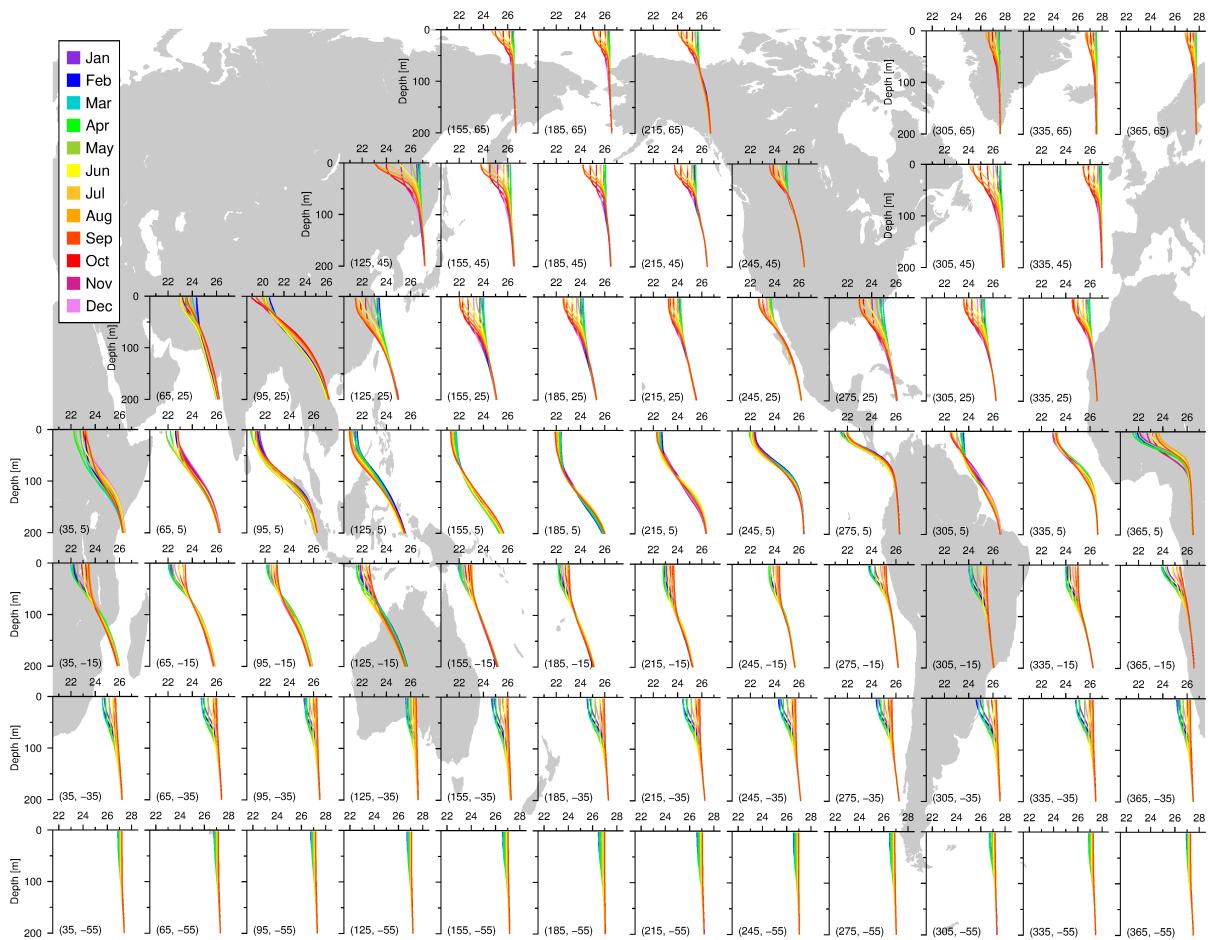# Diagnosing the development of seasonal stratification using the potential energy anomaly (PEA) in the North Pacific

2.1 Introduction

The upper ocean in the warming season consists of a relatively thin mixed layer (ML) and seasonal stratification (seasonal pycnocline and/or transition layer) below the ML. Seasonal change in the stratification is a ubiquitous feature of the North Pacific. In the warming season, the stratification develops as a result of heating, freshwater supply and wind forcing from the atmosphere, and oceanic lateral processes. Although the development of a seasonal stratification occurs over the North Pacific, its vertical structure differs regionally (Fig. 2.1). For example, shallower and sharper seasonal stratification tends to develop in the northern part of the North Pacific compared to the southern part. In the Kuroshio and its extension regions, a more substantial buoyancy gain occurs in the subsurface, leading to stratification with more linear vertical structures. These features are the result of regional differences in the dominant processes of forming the seasonal stratification.

Heat, freshwater, momentum, and chemical tracers exchanged between the atmosphere and ocean are transported into the ocean interior through the ML and the seasonal stratification. Because the seasonal stratification characterizes "difficulty in mixing (i.e., stability)" of the upper ocean due to its maxima in the density stratification, it has great potential of influences on physical and biogeochemical processes within the upper ocean. Vertical mixing below the ML during the warming season is controlled by the strength of stratification (Qiu et al., 2004; Cronin et al. 2013). In turn, this can affect the supply of nutrients from the subsurface and the vertical transport of heat, which is an important factor in determining the sea surface temperature during the warming season (Hosoda et al. 2015). Moreover, not only in the warming season, the upper-ocean stability that develops during the warming season can also affect ocean ventilation via its impact on the development of the winter ML (e.g. Qiu and Chen 2006; Kako and Kubota 2007). Despite the importance of the seasonal stratification for physical and biogeochemical processes, the formation and spatial variability of seasonal stratification has not been widely investigated from an observational perspective (e.g., Johnston and Rudnick 2009).

Previous model and observational studies have used common metrics to quantify upper-ocean stratification. These include the density or temperature difference between the surface and subsurface, and the buoyancy frequency (Tomita et al. 2010; Capotondi et al. 2012; Maes &

O'Kane, 2014). Although these metrics are useful, being readily obtained from low vertical resolution observational data or climate model output, they do not always quantify the "difficulty in mixing", which is the essence of the seasonal stratification. To assess the influences of the seasonal stratification on biogeochemical processes and air-sea interaction, a metric capable of quantitatively representing this "difficulty in mixing" of the water column is needed.

In this chapter, we used the potential energy anomaly (PEA; ϕ) advocated by Simpson (1981). PEA defined from the surface ($z = 0$) to the base of a depth ($z = -H$) is written as;

$$\phi = \frac{1}{H}\int_{-H}^{0}(\bar{\rho} - \rho)gz \, dz = -\frac{1}{H}\int_{-H}^{0}\tilde{\rho}gz \, dz \qquad (2.1)$$

with the vertically averaged potential density being written as

$$\bar{\rho} = \frac{1}{H}\int_{-H}^{0}\rho \, dz,$$

where $\tilde{\rho}$ ($= \rho - \bar{\rho}$) is the deviation from the vertically averaged potential density and g is the acceleration due to gravity. PEA provides a measure of the amount of energy per unit volume (J m^{-3}) required to make the density stratified water column vertically homogeneous; it, therefore, represents the "difficulty in mixing". Examples of calculation of PEA are shown in Fig. 2.2. Using this PEA as an indicator of the strength of seasonal stratification, together with its time-dependent equation, we are able to discuss quantitatively the development and spatial variability of the seasonal stratification in terms of stability.

Making use of observational data, the purpose of this chapter is to describe the development of seasonal stratification in terms of "difficulty in mixing", and to discuss the dominant processes forming the stratification and their balance using a time-dependent equation for PEA. We also examine the utility of the PEA budget analysis, which has generally been used in studies of coastal studies, to the seasonal stratification in the open ocean. The remainder of this chapter is organized as follows. In Section 2.2, the dataset and the processing methods are described. The PEA climatological field and its seasonal cycle are described in Section 2.3. In Section 2.4 we outline the configuration and validation of the PEA budget analysis and the results of the PEA budget. In Section 2.5 we discuss the term balance of term in the budget and its regional differences. Finally, a summary is provided in Section 2.6.

2.2 Data and methods

We mainly used the Advanced automatic Quality Control Argo data (AQC Argo data;

http://www.jamstec.go.jp/ARGO/argo_web/ancient/AQC/index.html) for temperature and salinity profiles provided by the Japan Agency for Marine-Earth Science and Technology (JAMSTEC). AQC Argo data includes the Global Data Assembly Center (GDAC) real-time quality control profiles (Argo 2000), with additional quality controls performed by JAMSTEC. The spatial coverage of the Argo profiles in the North Pacific after 2006 is sufficient for detecting the seasonal cycle of the upper-ocean stratification. Profiles collected from January 2006 to December 2016 were used. Due to the scarcity of profiles in the coastal and marginal sea regions, these regions were excluded from subsequent analysis. Although the vertical resolution of Argo profiles varies with the initial setting or/and data transfer method, half of the profiles used in this chapter have more than 15 observations in the upper 100 m of the ocean. Vertically coarse profiles (those with a vertical spacing greater than 10 m) account for less than 5 % of the profiles.

From the QC'ed profiles by JAMSTEC, a few profiles were excluded because they exceeded three standard deviations of the mean profile calculated for the month and within the 3°(longitude) × 3° (latitude) area. After this QC procedure and the potential density calculation, profiles were vertically interpolated to 1-m intervals using the Akima spline (Akima 1970). To obtain the gridded fields of the metrics (e.g., PEA and ML depth) and to avoid the smoothing of vertical structures by the spatial and temporal averaging of profiles, metrics were calculated from the raw profile data. Monthly 1°(longitude) × 1°(latitude) fields for each metric were produced using a weight function that is inversely proportional to the distance from the grid point, following Oka et al. (2015).

To evaluate the contribution of lateral processes to the change in seasonal stratification, we also used the Roemmich–Gilson Argo climatology (RG Argo; Roemmich & Gilson 2009). The dataset was gridded using monthly objective mapping to 1° × 1° horizontal resolution with latitude-dependent decorrelation scales. The dataset has 58 levels in the vertical, with a 10 dbar resolution above 170 dbar and a maximum depth of 1975 dbar. After vertical interpolation, using the same procedure as for Argo profiles, we calculated the geostrophic velocity profile assuming a reference depth of 1975 dbar. Daily averaged gridded QuikSCAT and Advanced Scatterometer (ASCAT) wind stress products made available through the Asia–Pacific Data-Research Center (http://apdrc.soest.hawaii.edu/) were used to obtain the monthly Ekman transport field.

We used three daily mean atmospheric datasets to calculate atmospheric buoyancy forcing. The surface net heat flux, Q_{net}, and its four components (shortwave radiation, Q_{SW}; longwave radiation, Q_{LW}; sensible heat flux, Q_{SH}; latent heat flux, Q_{LH}) are from the Japanese Ocean Flux Data Sets with Use of Remote Sensing Observations 3 (J-OFURO3; Tomita et al. 2018). The J-

OFURO3 data are derived using a bulk formula to estimate turbulent fluxes based on parameters observed by multiple satellites and have a spatial resolution of 0.25° × 0.25°. The radiation data were taken from the International Satellite Cloud Climatology Project (ISCCP) and Cloud and the Earth's Radiant Energy System (CERES). For the component of freshwater flux, $E - P$ (evaporation minus precipitation), we used the Global Precipitation Climatology Project ver1.2 (GPCP; Huffman et al. 2001) for precipitation rate and the Objectively Analyzed Air-Sea Flux (OA Flux; Yu et al. 2008) for the evaporation rate. The net surface buoyancy flux, $B = -g(\alpha Q_{net}/C_p\rho_0 - \beta(E - P)S_0)$, was then estimated from the net surface heat and freshwater fluxes, where $C_p\rho_0$ $(= 4.09 \times 10^6 \text{ J °C}^{-1} \text{ m}^{-3})$ is the volumetric heat capacity of seawater, S_0 is the sea surface salinity, and α and β are the thermal expansion and haline contraction rates of seawater, respectively. These heat and freshwater flux datasets were averaged over the analytical period to obtain a monthly climatology with 1° × 1° horizontal resolution.

The averaging periods for J-OFURO3 and GPCP data are 2006–2013 and 2006–2014, respectively, based on data availability. Although these averaging periods are shorter than those of the oceanic variables (2006–2016), they do not have an impact on our results from the analyses below. We checked that the results of this chapter were qualitatively unchanged using a climatology constructed from 2006–2013 Argo data.

2.3 Seasonal cycle of PEA

Since the focus of this work is the layer of the ocean where the density shows seasonal variation (hereafter, seasonal boundary layer), we set the lower limit in the PEA calculation (*H*) to the local annual maximum of ML depth. ML depth is defined as the depth at which potential density increases (or temperature differs) from the surface value by 0.125 kg m^{-3} (0.5 °C), following the widely used threshold method (Monterey & Levitus 1997). The surface value is assigned to the value at 5 m depth. The seasonal boundary layer depth, *H*, was obtained from the monthly ML depth climatology derived from raw profile ML depths using the above-mentioned mapping method. The spatial distribution of *H* used in the calculation of PEA is shown in Fig. 2.3. The thickness of the seasonal boundary layer has significant spatial variability (Fig. 2.3). Although *H* can exceed 200 m (the maximum value is 247 m) in the northwestern part of the subtropical gyre where the ML is well developed in late winter (Suga et al. 2004), *H* is ~100 m south of 20°N and is shallowest in the eastern part of the tropics. In pioneering work using observations to investigate upper-ocean heat and freshwater balance (Moisan & Niiler 1998; Giglio & Roemmich 2014), a surface that behaves similarly to a material surface was defined in the subsurface and this surface

11

used as the base in the budget calculation. Since H in the study of this chapter is defined using a similar procedure to these studies, we regard H as a material surface, at least, in the warming season (i.e., when the ML is shallow). Indeed, the material surface defined in Fig. 1 of Giglio & Roemmich (2014) has a similar spatial distribution to that of H in this study (Fig. 2.3).

The monthly climatology of PEA is shown in Fig. 2.4. PEA has a characteristic spatial distribution that reflects the spatially non-uniform development and decay of the seasonal stratification in the North Pacific. The development of PEA has a latitudinal maximum along 35°N and another local maximum in the eastern part of tropics at ~10°N, across a region where the development of PEA is relatively minor. Comparison with the spatial distribution of ML depth reveals that the PEA is larger in the shallower ML depth region during the warming season. However, in late summer (August–September) when PEA is fully developed, the spatial patterns of these two fields do not always correspond. This suggests that PEA development is not determined simply by processes controlling the ML depth under stabilizing forcing during the warming season.

Focusing on seasonal variation in PEA (Fig. 2.5), the phase of PEA development differs between the high- and mid-latitudes and the tropics. As one might expect, in the high- and mid-latitudes north of 20°N, PEA, which becomes zero by mixing and convection induced by strong cooling and wind forcing during winter, begins to develop in spring and early summer (March–April) and reach its annual maximum stage of development in mid-summer (July–August). In the eastern part of tropics, the phase of PEA development is about two months behind that of the mid-latitudes; the PEA starts to develop in May or June and peaks in October or November. At the latitude of 15°–25°N, the PEA develops from spring to early summer in its western part and during late summer in its eastern part, although the changes are relatively small. PEA development lasts around six months over the whole North Pacific, although the phase differs among regions. The decay of PEA is a mirror image of the development phase.

It is expected that the surface stabilizing buoyancy forcing is an important factor in the development of seasonal stratification, such as the well-known mixed layer processes under stabilizing forcing. We examined the phase relationship between the development of PEA and the surface buoyancy gain during the warming season. Figure 2.6 shows the month of maximum development of PEA (Fig. 2.6a) and the net surface buoyancy gain (Fig. 2.6b) over the North Pacific, together with their difference (Fig. 2.6c). The negative values in Fig. 2.6c indicate that the peak of PEA development precedes that of the net surface buoyancy gain. In many regions of the north of 20°N there is little difference between the phase of their peaks, suggesting that the

surface buoyancy forcing plays a dominant role in the development of seasonal stratification in the high- and mid-latitudes. In contrast, significant differences can be seen in regions south of 20°N where the monthly change in PEA is small. This suggests that aside from the surface buoyancy forcing, other factors, such as lateral processes, contribute to the development of seasonal stratification in the North Pacific.

2.4 PEA budget analysis

To quantify the relative contribution of processes driving the development of the seasonal stratification in the North Pacific, we performed a PEA budget analysis using a time-dependent equation for the PEA (Burchard & Hofmeister 2008). Since our focus is the developing phase of the seasonal stratification, we applied the PEA budget analysis to only the warming season (April–August).

2.4.1 Time-dependent equation for PEA

Burchard and Hofmeister (2008) derived a time-dependent equation for PEA based on the potential temperature and salinity equations, the continuity equation and an equation of state for the potential density. The time rate of change of PEA, defined from the sea surface ($z = 0$) to the annual maximum of ML depth ($z = -H$), can be written as follows:

$$\frac{\partial \phi}{\partial t} = \underbrace{-\nabla_h \cdot (\bar{\mathbf{u}}\phi)}_{<1>} \underbrace{+\frac{g}{H}\nabla_h\bar{\rho} \cdot \int_{-H}^{0} z\widetilde{\mathbf{u}} \, dz}_{<2>}$$

$$\underbrace{-\frac{g}{H}\int_{-H}^{0}\left(-\frac{H}{2}-z\right)\widetilde{\mathbf{u}} \cdot \nabla_h\tilde{\rho} \, dz}_{<3>} \underbrace{-\frac{g}{H}\int_{-H}^{0}\left(-\frac{H}{2}-z\right)\widetilde{w}\frac{\partial\tilde{\rho}}{\partial z} \, dz}_{<4>}$$

$$\underbrace{+\frac{\rho_0}{H}\int_{-H}^{0}P_b \, dz}_{<5>} \underbrace{-\frac{\rho_0}{2}\left(P_b^s + P_b^H\right)}_{<6>} \underbrace{+\frac{g}{H}\int_{-H}^{0}\left(-\frac{H}{2}-z\right)Q \, dz}_{<7>}$$

$$\underbrace{+\frac{g}{H}\int_{-H}^{0}\left(-\frac{H}{2}-z\right)\nabla_h \cdot (K_h\nabla_h\rho) \, dz}_{<8>}, \tag{2.2}$$

where $\bar{\mathbf{u}}$ is the vertically averaged horizontal velocity vector defined as

$$\overline{\mathbf{u}} = \frac{1}{H} \int_{-H}^{0} \mathbf{u} \, dz \, ; \tag{2.3}$$

$\widetilde{\mathbf{u}}$ is the deviation from the vertically averaged horizontal velocity vector, $\widetilde{\mathbf{u}} = \mathbf{u} - \overline{\mathbf{u}}$; $\overline{w}$ and $\widetilde{w}$ are the vertical velocity defined by the continuity equation,

$$\mathbf{\nabla}_h \cdot \overline{\mathbf{u}} + \frac{\partial \overline{w}}{\partial z} = 0, \tag{2.4}$$

and its deviation, $\widetilde{w} = w - \overline{w}$; $\mathbf{\nabla}_h$ is the horizontal gradient operator; P_b is the vertical buoyancy flux represented as

$$P_b = \frac{g}{\rho_0} K_v \frac{\partial \rho}{\partial z} \tag{2.5}$$

with the vertical diffusivity K_v and a constant reference density ρ_0; P_b^s and P_b^H are buoyancy flux at the surface and at the annual maximum of ML depth, respectively; K_h is the horizontal eddy diffusivity; and Q is the source term of potential density,

$$Q = -\frac{\rho\alpha}{\rho_0 C_p} \frac{\partial I}{\partial z} + K_v \frac{\partial}{\partial z} \theta \frac{\partial \rho\alpha}{\partial z} - K_v \frac{\partial}{\partial z} S \frac{\partial \rho\beta}{\partial z}$$

$$+ K_h \mathbf{\nabla}_h \theta \cdot \mathbf{\nabla}_h (\rho\alpha) - K_h \mathbf{\nabla}_h S \cdot \mathbf{\nabla}_h (\rho\beta), \tag{2.6}$$

with the penetrated shortwave radiation, I, and the potential temperature, θ.

    Terms 1–4 in Eq. 2.2 represent the change in PEA induced by the ocean currents. Terms 1 and 4 represent the PEA advection, including vertical density advection by $\overline{w}$. Term 2, the depth-mean straining, quantifies the change in PEA due to a vertically sheared horizontal current in the presence of a horizontal gradient of vertically averaged density. Term 3, the non-mean straining, represents PEA change due to the horizontal current and the density with vertically correlated variation. This term dictates that a PEA change may occur due to horizontal change in the vertical density gradient, even if the vertical averaged density is horizontally constant. Term 5 represents a decrease in PEA due to the rearrangement of water in the seasonal boundary layer, induced by vertical mixing. The surface and bottom buoyancy fluxes also contribute to PEA changes (Term 6). An inner sink or source of potential density (Term 7) can contribute to stabilizing or destabilizing of the water column; if a sink (e.g., the penetration of shortwave radiation) is in the upper (lower) half of the water column, PEA will increase (decrease). Term 8 represents change due to divergence/convergence of horizontal eddy diffusive density fluxes and creates a change in the same manner as Term 7. For further explanation of each term and the detailed derivation of Eq. 2.2, see Burchard & Hofmeister (2008).

Considering the spatiotemporal scales of interest to the study in this chapter, we simplified the time-dependent equation for PEA under the following assumptions. The vertical velocity in the seasonal boundary layer of the horizontally smoothed fields is quite small (typically on the order of 10^{-6} m s^{-1}). Term 4 of Eq. 2.2, therefore, becomes one or two orders of magnitude smaller than other terms (e.g., an order of magnitude smaller than Term 3). Likewise, the seasonal contribution from horizontal eddy diffusivity is expected to be small in large-scale averaged fields, except near the equatorial and western boundary current regions (Moisan & Niiler 1998; Giglio & Roemmich 2014; Ren & Riser 2009). In addition, since the vertical density gradient is generally small at the annual maximum of ML depth, we can assume that the bottom buoyancy flux due to vertical mixing (P_b^H) is negligible. For convenience, we assume that only the penetration of shortwave radiation into seawater is solely responsible for the inner source of potential density term (Term 7). With these assumptions, Eq. 2.2 can be rewritten as follows:

$$\frac{\partial \phi}{\partial t} = \underbrace{-\boldsymbol{\nabla}_h \cdot (\overline{\mathbf{u}}\phi)}_{A} + \underbrace{\frac{g}{H}\boldsymbol{\nabla}_h\bar{\rho}\cdot\int_{-H}^{0} z\widetilde{\mathbf{u}}\,dz}_{B} + \underbrace{-\frac{g}{H}\int_{-H}^{0}\left(-\frac{H}{2}-z\right)\widetilde{\mathbf{u}}\cdot\boldsymbol{\nabla}_h\tilde{\rho}\,dz}_{C}$$

$$\underbrace{-\frac{\rho_0}{2}P_b^s}_{D} + \underbrace{\frac{g}{H}\int_{-H}^{0}\left(-\frac{H}{2}-z\right)\left(-\frac{\rho\alpha}{\rho_0 C_p}\frac{\partial I}{\partial z}\right)dz}_{E} + (Residual), \tag{2.7}$$

where the residual term includes vertical mixing (Term 5 of Eq. 2.2) and all terms that are assumed to be negligibly small.

To estimate the vertical profile of penetrating shortwave radiation, $I(z)$, we adopted a generalized empirical model using the inherent optical properties of seawater (Lee et al. 2005). Specifically, the penetration of shortwave radiation is represented as;

$$I(z) = I(0)e^{-K_{VIS}z} \tag{2.8}$$

where K_{VIS} is the attenuation coefficient for the visible domain of shortwave radiation and is modeled as a function of depth and absorption and backscattering coefficients at 490 nm (a, b_b, respectively):

$$K_{VIS}(z, a, b_b) = K_1(a, b_b) + \frac{K_2(a, b_b)}{(1+z)^{0.5}} \tag{2.9}$$

$$K_1(a, b_b) = \chi_0 + \chi_1 a^{0.5} + \chi_2 b_b$$

$$K_2(a, b_b) = \zeta_0 + \zeta_1 a + \zeta_2 b_b.$$

Here, χ_0-χ_2 and ζ_0-ζ_2 are constant parameters derived from radiative transfer numerical simulations. The typical range of K_{VIS}^{-1} is roughly 5–15 m at 10 m depth, with the value increasing with depth and reaching $K_{VIS}^{-1} = 25$ m at 100 m depth (further explanations are in Appendix 2A). The skill and robustness of this model in reproducing the observed transmittance of shortwave radiation for both open oceanic clear water and coastal turbid water have been demonstrated in recent studies (Xiu & Chai 2014; Zoffoli et al. 2017). Figure 2.7 shows the penetrating component of the shortwave radiation, calculated using the attenuation and backscattering coefficients from the Moderate Resolution Imaging Spectroradiometer (MODIS Aqua; NASA Goddard Space Flight Center, Ocean Ecology Laboratory, Ocean Biology Processing Group 2014). The penetrating component of shortwave radiation has a large spatial variability and becomes larger within the subtropical gyre because of the high transparency of seawater (Fig. 2.7). The fraction of shortwave radiation able to penetrate beyond the upper few centimeters of the ocean, γ, is assigned a value of 0.33 (Chen et al. 1994; Zhang et al. 2011). The penetrating component of the shortwave radiation at the surface is, $I(0) = \gamma Q_{SW}$, and the non-penetrating buoyancy flux (Fig. 2.8; i.e., the fraction absorbed near the surface; the sum of sensible and latent heat fluxes, the longwave radiation flux, and the remaining shortwave radiation flux) becomes

$$P_b^s = -g\left(\frac{\alpha\big((1-\gamma)Q_{SW} + Q_{LW} + Q_{SH} + Q_{LH}\big)}{C_p\rho_0} - \beta(E-P)S_0\right). \tag{2.10}$$

On the spatiotemporal scales relevant to this work, the horizontal velocity vector in Eq. 2.7 is simply given as the sum of geostrophic and Ekman components. To obtain the vertical profile of Ekman velocity, we assumed that the Ekman velocity is constant in the ML and exponentially decays below the ML, following the Large Eddy Simulation (LES) study of Goh & Noh (2013). By vertically redistributing the Ekman transport estimated from satellite wind fields, we calculated the vertical profiles of Ekman velocity at grid points. Adding the geostrophic velocity computed from the RG Argo data (using a reference pressure of 1975 dbar) to the Ekman velocity, we obtained the depth-dependent horizontal velocity field. A comparison at 15 m depth between the resulting velocity field and a two-dimensional ocean current product (Ocean Surface Currents Analyses Real-time (OSCAR); Bonjean & Lagerloef 2002) demonstrated a good agreement for both the magnitude and direction of the velocity field (Fig. 2.9 and 2.10).

2.4.2 PEA balance in the budget
The results of the PEA budget (RHS of Eq. 2.7) for July–August are shown in Fig. 2.11. As

expected from the phase relationship between PEA development and surface buoyancy forcing (Fig. 2.6), terms representing atmospheric buoyancy forcing (Terms D and E) are dominant. The sum of the non-penetrating buoyancy forcing (Term D) and the penetration of shortwave radiation (Term E) determines the spatial distribution of PEA development (Fig. 2.5).

Contributions from lateral processes (Terms A, B, and C) are relatively small throughout the period of PEA development (shown in Fig. 2.11a–c). PEA advection (Term A), however, makes a significant contribution in regions where dynamic height contours are concentrated, such as the Kuroshio/Kuroshio extension and the equatorial current system south of 10°N (Fig. 2.11a). The depth-mean straining term (Term B) increases PEA up to 30 J m^{-3} month^{-1} south of 30°N. This is because the northward Ekman flow due to the trade winds carries near surface lighter water from the south, which strengthens stratification (Fig. 2.11b). In the region where the depth-mean straining term reaches its maximum value (approximately 130°W, 20°N), its contribution is comparable to the buoyancy terms. The non-mean straining term (Term C) is smaller than 10 J m^{-3} month^{-1} for the whole of the North Pacific, except in a few limited regions (Fig. 2.11c).

The residual term shows relatively uniform negative values, suggesting a decrease in PEA due to vertical mixing in the water column. In many parts of the North Pacific, the residual term is the second largest, after the sum of buoyancy flux terms (Fig. 2.11f). The dominance of Terms D and E in determining the PEA development is also found during other months of the PEA development period (Fig. 2.12–14). Accordingly, this suggests, except in the strong current regions, seasonal stratification in the North Pacific develops under a vertical one-dimensional energy balance between the surface and/or inner buoyancy gain and buoyancy redistribution by vertical mixing.

2.4.3 Residual term and validation of the budget

Although the negative residual term is consistent with the vertical mixing acting to decrease in PEA, the term is itself a combination of terms that we are unable to estimate and the errors in those we can estimate. It is difficult to estimate precisely these uncertainties. However, we can get an estimate for the vertical diffusivity by assuming the case that vertical mixing dominates the residual term.

Assuming the vertical mixing (Term 5 of Eq. 2.2) is responsible for the change in PEA due to residual terms, the vertically averaged vertical diffusivity weighted by the vertical density gradient, $\overline{K_v}$, can be computed as

$$\overline{K_v} = \frac{H}{g} (Residual)(\int_{-H}^{0} \frac{\partial \rho}{\partial z} \, dz)^{-1}. \tag{2.11}$$

The seasonal change in the spatial distribution of $\overline{K_v}$ obtained from monthly residual term, excluding regions with a positive residual (i.e., with negative $\overline{K_v}$), is shown in Fig. 2.15. The largest diffusivity value (exceeding $3 \times 10^{-4} \, \mathrm{m^2 \, s^{-1}}$) are found in regions where the ML is relatively deep, and where strong vertical mixing remains into the spring and early summer (Fig. 2.15a; see also Fig. 2.4). In mid-summer when the ML becomes shallow relative to H, the diffusivities range roughly between $5 \times 10^{-5} \, \mathrm{m^2 \, s^{-1}}$ and $5 \times 10^{-4} \, \mathrm{m^2 \, s^{-1}}$, and show a distinct seasonal change.

The dependency of the diffusivity on the local wind forcing is shown in a scatter plot of the logarithm of $\overline{K_v}$ and the logarithm of the cube of the surface frictional velocity, $u_* = \sqrt{\tau/\rho}$, where τ is surface wind stress from the daily QuikSCAT and ASCAT products (Fig. 2.16). $\overline{K_v}$ is significantly correlated with u_*^3 with a correlation coefficient $R = 0.41$ ($p < 0.01$). This correlation is increased ($R = 0.54$; $p < 0.01$) if data points where the corresponding value of the PEA residual is larger than $-20 \, \mathrm{J \, m^3 \, month^{-1}}$ are excluded ($20 \, \mathrm{J \, m^{-3} \, month^{-1}}$ is roughly equivalent to an error in Q_{net} of $30 \, \mathrm{W \, m^{-2}}$).

Except for low diffusivity in the central North Pacific, estimated summertime diffusivities in the seasonal boundary layer are consistent with values derived from the budget analyses of potential vorticity (2–$5 \times 10^{-4} \, \mathrm{m^2 \, s^{-1}}$; Qiu et al. 2006), dissolved oxygen ($1.7 \times 10^{-4} \, \mathrm{m^2 \, s^{-1}}$; Sukigara et al. 2011) and heat and salt (1–$3 \times 10^{-4} \, \mathrm{m^2 \, s^{-1}}$; Cronin et al. 2013; Cronin et al. 2015) in the northwestern Pacific subtropical recirculation gyre and the northeastern subpolar gyre. Moreover, the gradual decrease in diffusivity as stratification below the ML develops toward late summer is consistent with the result of Cronin et al. (2015).

Good agreement between diffusivities estimated in this work and estimates from previous studies indicated that the residual in the PEA budget is attributed mainly to the vertical mixing term, suggesting in turn that the assumptions made to estimate the RHS of Eq. 2.7 are valid. However, it is to be noted again that this estimated $\overline{K_v}$ include various uncertainties, such as the error in estimates of the surface buoyancy flux. Indeed, the positive residual values shown in Fig. 2.15 cannot be explained through the vertical mixing process. As a possible cause, contribution from time-varying currents on shorter time scale than monthly and smaller spatial scale than $1° \times 1°$ might be underestimated in the strong current regions, such as the western boundary and equatorial current system (c.f., Fig. 2.11a–c). Indeed, the importance of time-varying currents in contributing to the upper-ocean heat content changes has been emphasized by several previous

studies focusing on the Kuroshio Extension region (e.g., Qiu and Kelly 1993; Vivier et al. 2002).

2.5 Discussion

Seasonal stratification in the North Pacific develops from a vertical one-dimensional energy balance, except in regions with strong current (Fig. 2.11) and it is suggested that the development of seasonal stratification is strongly associated with the seasonal cycle of buoyancy forcing (Fig. 2.6). In this section, we examine the detail of the local PEA balance to reveal the relative contribution of oceanic lateral processes, and to investigate the influences of difference in the composition of atmospheric buoyancy forcing.

We set three boxes as each representative example (Fig. 2.11d); one is in Kuroshio extension region (150–160°E, 32–37°E; KE box) and the other two boxes are located on northern and southern part of the North Pacific away from the strong current regions (North box: 179°E–176°W, 40°–45°N; South box: 179°E–176°W, 20°–25°N). The accumulated ocean buoyancy gains and its composition for the three regions are shown in Fig. 2.17. The latter two regions have similar values of the accumulated ocean buoyancy gains during the development phase of the seasonal stratification. However, their compositions are quite different, suggesting meridional differences in the PEA balance. The penetrating shortwave radiation and the non-penetrating components are both positive in the North box (Fig. 2.17b), whereas in the South box the non-penetrating component is negative, indicating ocean buoyancy loss (Fig. 2.17c). Averaged over each region, August PEA is 196.6 J m^{-3} for the North box, 128.9 J m^{-3} for the South box, and 383.0 J m^{-3} for the KE box (c.f. Fig. 2.2). It should be noted that a simple comparison of these PEA estimates for each region may be difficult to interpret due to the difference in the annual maximum of ML depth (H) used in the calculation. Hence, we instead here focus on comparing the balance of terms in the PEA budget between regions.

Figure 2.18 shows the time series of the PEA budget averaged over each region. Only in the KE box does PEA advection play a significant role in the development of seasonal stratification (Fig. 2.18a). Since higher PEA waters are carried into the region from upstream of the Kuroshio current, the PEA advection term also peaks late in the developing phase. As a result, PEA development peaks one month later than the buoyancy gain. In August, PEA advection contributes to ~41% of the time rate change in PEA.

Comparing the North and South boxes (Fig. 2.18b, c), the PEA budgets show a fundamental difference in the balance, although their net buoyancy gains are similar. In the North box, the dominant contribution from the non-penetrating buoyancy flux (term D in Eq. 2.7) controls the

19

seasonal cycle, and the penetrating shortwave radiation (term E) term and the vertical mixing term (residual) are nearly balanced. On the other hand, in the South box, since the non-penetrating buoyancy term is negative (except for June), the PEA cannot increase through the warming season as it does for the North box. Note that the negative non-penetrating buoyancy term at the surface here does not imply vertical mixing within the surface layer. Since the relative size of the residual term (assumed to be the contribution of vertical mixing) to the time rate of change in PEA is not significantly different between the North box and the South box, this difference in the PEA term balance is attributed to the difference in the component of buoyancy forcing, rather than the local vertical mixing intensity. That is, even if the total buoyancy gain would be same, a condition that the non-penetrating component also contributes to the total buoyancy gain—as is the case in the northern North Pacific (Fig. 2.11d)—is more favorable for the formation of more intense PEA stratification. According to the definition of PEA (PEA becomes larger in vertically sharper stratification if H is the same), this means that the sharper seasonal stratification tends to be formed in the northern North Pacific. These results emphasize the important influence of the "composition" of buoyancy forcing, in addition to the "total magnitude", on the development of seasonal stratification.

2.6 Summary

Based on the Argo profile data and atmospheric buoyancy/momentum flux data derived mainly from satellite observations, we investigated the development of the seasonal stratification in the North Pacific. Applying the concept of PEA, which has historically been used in studies of coastal and shelf seas (e.g. Gronholz et al. 2017), to the seasonal stratification of the open ocean, we have quantitatively described the development of the seasonal stratification. Using PEA as a metric to represent the stratification, and by analyzing its budget, we have estimated the contribution of lateral processes and vertical mixing as the residual. Both contributions would have been difficult to quantify by using other previous metrics.

The PEA budget analysis shows that the seasonal stratification develops under a vertical one-dimensional energy balance between the atmospheric buoyancy forcing and the vertical mixing in the water column over a large part of the North Pacific, except for the Kuroshio/Kuroshio Extension and equatorial current system south of 10°N. In the Kuroshio Extension region, a significant part of the time rate of change in PEA can be attributed to the advection of PEA. A comparison of PEA term balance suggests that the dominance of non-penetrating component in the buoyancy forcing is favorable for the development of sharper

stratification in the northern North Pacific. It is worth emphasizing that the composition of buoyancy forcing, in addition to its magnitude, is also important for forming the upper-ocean stability during the warming season that affects the physical and biogeochemical processes through controlling the vertical mixing.

The vertical diffusivity, depth-averaged over the seasonal boundary layer and estimated from the residual of the energy budget, ranging from 5×10^{-5} m^2 s^{-1} to 5×10^{-4} m^2 s^{-1}. This range is consistent with previous indirect estimates for other independent tracers (e.g., potential vorticity), which gives us confidence in these estimates. The diffusivity shows significant spatial and seasonal variability, indicative of its dependence on the strength of local wind forcing during the warming season. Pertinent to the discussion of vertical mixing under a stabilizing buoyancy force, recent observational and LES studies have shown that the oceanic response to wind forcing is latitude-dependent, due to the Coriolis parameter (Goh & Noh 2013; Lee at al. 2015; Yoshikawa 2015). Moreover, modeling studies have demonstrated that the wind energy input to near-inertial motion contributes to the near-surface mixing (Furuichi et al. 2008; Jochum et al. 2013). In this chapter, the contribution from the directly wind-induced mixing and the mixing associated with the near-inertial energy are included in the residual term of the PEA budget. It is difficult, however, to identify the mechanisms responsible for the vertical mixing due to its large uncertainty and errors from other terms. Further studies are thus needed to explain quantitatively the spatial distribution of the vertical diffusivity in the seasonal boundary layer and its impact on the sea surface temperature development and biogeochemical processes during the warming season.

Appendix 2A: Attenuation coefficient of shortwave radiation

As discussed in Section 2.4 and 2.5, the penetration of the shortwave radiation plays an important role on the development of the seasonal stratification. However, it is implied that the calculation of the penetration of the shortwave radiation is strongly depend on the choice of the model for computation of the attenuation coefficient. In order to examine the robustness of results in this chapter, we here briefly compared the model used in this chapter (Eq. 2.9; Lee et al. 2005) with widely used classical model based on the water type classification (Jerlov 1968; Paulson & Simpson 1977).

Figure A 2.1 shows the meridional changes in the vertical profiles of the attenuation coefficient and corresponded penetrating shortwave radiation along the dateline. While the attenuation coefficient from classical model has constant value, those from Lee et al. (2005) decrease with the depth at all latitudes (Fig. A 2.1left). The attenuation coefficient used in this

chapter increase with the latitude, reflecting that subpolar (high-latitude) water is more turbid due to high productivity. By the vertical variation in the attenuation coefficient, there is tendency that the penetration of shortwave radiation converges at shallower depth in high-latitude and reaches to deeper layer in low-latitude compared to the case of constant attenuation coefficient (Fig. A 2.1ceanter and right).

However, these differences have little impacts on the PEA balance in the budget during the warming season. We show the contribution of penetrating shortwave radiation in the PEA budget (Term E of Eq. 2.7) calculated using above two models for the attenuation coefficient in Fig. A 2.2. Reflecting the above-mentioned differences in vertical profile of the penetration, Fig A 2.2 shows that slightly large (small) contribution of shortwave radiation in higher (lower) latitude regions in the case using the attenuation coefficient based on the inherent optical properties of seawater. On the other hand, it is also indicated that the results and conclusions shown in previous chapter are qualitatively unchanged using different model.
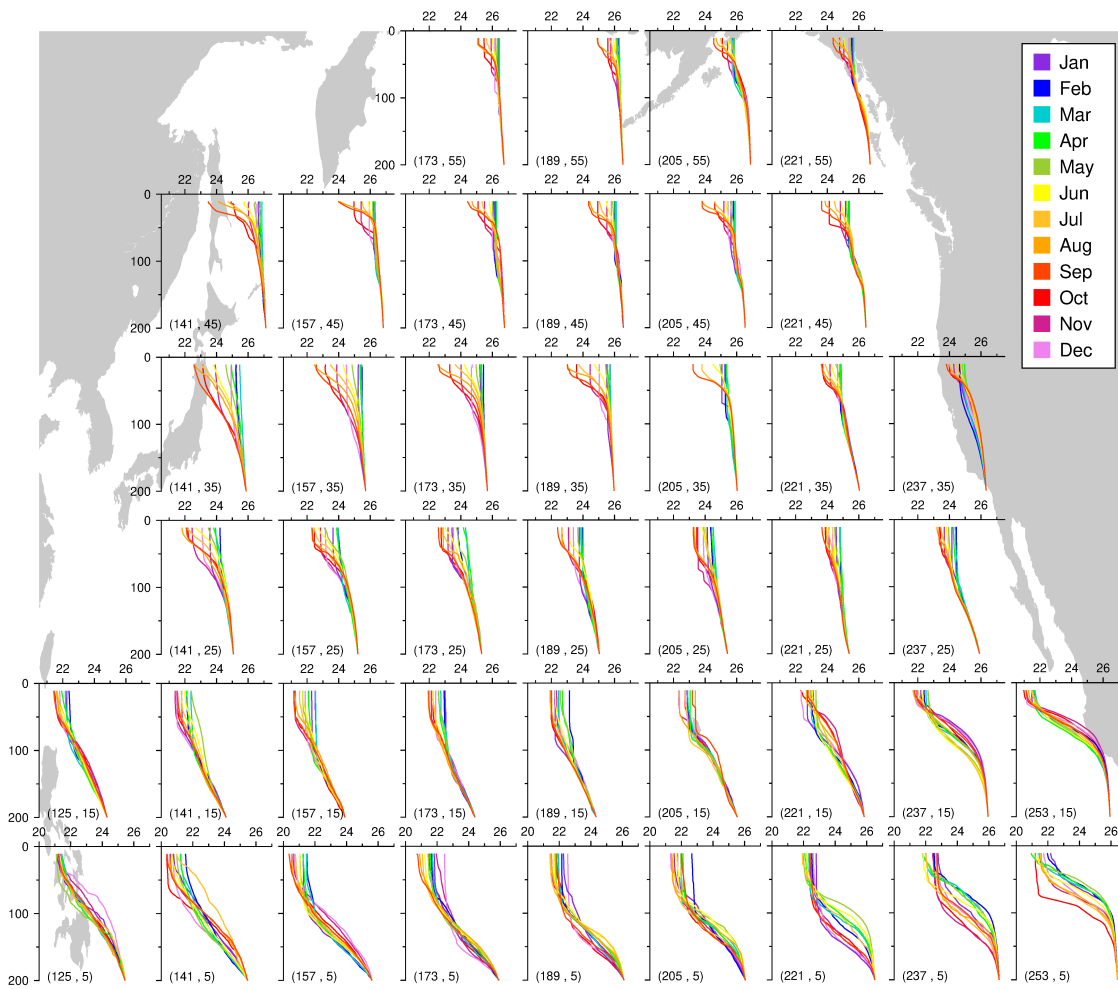
Figure 2.1. Seasonal cycle of the upper-ocean potential density stratification in the North Pacific, based on Argo data sampled during 2006–2016 (y axis: depth [m], and x axis: potential density [kg m^{-3}]). Profiles are averaged over a 2°(longitude) × 2°(latitude) region centered at labeled location (longitude [°E], latitude [°N]). Averaged profiles are normalized to the potential density at 200 m in February following the procedure of Moisan & Niller (1998).
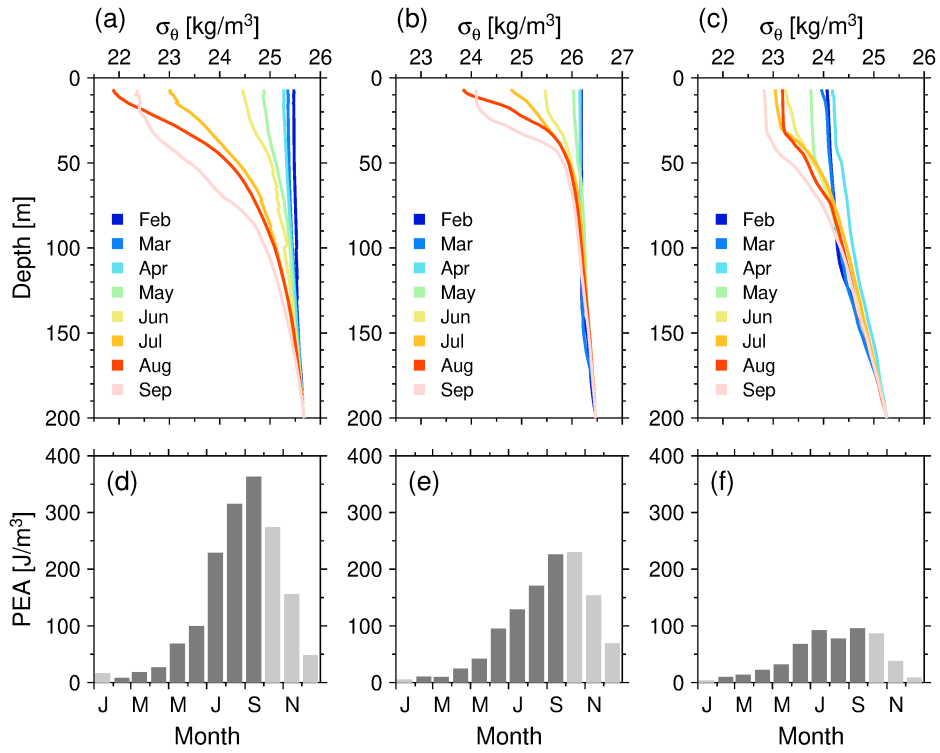
Figure 2.2. Examples of the potential energy anomaly (PEA) calculation. (a–c) Seasonal cycle of the upper-ocean profile of potential density stratification at (a; 153°E, 35°N), (b; 177°W, 43°N), and (c; 177°W, 23°N). (d–f) Corresponding seasonal cycle of PEA with the annual maxima of ML depth (H) set to (d) 144 m, (e) 163 m, (f) 88 m, respectively.
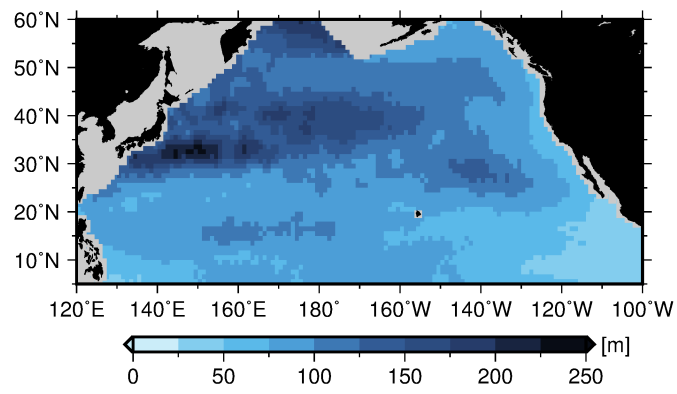
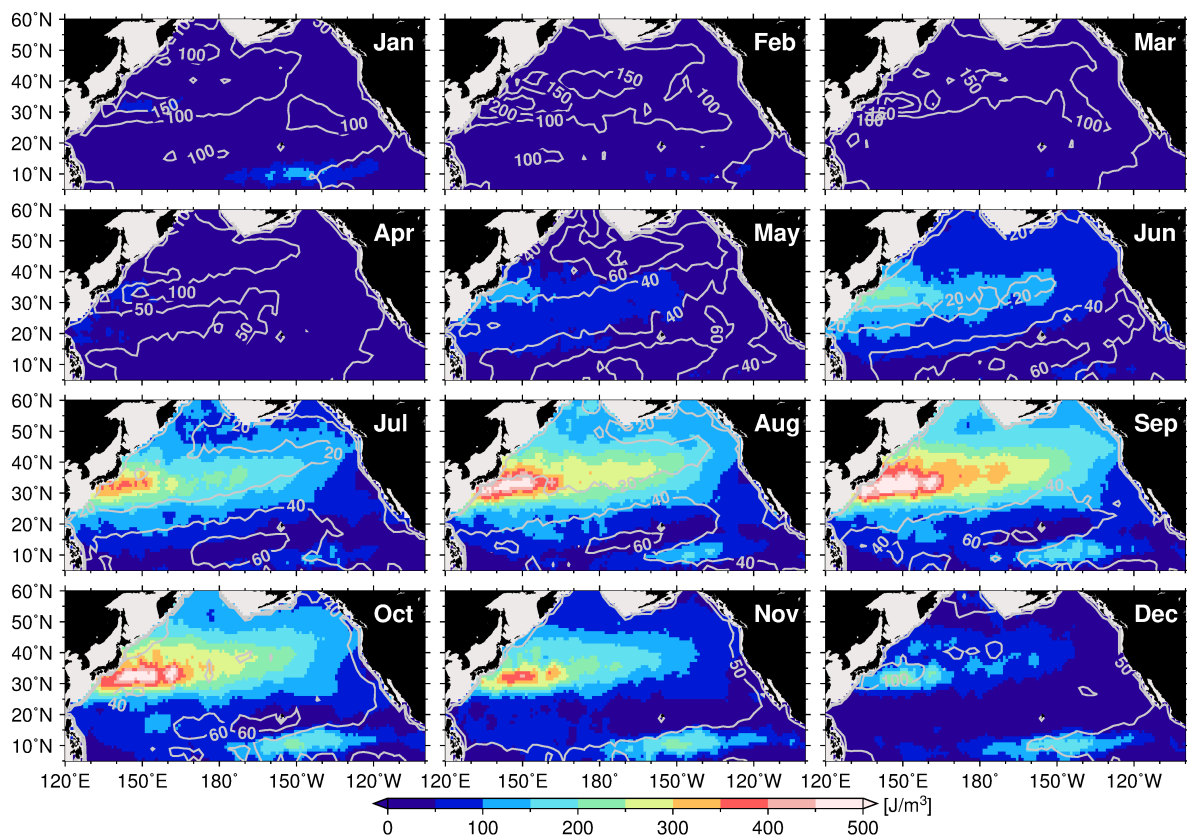Figure 2.3. Spatial distribution of the annual maximum of mixed layer depth (i.e., the seasonal boundary layer depth), *H* (m).

Figure 2.4. Seasonal cycle of PEA (J m^{-3}; color) and the mixed layer depth (m; gray contours). The mixed layer depth contour interval is 50 m for November–April and 20 m for May–October.
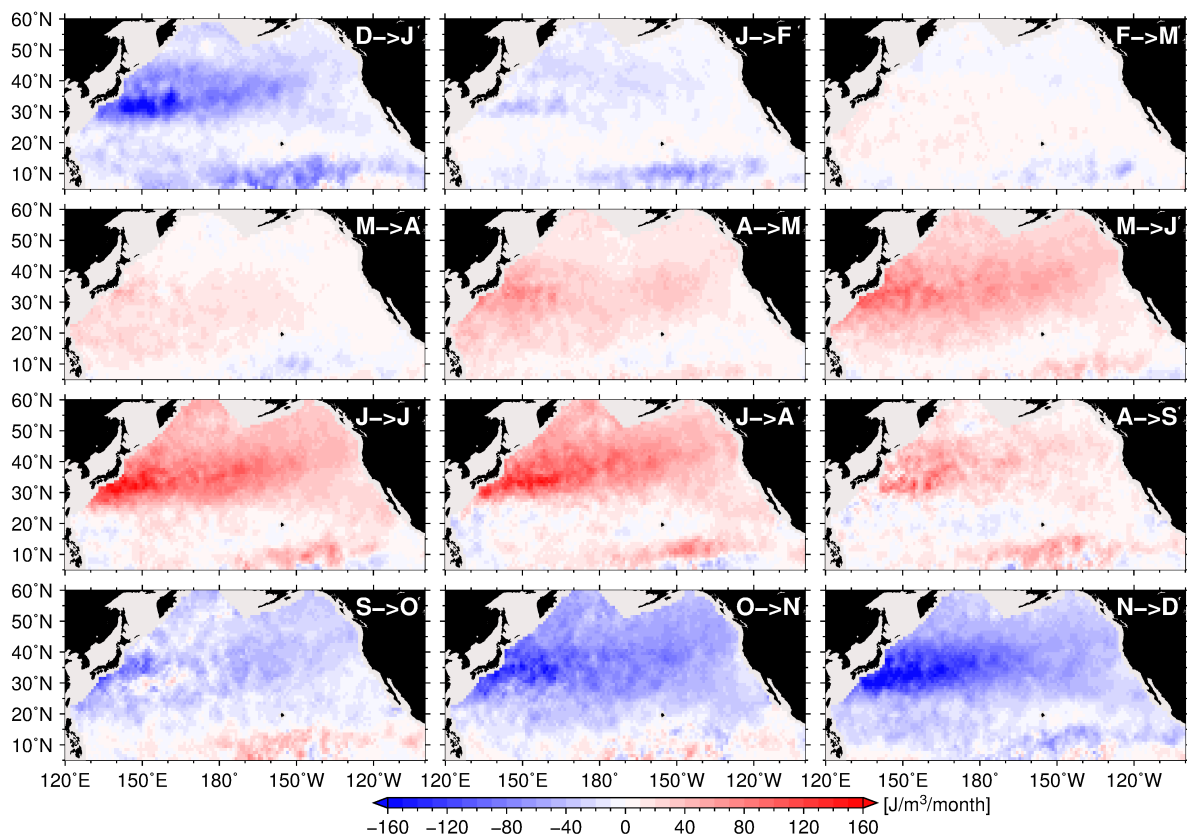
Figure 2.5. Maps of the month-to-month change in PEA (J m^{-3} month^{-1}). The change is defined as the difference from the previous month.
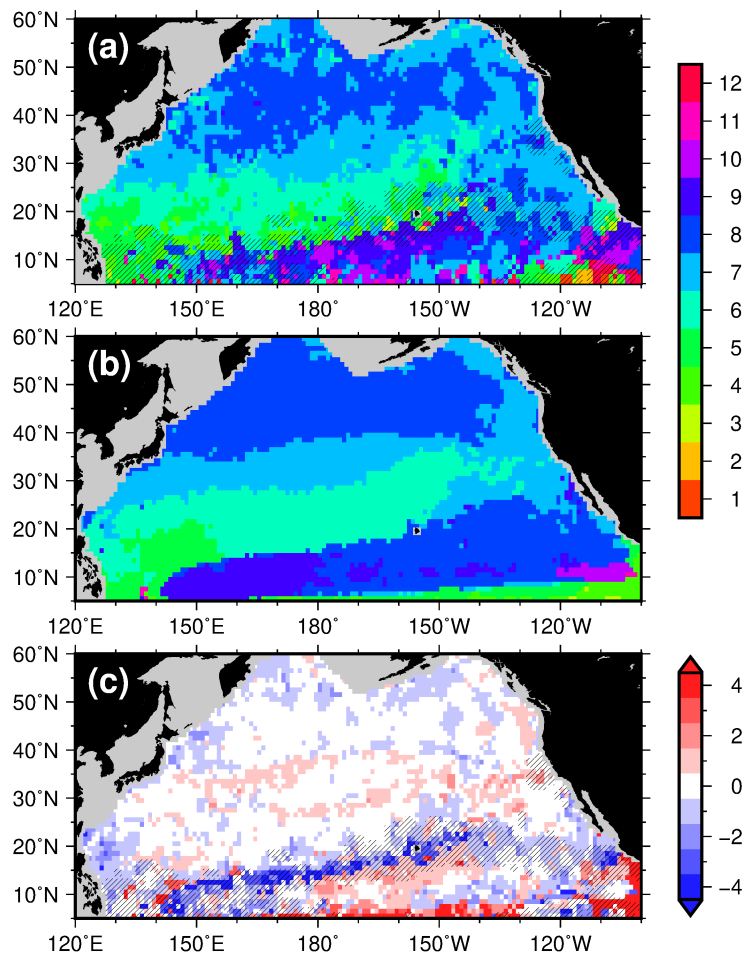
Figure 2.6. Month of maximum increase in (a) PEA and (b) net buoyancy gain. (c) Difference between (a) and (b), [i.e., (a) − (b)]. Black hatching indicates regions where the annual maximum of PEA increase is less than 20 J m^{-3} month^{-1}.
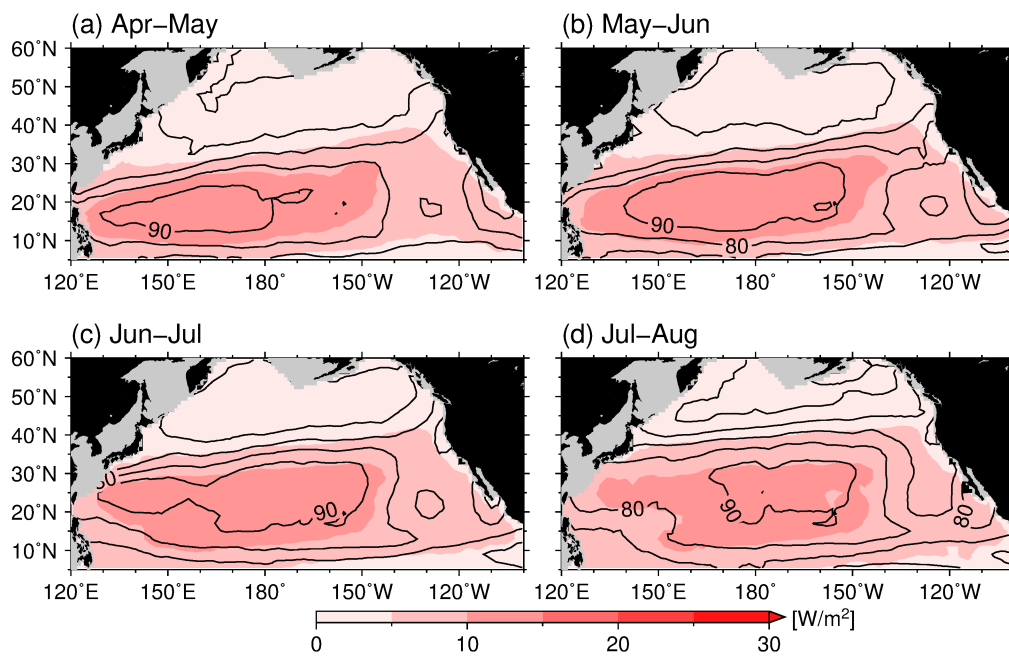
Figure 2.7. Spatial distribution of the penetrating shortwave radiation (W m^{-2}) at 40 m depth (color) and at the surface (black contours) for (a) April–May, (b) May–June, (c) June–July, and (d) July–August. Positive values indicate a downward flux.
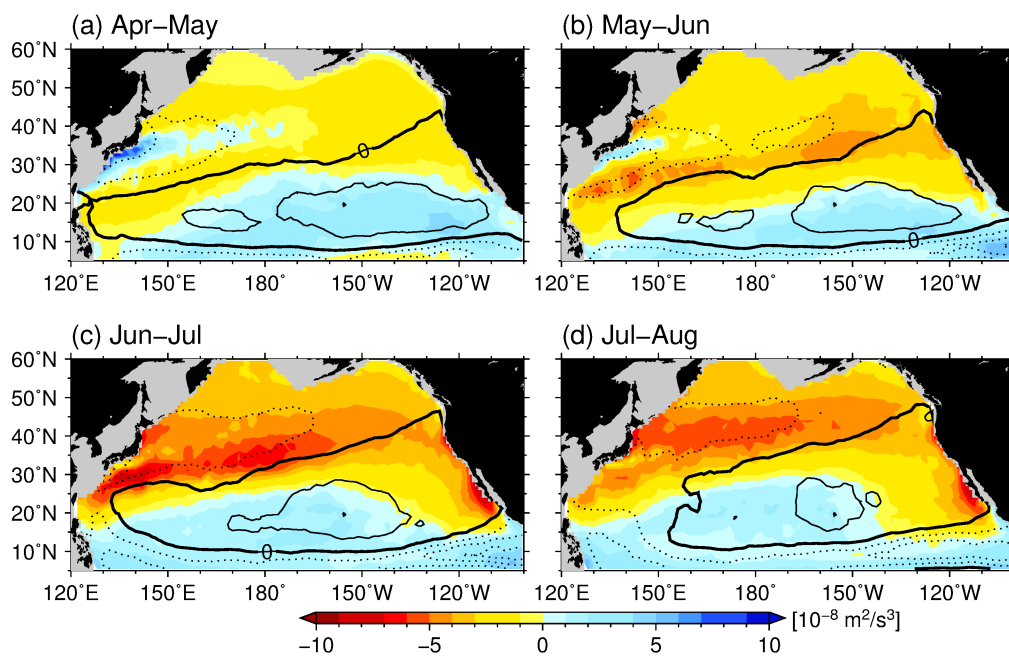
Figure 2.8. Spatial distribution of heat (color shade; first term of RHS in Eq. 2.10) and freshwater (black contours; second term of RHS in Eq. 2.10) components of the surface non-penetrating buoyancy flux (10^{-8} m^2 s^{-3}) for (a) April–May, (b) May–June, (c) June–July, and (d) July–August. Solid (dash) lines indicate positive (negative) values and the contour interval is 1×10^{-8} m^2 s^{-3}. The negative values indicate net ocean buoyancy gain.
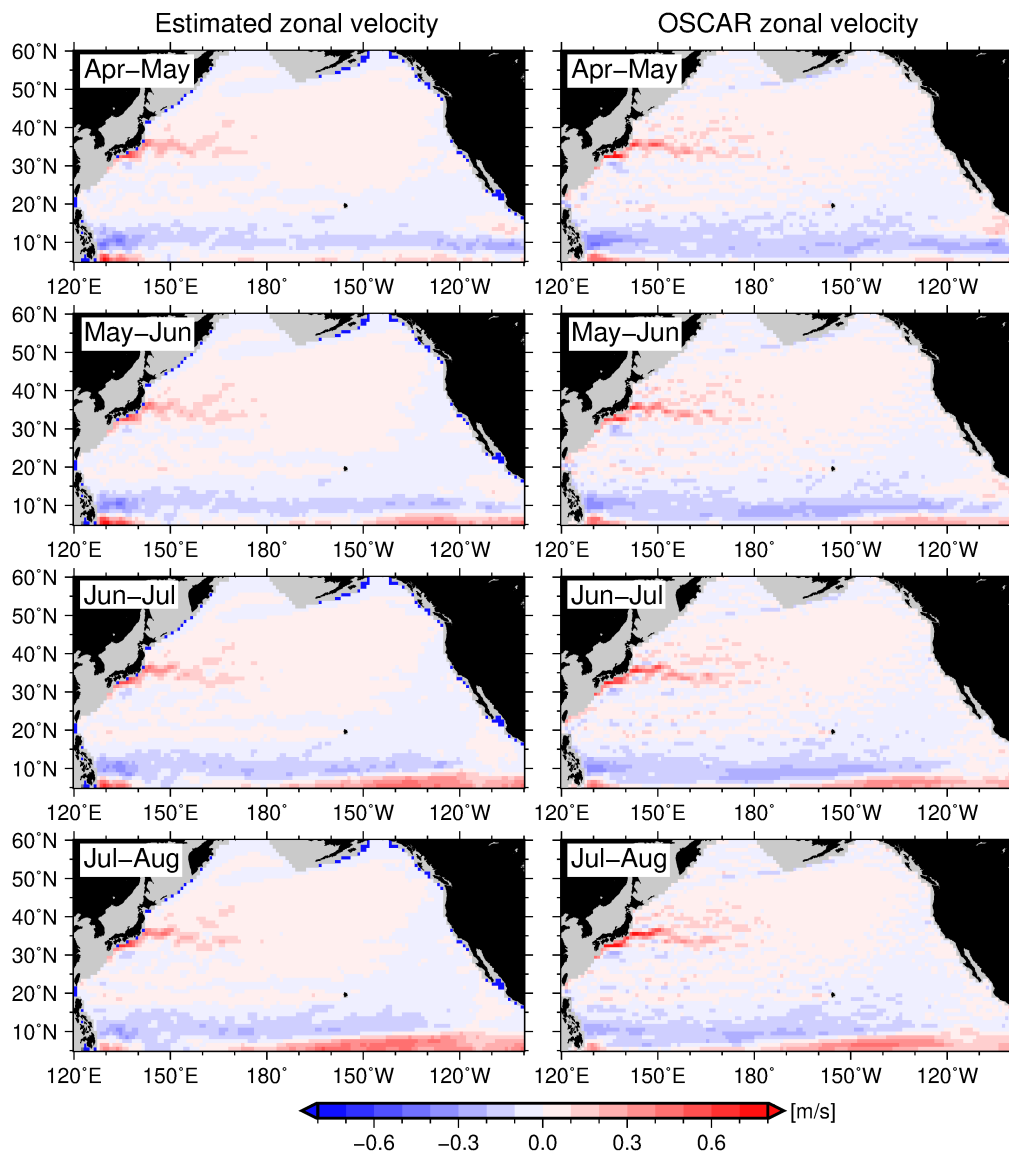
Figure 2.9. Comparisons of zonal velocity at 15 m depth between the estimated velocity field and the velocity field from the Ocean Surface Currents Analyses Real-time (OSCAR: Bonjean & Lagerloef 2002).
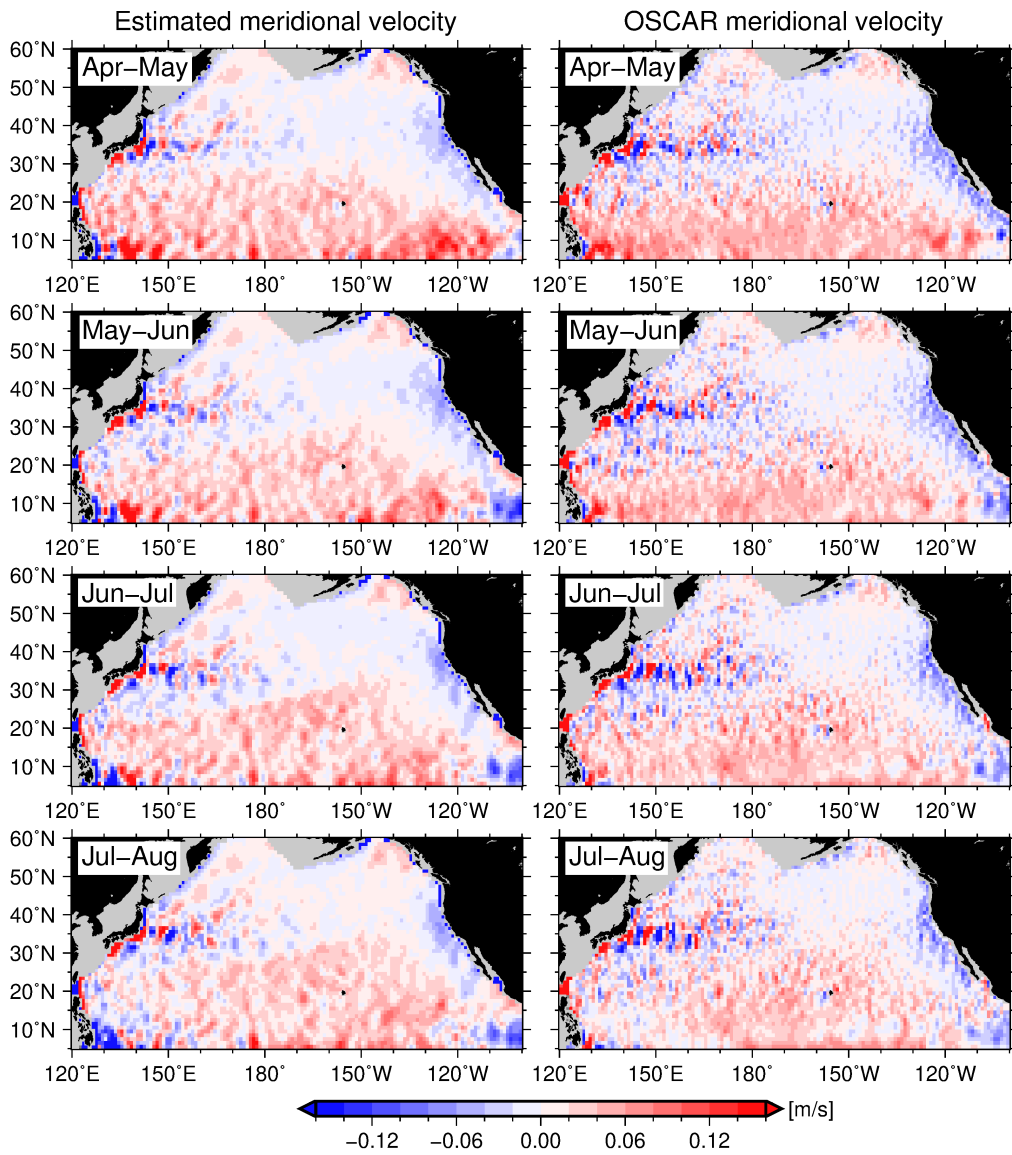
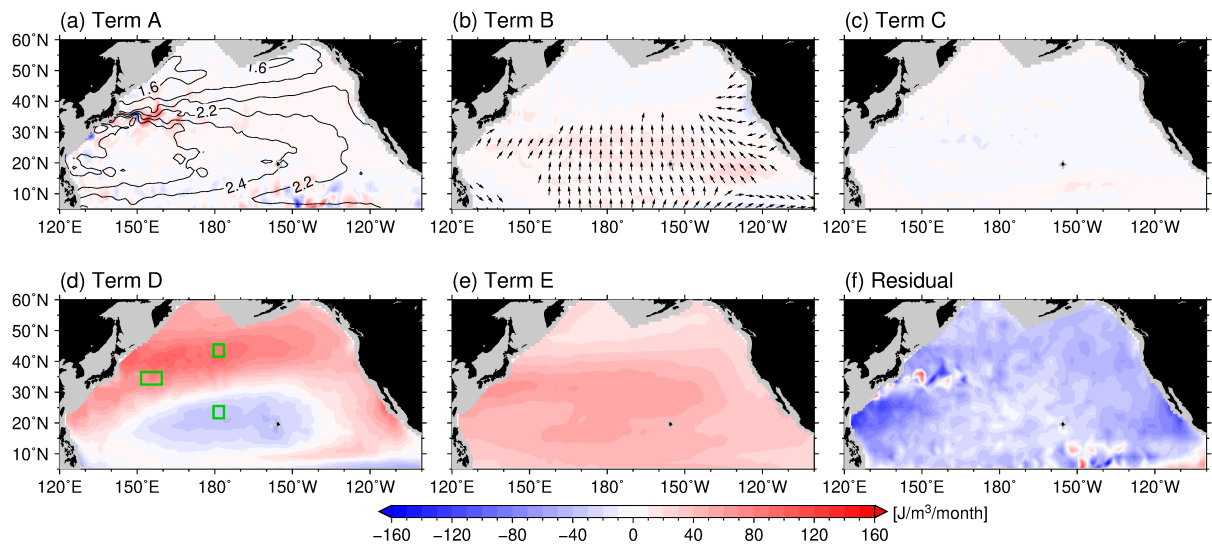Figure 2.10. Same as Fig. 2.9, but for the meridional velocity.

32

Figure 2.11. Spatial distribution of the contributions to the PEA budget in July–August: (a) PEA advection term overlain by the mean dynamic height (dyn-m; contours); (b) Depth-mean straining term with Ekman current vectors at 10 m depth (shown for values larger than 3 m s^{-1} and with constant vector length); (c) Non-mean straining term; (d) Non-penetrating buoyancy flux term; (e) Penetrating shortwave radiation term; (f) Residual term. Green boxes in (d) indicate the locations discussed in Section 2.5 (Figs. 2.17 and 18).
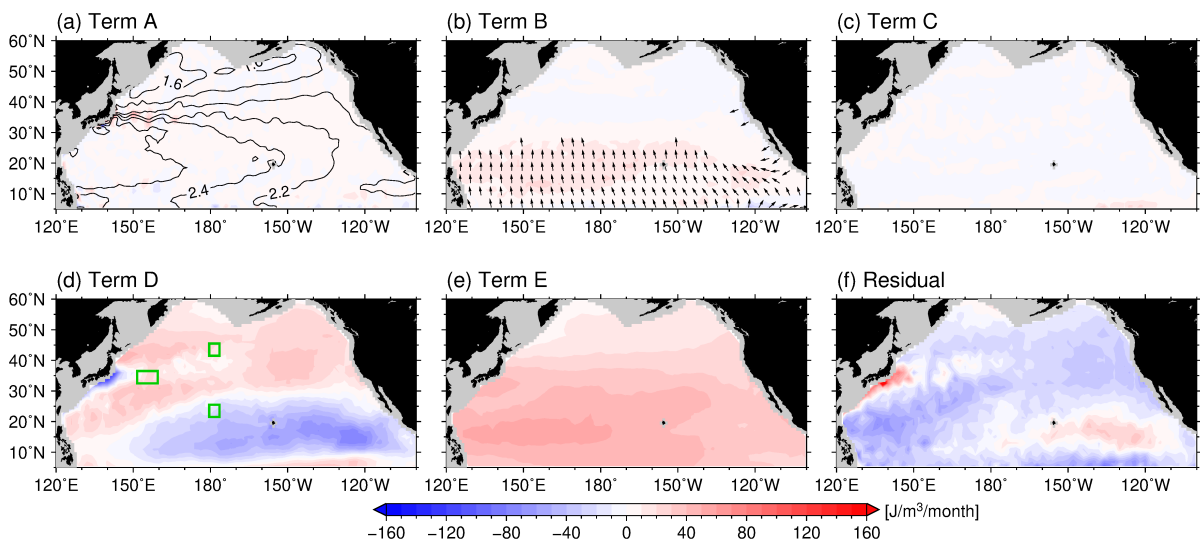
Figure 2.12. Same as Fig. 2.11, but for the PEA budget in April–May.
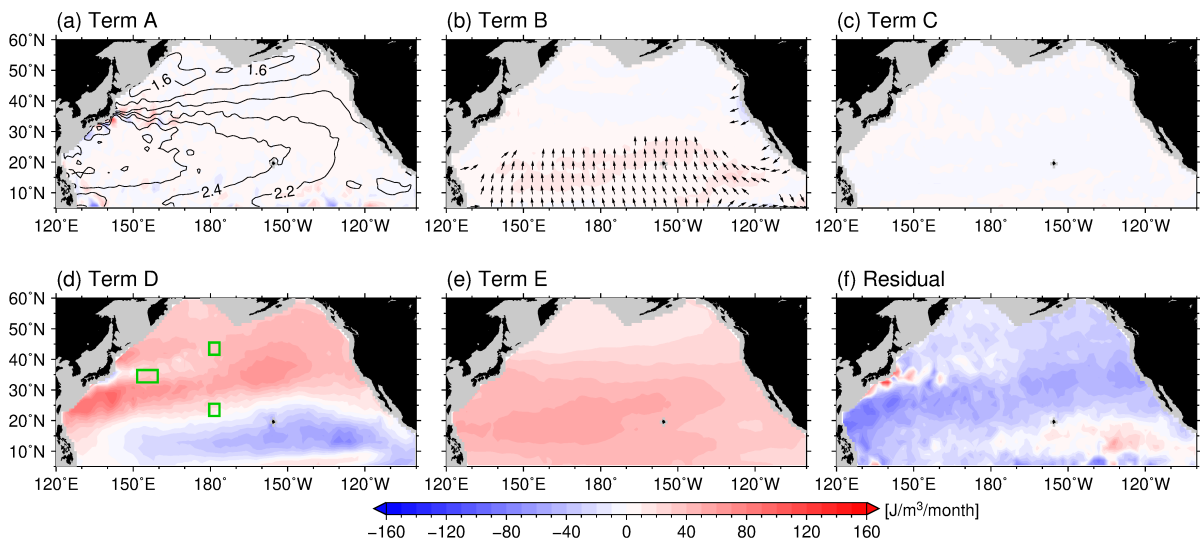
Figure 2.13. Same as Fig. 2.11, but for the PEA budget in May–June.
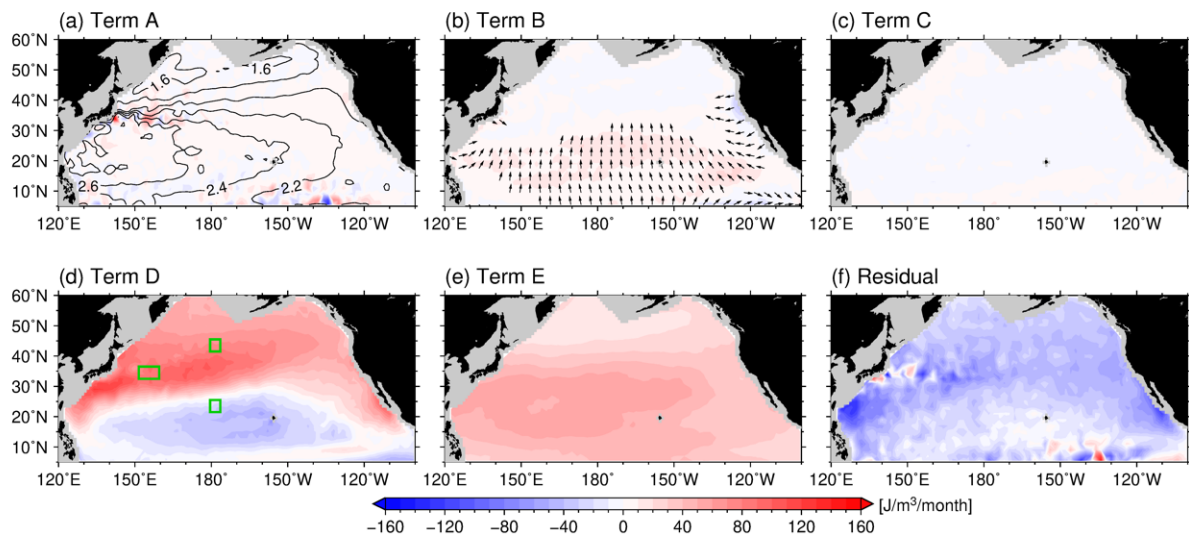
Figure 2.14. Same as Fig. 2.11, but for the PEA budget in June–July.
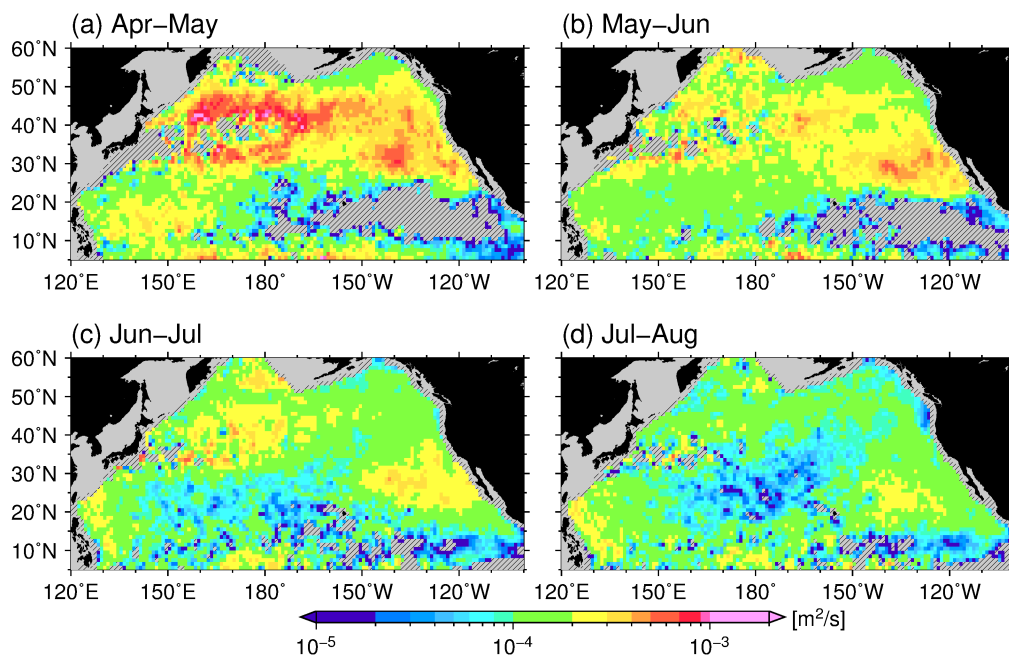
Figure 2.15. Spatial distribution of depth-averaged vertical diffusivity, $\overline{K_v}$ (m^2 s^{-1}), for (a) April–May, (b) May–June, (c) June–July, and (d) July–August. Gray hatching indicates regions with positive residuals.
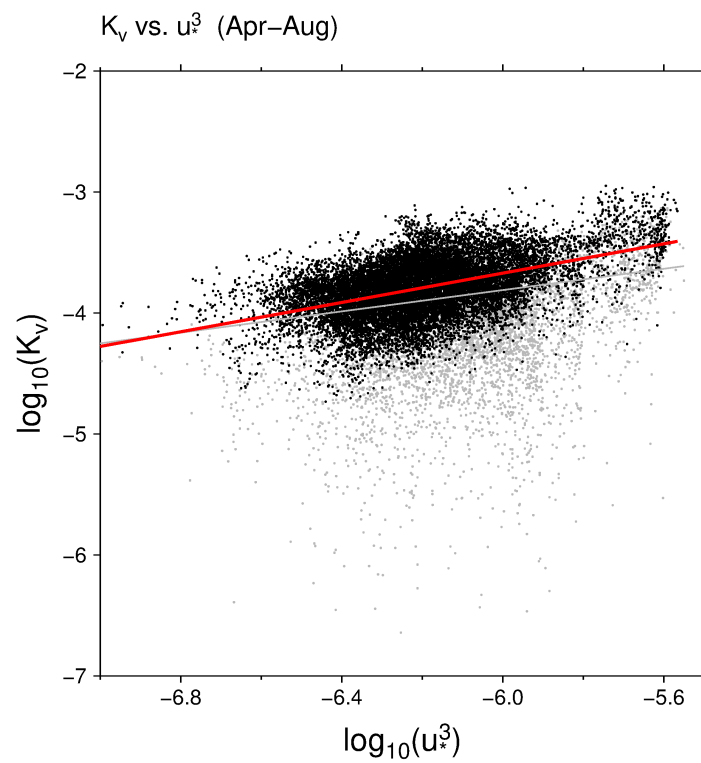
Figure 2.16. Scatter plot of the logarithm of depth-averaged vertical diffusivity, $\overline{K_v}$, and logarithm of the cube of frictional velocity, u_*, for April–August. Data points with a corresponding PEA residual term greater than -20 J m^{-3} month^{-1} are shown in gray. The gray line is the least squares fit for all data points, whereas the red line is the least squares fit for data points colored black.
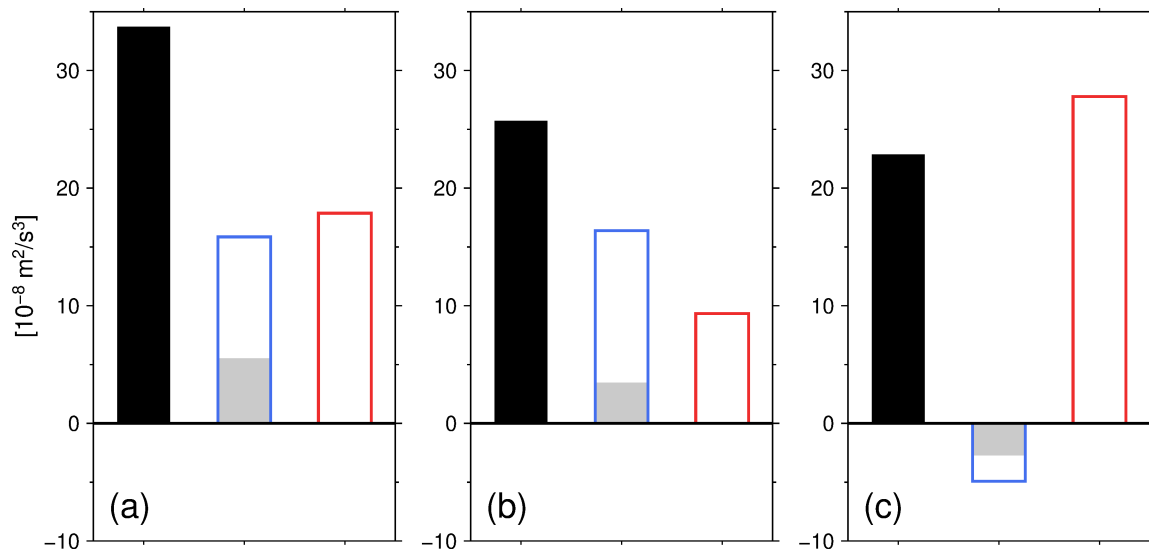
Figure 2.17. Accumulated April–August oceanic buoyancy gain (10^{-8} m^2 s^{-3}; black bars) and its components for the (a) KE box (b) North box, and (c) South box. The blue (red) bars indicate non-penetrating (penetrating) components of oceanic buoyancy gain. Gray bars within blue bars show the freshwater component of the non-penetrating buoyancy gain.
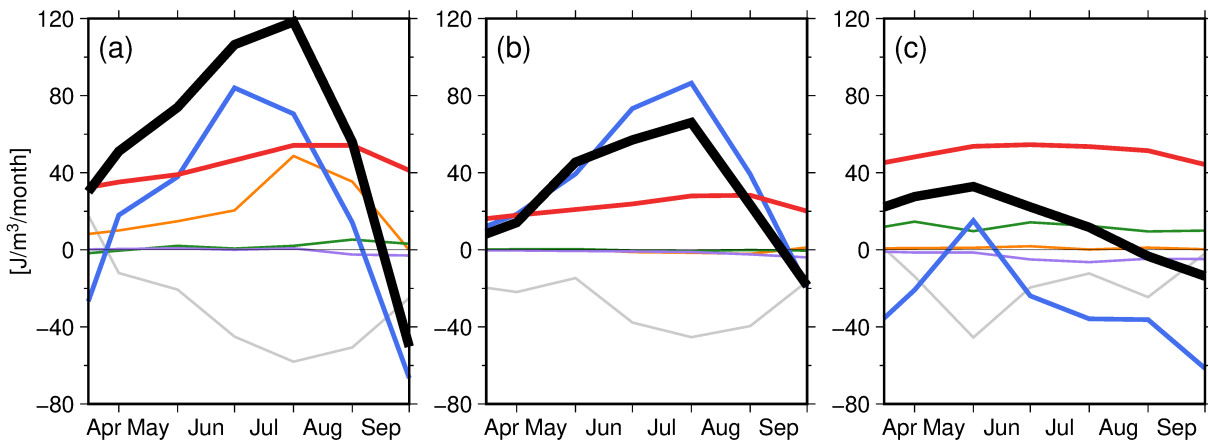
Figure 2.18. April–September time series of time rate change in PEA (J m^{-3} month^{-1}; black line) and each term in the PEA budget (Eq. 2.7) for the (a) KE box, (b) North box, and (c) South box. Terms shown are the PEA advection term (orange line), the depth-mean straining term (green line), the non-mean straining term (purple line), the non-penetrating buoyancy flux term (blue line), the penetrating shortwave radiation term (red line), and the residual term (gray line).
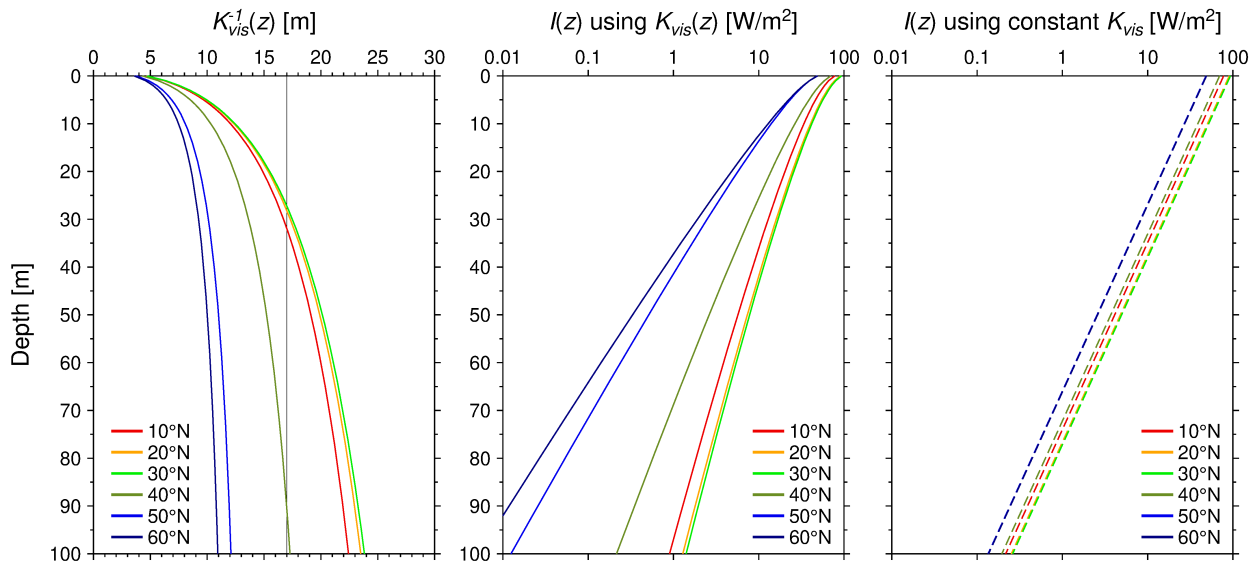
Figure A 2.1. Vertical profiles of the attenuation coefficients for the visible domain of shortwave radiation (K_{VIS}) and the penetrating shortwave radiation (I) along the dateline in August. The vertical profiles of I are computed from Eq. 2.8 with use of (center) the attenuation coefficient of Eq. 2.9 and (right) the constant attenuation coefficient of water type 1B after Jerlov (1968) (K_{VIS}^{-1} =17 m: Paulson & Simpson 1977).
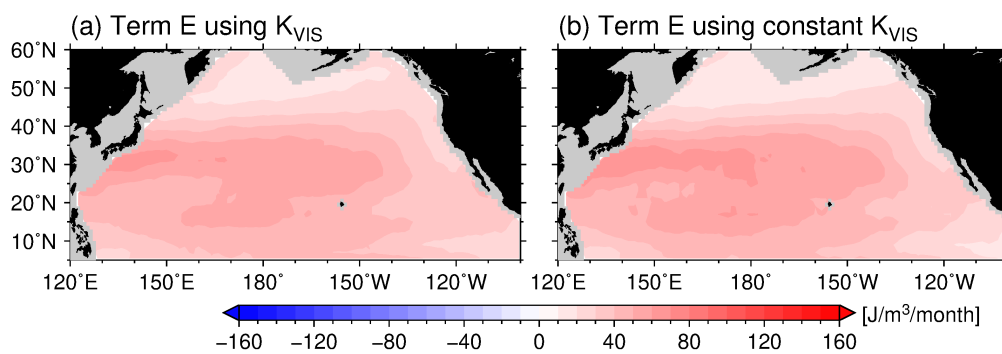
Figure A 2.2. Comparison of Term E of Eq. 2.7 calculated (a) using the attenuation coefficient from the generalized empirical model based on the inherent optical properties of seawater (same as Fig. 2.11e) and (b) using constant attenuation coefficient of Jerlov water type 1B (K_{VIS}^{-1} =17 m: Jerlov 1968; Paulson & Simpson 1977).

Chapter 3
An estimation of the sea surface Potential Vorticity (PV) flux and its interannual variability

3.1 Introduction

Potential vorticity (PV) is a central concept for describing the large-scale characteristic of the ocean in physical oceanography. Under the Boussinesq approximation, PV (Ertel's PV) is written as

$$Q = -\frac{1}{\rho}\boldsymbol{\omega} \cdot \boldsymbol{\nabla}\sigma, \tag{3.1}$$

where ρ is in situ seawater density,

$$\boldsymbol{\omega} = \mathbf{f} + \boldsymbol{\nabla} \times \mathbf{u} \tag{3.2}$$

is the sum of planetary vorticity ($\mathbf{f}$) and relative vorticity ($\boldsymbol{\nabla} \times \mathbf{u}$), and σ is the potential density of seawater (e.g., Vallis 2006). Traditionally, PV has been used to depict a picture of the ocean circulation from the theoretical perspective, resulting in our understanding of how the ocean is set into motion (e.g., Luyten et al. 1983). On the other hand, in observational studies, PV plays an important role as a tracer of water mass subducted from the sea surface into the ocean interior, associated with ocean ventilation process, with consequences for the oceanic uptake of heat, carbon, and oxygen (e.g., Talley 1988; Suga et al. 1989).

An advantage of the use of PV as a tracer of water mass comes from the widely recognized theorem of "Impermeability" of PV (Haynes & McIntyre 1987). According to the theorem, PV cannot cross an isopycnal surface and is exactly conserved in an isopycnal layer. Moreover, the source and sink of PV in an isopycnal layer are allowed only by interaction with the atmosphere at the sea surface or with topography at the boundary. Therefore, tracking PV signals formed by air-sea interaction at the surface mixed layer, we can acquire knowledge about the formation and circulation pathway of the water mass in the ocean interior. Because the formation of water mass is directly associated with oceanic PV extraction by the atmosphere during the cooling season, PV framework is also used for quantification of the formation rate of the Eighteen Degree Water (EDW) and shows its availability in the North Atlantic (Maze & Marshall 2011).

The PV exchange process at the sea surface is more important for the total variation in PV in an isopycnal layer than those by topographic friction at the boundary (Deremble et al. 2014). In general, the ocean is thought, from the traditional view by quasigeostrophic layered model works, to lose PV mechanically by the atmosphere due to anticyclonic wind stress curl over the

subtropical gyre. And, the lost oceanic PV should be compensated by the frictional PV gain at the western boundary and the bottom of the ocean (e.g., Hughes & de Cuevas 2001) or the sea surface PV gain from the atmosphere by cyclonic wind stress curl (e.g., Marshall 1984). Air-sea buoyancy flux is also believed to be an important driver of surface PV exchange. Surface cooling and evaporation (i.e., buoyancy flux from the ocean to the atmosphere) is a mechanism of PV loss and, conversely, oceanic buoyancy gain (surface heating and precipitation) is a mechanism of PV gain. In addition, a recent study pointed out that wind-driven surface mixing is an important mechanism of PV extraction from the ocean (Deremble & Dewar 2012). In this way, PV exchange at the sea surface has been discussed for a long time and is understood as being attributed mechanically and diabatically. However, quantitative estimations of the sea surface PV flux have done mostly from the model output and those from the observational dataset is relatively limited. A reasonable description of the sea surface PV exchange process from an observational perspective is needed for better understanding the water mass formation in the real ocean, consequently, providing better knowledge about ocean dynamics as well.

Among few studies for observational estimation of sea surface PV flux, Czaja & Hausmann (2009) showed climatological features of the PV flux in the Northern hemisphere calculated from observations using some scaling laws. However, it was reported that these bulk estimation from the observational dataset with scaling laws potentially shows PV gain bias (Deremble et al. 2014). Some improvements and its validation of the methodology are thought to be needed for reasonably estimating the sea surface PV flux from observations. In this study, we attempt to improve the previously proposed method of estimation for sea surface PV flux from observations, and then the new method is validated with independently calculated PV variation of the ocean interior. The rest of this paper is organized as follows. In Section 3.2, we present a brief review of PV framework and show estimation method of the sea surface PV flux and validation of the flux. We describe, in Section 3.3, the feature of estimated surface PV flux in terms of Isopycnal averaging and discuss the relationship with subduction rate. Interannual variability of the PV flux is discussed in Section 3.4. Finally, the summary is offered in Section 3.5.

3.2 Sea surface PV flux calculation

PV flux at the sea surface has formalized by many previous studies (e.g., Marshall & Nurser 1992; Marshall et al. 2001), and then the global estimate of them from observations have been evaluated based on some assumptions and proposed scaling laws (Czaja & Hausmann 2009; Olsina et al. 2013). In this section, we make a brief review of the framework and proposed estimation method

of PV flux in order to introduce our strategy of improvements of the method.

Following Marshall & Nurser (1992), the flux form of conservation equation of PV defined by Eq. 3.1 is written as

$$\frac{\partial(\rho Q)}{\partial t} + \boldsymbol{\nabla} \cdot \mathbf{J} = 0, \tag{3.3}$$

where the vector $\mathbf{J}$ is generalized PV flux vector. Although one can represent $\mathbf{J}$ in several ways, here, it is written as the sum of an advective flux and three nonadvective contributions (see Marshall et al. 2001),

$$\mathbf{J} = \rho Q \mathbf{u} + \boldsymbol{\omega} \frac{D\sigma}{Dt} + \mathbf{F} \times \boldsymbol{\nabla}\sigma + \frac{\Phi}{\rho_0} \boldsymbol{\nabla}\rho \times \boldsymbol{\nabla}\sigma. \tag{3.4}$$

In Eq. 3.4, $\mathbf{u}$ is three-dimensional velocity, $\mathbf{F}$ denotes the nonconservative frictional force per unit mass, ρ_0 is reference density, and Φ is the geopotential. The first nonadvective term $\boldsymbol{\omega}\frac{D\sigma}{Dt}$ (absolute vorticity multiplied by the Lagrangian derivative of potential density) indicates diabatic PV forcing. The second nonadvective term $\mathbf{F} \times \boldsymbol{\nabla}\sigma$ represents mechanical PV forcing and the last term comes from pressure-dependent effects in the equation of state (referred to as the thermobaric term). Using this representation of the $\mathbf{J}$ vector, one can evaluate individually these contributions to the PV flux.

The vertical component of the PV flux at the sea surface (we refer to J_z), the focus of this study, is obtained by dotting the $\mathbf{J}$ vector (Eq. 3.4) with vertical unit vector ($\mathbf{k}$). Because the vertical velocity at the sea surface can be thought of as zero, the advective flux does not contribute to J_z. Thus, we obtain,

$$J_z = \mathbf{J} \cdot \mathbf{k} = \omega_z \frac{D\sigma}{Dt}\bigg|_{z=0} + (\mathbf{F} \times \boldsymbol{\nabla}\sigma)_z|_{z=0} + \left(\frac{\Phi}{\rho_0}\boldsymbol{\nabla}\rho \times \boldsymbol{\nabla}\sigma\right)_z\bigg|_{z=0}. \tag{3.5}$$

The PV flux J_z is defined such that as upward flux is positive (i.e., negative PV flux indicates ocean PV gain). It is known that the thermobaric term (third term of the RHS of Eq. 3.4) does not make a large contribution especially near the sea surface (Marshall et al. 2001; Deremble et al. 2014). Since we focus on the spatiotemporal scale of lower Rossby number, the relative vorticity is assumed to be smaller than the planetary vorticity in Eq. 3.2. Eq. 3.5 is rewritten as

$$J_z \sim f\frac{D\sigma}{Dt}\bigg|_{z=0} + (\mathbf{F} \times \boldsymbol{\nabla}\sigma)_z|_{z=0}. \tag{3.6}$$

In this way, sea surface PV flux is approximately represented by diabatic and mechanical contribution. As mentioned above, some scaling laws have been proposed to estimate the PV flux represented by Eq. 3.6 from the observational dataset (Czaja & Hausmann 2009; Olsina et al.

2013). However, it has been pointed out that these bulk estimates of sea surface PV flux have ocean PV gain bias mainly due to overestimated summertime heating (Deremble et al. 2014). In the next subsection, some changes in the proposed methods based on observational insights are made to decrease the bias.

3.2.1 Diabatic contribution to PV flux

For convenience, the potential density at the sea surface ($\sigma_{z=0}$) is approximated by that at surface mixed layer (σ_h), following Czaja & Hausmann (2009),

$$\sigma_{z=0} \sim \sigma_h. \tag{3.7}$$

Thus, Diabatic contribution to the sea surface PV flux is represented by the Lagrangian time rate of change in mixed layer potential density multiplied by the Coriolis parameter,

$$f \frac{D\sigma}{Dt}\bigg|_{z=0} \sim f \frac{D\sigma_h}{Dt}. \tag{3.8}$$

In Czaja and Hausmann (2009), they assumed that this mixed layer density change results from the air-sea buoyancy exchange (J_z^{Bs}) and the vertical entrainment at the base of the mixed layer (J_z^E), as with an approach of the bulk mixed layer model. Their estimation of the diabatic contribution is,

$$f \frac{D\sigma_h}{Dt} = J_z^{BS} + J_z^E$$

where

$$J_z^{Bs} = \frac{f}{h}\left(-\frac{\alpha Q_{net}}{C_p} + \beta(E - P)S\rho_0\right), \tag{3.9}$$

and

$$J_z^E = w_{ent}\Delta\sigma_{ent}.$$

In Eq. 3.8, h indicates mixed layer depth, α and β are thermal expansion and haline contraction coefficients of seawater, respectively, Q_{net} is net sea surface heat flux, $E - P$ is net sea surface freshwater flux (evaporation minus precipitation), S is mixed layer salinity,

$$w_{ent} = \begin{cases} 0 \text{ when } \frac{\partial h}{\partial t} \leq 0 \\ \frac{\partial h}{\partial t} \text{ when } \frac{\partial h}{\partial t} > 0 \end{cases} \tag{3.10}$$

is approximate entrainment velocity at the base of the mixed layer, and $\Delta\sigma_{ent}$ ($= 0.5$ kg m^{-3}) is density difference between the mixed layer and the below.

In order to reduce the PV gain bias due to overestimation of summertime heating, we here

perform two alternatives for above-mentioned scaling laws. The first is the subtracting penetrating shortwave radiation at the base of the summertime thin mixed layer (q_h) from the net heat flux, which does not contribute to heating the mixed layer itself. The diabatic contribution from sea surface buoyancy forcing is replaced by

$$J_z^{Bh} = \frac{f}{h}\left(-\frac{\alpha(Q_{net} - q_h)}{C_p} + \beta(E - P)S\rho_0\right). \tag{3.11}$$

The second modification is about the contribution from wind-driven mixing during the warming season. According to the formalism of Eq. 3.9, PV extraction due to mixing in the upper-ocean can occur only when the mixed layer depth becomes deep, that is, during the surface cooling season. However, recent observational studies showed that a significant fraction of heat is carried below the mixed layer due to vertical mixing even during the warming season (Hosoda et al. 2015; Lee et al. 2015). Moreover, the result of Chapter 2 also indicates the occurrence of strong vertical mixing in the upper ocean in the warming season. This suggests that the previous scaling underestimates the PV loss caused by vertical mixing during the warming season, consequently, resulting in ocean PV gain bias. To consider the PV loss due to vertical mixing during warming season, we use a PV flux scaling based on the rate of deepening of the mixed layer caused by wind mixing, proposed by Deremble and Dewar (2012). The PV flux due to diabatic wind mixing effects is written as,

$$J_z^W = \lambda\frac{f\rho u_*^3}{gh^2}, \tag{3.12}$$

where g is gravitational acceleration, u_* is sea surface frictional velocity, and λ is a constant parameter. This scaling is also based on the concept of bulk mixed layer model and models the vertical entrainment at the base of the mixed layer even when the mixed layer appears to be shallow. This contribution is always positive since the wind can only mix the upper ocean, i.e., PV extraction from the ocean.

For the calculation of diabatic contribution to the sea surface PV flux, Monthly net surface heat flux (the sum of shortwave and longwave radiation flux and sensible and latent heat flux) and freshwater flux, and daily sea surface wind stress from ERA-interim (Dee et al. 2011) are used. We also use the Roemmich–Gilson Argo climatology (RG Argo; Roemmich and Gilson 2009) to obtain the oceanic variables (mixed layer depth, density, and salinity). The mixed layer depth is defined as the shallowest depth at which either the potential density increases from the surface value by 0.125 kg m^{-3} or temperature differs from the surface by 0.5 °C. To estimate the penetrating shortwave radiation at the base of mixed layer q_h, we use a generalized empirical

model (Eq. 2.8 and 2.9: Lee et al. 2005) with satellite ocean color data observed by Moderate Resolution Imaging Spectroradiometer (MODIS Aqua). Due to data availability, we calculate the PV flux from 2004 to 2017 and refer to the average over the entire period as the climatology.

Annual mean and monthly climatology of diabatic buoyancy contribution to sea surface PV flux are shown in Fig. 3.1. Since the buoyancy component is mainly driven by the seasonal cycle of the net surface heat flux, it shows oceanic PV gain in summer and the oceanic PV loss in winter. As the annual mean, buoyancy component contributes to the net PV gain because of summertime thinner mixed layer, even in the regions of the net annual mean buoyancy loss except for the regions of western boundary current. Changes due to considering of penetrating shortwave radiation are notably shown in mid-latitude summer where the mean shortwave radiation flux is large and the f also remains large. The differences reach up to 40% of annual mean value.

In Figure. 3.2, we show annual mean and monthly climatology of diabatic contribution due to wind mixing (J_z^W) and vertical entrainment (J_z^E). Directly estimating the entrainment effect from the daily wind product, J_z^W indicates PV oceanic loss by mixing even during the warming season. On the other hand, J_z^W contribution becomes smaller than that of J_z^E in the cooling season when the mixed layer is relatively deep. Consequently, PV extraction is enhanced as the annual mean especially in the subpolar North Pacific and the western North Atlantic.

3.3.2 Mechanical contribution to PV flux

To quantify the mechanical contribution to the PV flux (second term of the RHS in of Eq. 3.6), we use a scaling that has been frequently used in previous studies (e.g. Maze & Marshall 2011). The nonconservative frictional force in mechanical term is written as,

$$\mathbf{F} = \frac{1}{\rho_0} \frac{\partial \boldsymbol{\tau}}{\partial z},$$
(3.13)

where $\boldsymbol{\tau}$ indicates turbulent stress representing the vertical transport of momentum. Assuming the thickness of a layer that significantly experiences the turbulent stress given at the sea surface as the mixed layer depth, the vertical divergence of the stress is approximated as,

$$\mathbf{F} \sim \frac{\boldsymbol{\tau}_s}{\rho_0 h},$$

using the turbulent surface stress at the sea surface ($\boldsymbol{\tau}_s$; i.e., surface wind stress). Substituting the mixed layer density for the sea surface as with the scaling for the diabatic contribution, the mechanical contribution to the sea surface PV flux is estimated as,

$$J_z^F = (\mathbf{F} \times \boldsymbol{\nabla}\sigma)_z|_{z=0} \sim \left(\frac{\boldsymbol{\tau}_s}{\rho_0 h} \times \boldsymbol{\nabla}\sigma_h\right)_z. \tag{3.14}$$

This mechanical contribution to the sea surface PV flux is, therefore, simply related to density advection by the Ekman transport. Annual mean and monthly climatology of the mechanical contribution calculated from daily wind stress of ERA-interim are shown in Fig. 3.3. Net annual mean PV gain (loss) occur in the region where the easterly (westerly) wind is dominant. It is because that generally the easterly (westerly) wind carries relatively warmer (cooler) water from the south (north) to north (south) and thus causes the creation (destruction) of stratification.

3.3.3 Net surface PV flux and its validation

For comparison, we show the 2004–2017 mean net sea surface PV flux calculated using different combinations of scaling for diabatic and mechanical contributions in Fig. 3.4. Four patterns of the net sea surface PV flux are estimated; Fig. 3.4a is an estimate that above-mentioned two alternatives are performed ($J_z^{Bh} + J_z^W + J_z^F$), Fig. 3.4b is an estimate by previous methodology ($J_z^{Bs} + J_z^E + J_z^F$), and Fig. 3.4c ang 3.4d are estimates that one of the two alternatives are not performed ($J_z^{Bs} + J_z^W + J_z^F$ and $J_z^{Bh} + J_z^E + J_z^F$). Comparing this study's estimate (Fig. 3.4a) with the previous one (Fig. 3.4b), it is confirmed that the regions of the net PV loss increase due to the correction for the reduction in oceanic PV gain bias. As shown in Fig. 3.1 and 3.2, effects by considering the penetrating shortwave radiation can be seen in mid-latitude of both the Pacific and Atlantic (Fig. 3.4a and c), and those due to change in scaling for mixing can be clearly seen in high latitude (Fig. 3.4a and d).

In this subsection, we investigate which estimated flux is valid using a constraint from the impermeability theorem of PV. According to the impermeability theorem, time rate of change in an integrated PV in an isopycnal layer should coincide with the sea surface PV flux through the outcrop window of the isopycnal, with neglecting the PV creation by friction and PV flux at the boundaries. We independently compute the time rate of change in the total amount of PV in an isopycnal layer from RG Argo and compare it to estimated PV fluxes.

The integrated PV in an isopycnal layer σ (refer to Q^σ) is well approximated by the vertical component of the Ertel's PV (E.q. 3.1) integrated over the layer (Valis 2006; Deremble et al. 2014),

$$Q^\sigma = \int_x \int_y \int_z (f + \mathbf{k} \cdot \boldsymbol{\nabla} \times \mathbf{u})\frac{\partial\sigma}{\partial z} dx\, dy\, dz, \tag{3.15}$$

where the three integral intervals are set to cover the entire isopycnal layer. Under the same

assumption of low Rossby number as Eq. 3.6, the relative vorticity is negligible. Thus, Eq. 3.15 is rewritten by performing vertical integration as

$$Q^{\sigma} \sim \Delta\sigma \int_x \int_y f \, dx \, dy, \tag{3.16}$$

where $\Delta\sigma$ (=0.4 kg m^{-3}) is a density difference between the upper and lower limit of the chosen isopycnal layer. We compute this integrated PV from monthly density field of RG Argo. On the other hand, the amount of PV that enter into or exit from the same isopycnal layer σ (refer to J_z^{σ}) is calculated by area integration of the sea surface PV flux over the outcrop window,

$$J_z^{\sigma} = \int_{\sigma-\Delta\sigma/2}^{\sigma+\Delta\sigma/2} -J_z \, dx \, dy. \tag{3.17}$$

In Fig. 3.5, we show the comparisons between estimated PV fluxes and Integrated PV for representative isopycnals in the North Pacific and North Atlantic. In all isopycnal layers, the integrated PV increases (i.e., the isopycnal layer geographically expands) in summer due to oceanic PV gain, conversely, decrease in winter by surface PV loss. By performing the alternatives of estimation method of the flux in this study, the summertime PV gain bias is reduced. Moreover, the improved flux becomes more consistent with the variation in PV of the ocean interior than the others. To evaluate these fluxes for all isopycnals over the entire analytical period (2004–2017), we compute the correlation coefficients and root-mean-square (RMS) differences between the sea surface PV fluxes and the time rate of change in the integrated PV (Fig. 3.6). Although the change in the correlation coefficient is small, the RMS differences are reduced in most of the isopycnals except for the denser isopycnals (σ>25.8 kg m^{-3}) in the North Pacific. It should be noted that these two time series do not completely match even if the flux could be obtained without an estimation error. Indeed, the RMS differences between improved PV flux and change in integrated PV (black lines in Fig. 3.6c, d) also include contribution from the horizontal PV flux, PV production by friction and the component of relative vorticity, other than the estimation errors.

3.3 Climatology of sea surface PV flux

Using the improved estimate of the sea surface PV flux, we investigate the climatological feature and related variables such as annual subduction rate, which can be obtained from the PV flux.

3.3.1 Isopycnal view

Annual cycle of the net surface PV flux and its three components averaged along isopycnal

outcrops are shown in Fig. 3.7. Note that each flux is normalized by the density interval $\Delta\sigma$ (=0.4 kg m^{-3}), and thus the unit is m^2 s^{-2}. The diabatic contribution shows significant seasonal changes and, especially, its buoyancy component makes seasonality of the net surface PV flux (Fig. 3.7c, d). The diabatic contribution due to wind mixing (Fig. 3.7e, f) reaches the peak in summer in most of the isopycnals in both North Pacific and North Atlantic but has two peaks in isopycnals that are denser than 25 kg m^{-3}. Although the mechanical contribution is relatively small, it also shows seasonal changes mainly due to the seasonality of zonal wind.

In the annual mean field (Fig. 3.8), net surface PV gain (loss) occurs in lighter (denser) density regions in both the North Pacific and North Atlantic, as has been thought traditionally. The compositions of the net air-sea PV exchange, however, are significantly different. The mechanical component in the North Atlantic contributes to the mean field in low latitude region, but it is not important and the diabatic contribution are dominant in the high latitude region (Fig. 3.8b). On the other hand, in the North Pacific, the mechanical component significantly contributes in the entire basin.

In each basin, the PV loss show some peaks that correspond to density ranges of major water masses: in the North Pacific, the peaks at ~25.0 kg m^{-3} and ~26.0 kg m^{-3} correspond to Subtropical Mode Water (STMW) and Central Mode Water (CMW), respectively (e.g. Oka & Qiu 2012), and in the North Atlantic, the peak at ~26.4 kg m^{-3} corresponds to Eighteen Degree Water (EDW; e.g., Maze et al. 2009). This is consistent with the fact that each water mass is formed by atmospheric PV extraction and observed as low PV signals of the ocean interior. Moreover, the special distribution of the PV loss through the outcrop of these isopycnals (Fig 3.9; 25.4 kg m^{-3} and 26.4 kg m^{-3}) roughly correspond to the formation regions of respective mode water, as mentioned by previous studies (e.g., Maze et al. 2009; Oka & Qiu 2012).

3.3.2 Eulerian view and subduction rate

Assuming the steady state of the main thermocline, Eulerian-averaged annual mean surface PV flux is associated with annual subduction rate S_{ann}, as follow (see Marshall et al. 2001),

$$S_{ann} = -\frac{[J_z dA]^{\text{surface}}}{[\rho Q dA]^{\text{thermocline}}}, \tag{3.18}$$

We show the Eulerian annual subduction rate calculated with use of the improved surface PV flux in Fig. 3.11. Following Marshall et al. (2001), we assign maximum PV in March computed from RG Argo (Fig. 3.10) to the main thermocline value in Eq. 3.18. The Eulerian annual subduction rate shows consistent features as a whole with that computed from Lagrangian methodology,

which commonly has been used in previous studies (e.g., Qiu & Huang 1995; Suga et al. 2008). There are, however, also some differences. For example, significant subduction that corresponds to the North Pacific eastern STMW (ESTMW; roughly located around 20°N, 140°W) is not shown in this Eulerian estimate. As a result, area integrated subduction rate (Fig. 3.11b) in the STMW density range is smaller than those from the Lagrangian estimates (~6 Sv at 25.0–25.2 kg m^{-3}; Suga et al. 2008). Also near the boundary regions, there are inconsistencies to previous estimates probably due to lack of consideration of the horizontal and coastal processes, such as friction by the western boundary currents, coastal upwelling, and tidal mixing. Although these differences come from the limitation of this study's method, there are possibilities that these reflect the dynamical difference in the subduction processes. Further investigations are needed to understand this Eulerian subduction rate.

3.4 Interannual variability in sea surface PV flux

Fig 3.8 suggests significant interannual variability of the net surface PV flux, although the climatological feature does not change drastically. In this section, we investigate the spatiotemporal characteristic of the net surface PV flux. We also discuss the summertime preconditioning of the winter mixed layer development, using the surface PV flux framework.

3.4.1 Spatiotemporal characteristics of interannual variability

We show the spatial distribution of the interannual standard deviation of the net surface PV flux anomaly in Fig. 3.12. The amplitude of the interannual variability in annual mean net PV flux anomaly is large along the western boundary current in both the North Pacific and the North Atlantic. Including the other regions, the interannual variabilities exceed 20% of the climatological mean values. Calculating the standard deviation for the season of PV gain (April–August) and PV loss (September–March) separately (c.f., Fig 3.7), these standard deviations show different spatial distribution (Fig. 3.12b, c). While the variabilities of winter mean anomalies are confined near the regions of western boundary current and its extension, those of summertime mean anomalies relatively extend to the broader region. Interannual variability from buoyancy component is dominant, followed by those from wind mixing component, and mechanical contribution has little variability (Fig. 3.12d–f).

To identify the dominant spatiotemporal pattern of variability in entire the North Pacific and North Atlantic, we performed the empirical orthogonal function (EOF) analysis to the 2004–2017 net surface PV flux anomaly. Although attention should be paid because of the short time series,

a decadal variability is detected as the first EOF mode explaining 21% of the total variance (Fig. 3.13). The first mode shows the same phase variability of the western part of the North Pacific and North Atlantic. In the North Pacific, the spatial pattern seems to be the Pacific Decadal Oscillation (PDO; Mantua et al. 1997) pattern, which has opposite signs between its western and eastern part. The correlation coefficient between the time coefficients of the first mode and the PDO index is 0.57.

3.4.2 Discussion of summertime preconditioning of mixed layer development

In regions where the surface mixed layer well develops during the winter in the North Pacific, water masses, called Mode Water, are formed since the developed winter mixed layer is isolated from atmospheric forcing due to spring surface heating (Fig. 3.14). The Mode Water plays an important role in ocean ventilation processes, which result in uptake of heat, carbon, and oxygen. The volume of the formation of the Mode Water is regulated by the development of the winter mixed layer.

Many previous studies on the development of winter mixed layer have been done and have revealed that some factors (winter cooling and background stratification etc.) are important for the development (e.g., Suga & Hanawa 1995; Qiu & Chen 2006). The winter mixed layer develops as destroying upper-ocean stratification presented in pre-winter by surface cooling and wind mixing (c.f., Fig1.1). In addition to the intensity of the winter cooling, therefore, summertime preconditioning (i.e., the strength of stratification existing when the winter cooling begins) is also important for determining how deep the winter mixed layer develops. The impact of summertime preconditioning on the development of winter mixed layer has been examined from studies focused on the interannual variability of the winter mixed layer depth in regions of Mode Water formation: in STMW formation region, the impact reported as a case study (Kako & Kubota 2007), and in the eastern part of CMW and ESTMW, the impact has been recognized in the interannual variability of the winter mixed layer (Yamaguchi 2016; Toyoda et al. 2011). The impact, however, is geographically limited in the formation region of Mode Water. In this section, we attempt to discuss the reason why the impact of summertime preconditioning appears in limited regions, using the net surface PV flux.

In focus on the large scale (i.e., situation satisfying the low Rossby number), PV defined by Eq. 3.1 is well approximated as the vertical density stratification multiplied by Coriolis parameter,

$$Q = -\frac{1}{\rho}\boldsymbol{\omega} \cdot \boldsymbol{\nabla}\sigma = -\frac{1}{\rho}(2\boldsymbol{\Omega} + \boldsymbol{\nabla} \times \mathbf{u}) \cdot \boldsymbol{\nabla}\sigma \sim -\frac{f}{\rho}\frac{\partial\sigma}{\partial z}. \tag{3.19}$$

This expression of PV framework enables us to uniformly treat the development of summertime upper-ocean stratification and winter mixed layer as oceanic PV gain and loss respectively, which have been represented commonly by different metrics. Moreover, the mechanical and diabatic forcing, resulting in the development of summertime stratification and winter mixed later, are elegantly put together within a single representation of the net surface PV flux (see Section 3.2).

To compare the interannual variability in summertime forcing (PV input) and wintertime forcing (PV extraction), we show the differences in the standard deviation of them and the differences divided by the annual mean surface PV flux in Fig. 3.15. Figure 3.15 indicates that the interannual variability in summertime PV forcing is larger than that of winter and the differences are significantly large with respect to the annual mean values, in the formation region of the ESTMW and the eastern part of CMW formation region. This means that the interannual variability in summertime forcing can significantly contribute to the annual mean surface PV flux that could be a driver of the interannual variability in the winter mixed layer depth. Therefore, previously reported regions where the summertime preconditioning has an impact on the development of winter mixed layer are interpreted as limited regions that summertime forcing potentially tend to be able to be dominant in the annual mean PV flux anomaly.

3.5 Conclusions

In this chapter, we improved previously proposed methods for estimation of the sea surface PV flux from observations. Considering the penetration of shortwave radiation at the base of the mixed layer and vertical mixing during the warming season, the PV gain bias is reduced. Our estimated PV flux showed more consistency with independently calculated PV variation of the ocean interior. Conclusions obtained from newly estimated PV flux are as follows;

- Typically, the net surface PV flux consists of the dominant diabatic contribution and mechanical contribution. The buoyancy component in the diabatic contribution shows seasonal variation mainly due to the seasonality of net surface heat flux and has the same order of magnitude of the wing mixing component.

- In the annual mean field, the PV gain (loss) occurs in low (high) latitude in both the North Pacific and the North Atlantic. The components, however, are different; The mechanical contribution is more important in the North Pacific, and the diabatic contribution is dominant in the high latitude region of the North Atlantic.

- The annual mean PV losses have the peak at the density that corresponds to the density of the major water mass in both the North Pacific and the North Atlantic.

- The net surface PV flux shows significant interannual variability mainly caused by the buoyancy component. In the entire basin of the North Pacific and North Atlantic, PDO like decadal variability is suggested.

We also estimated the Eulerian annual subduction rate from the sea surface PV flux. Although we found some features differed from the previous estimate by Lagrangian methodology, further investigations are needed for understanding the findings.
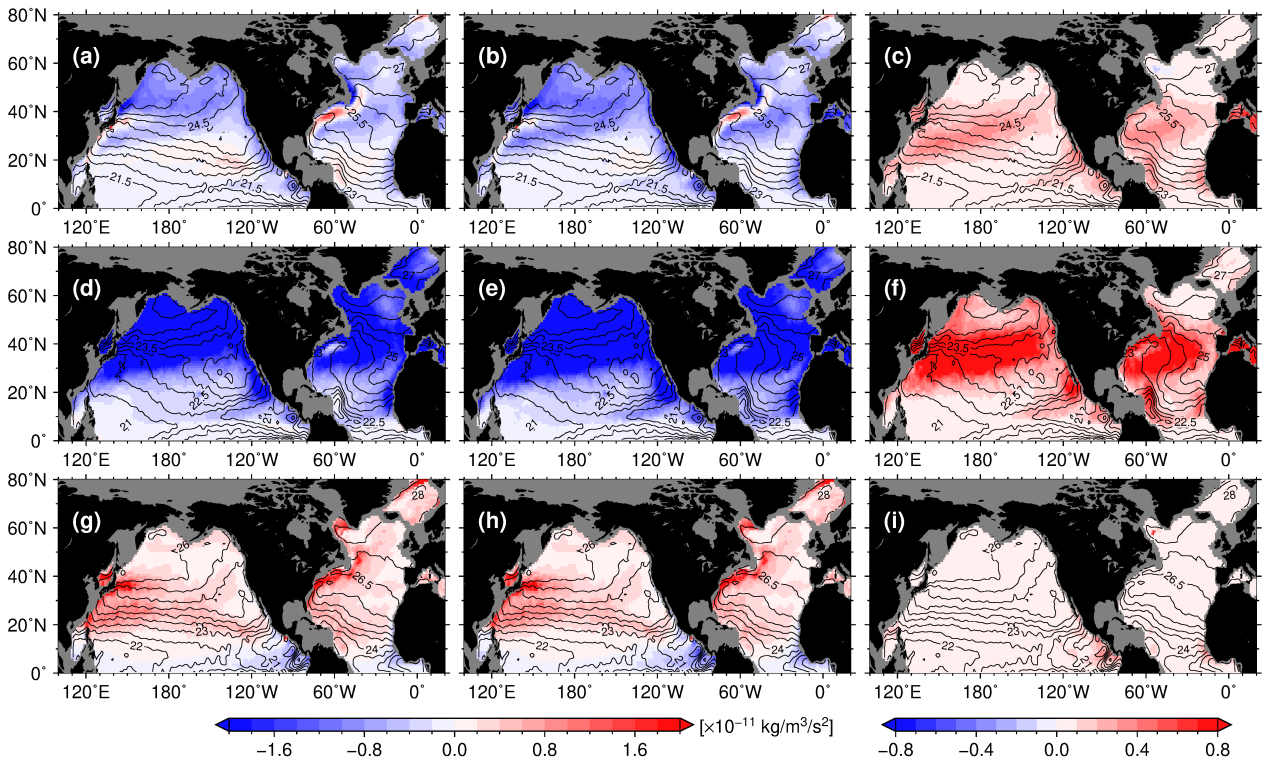
Figure 3.1. (a, b) Annual mean and monthly climatology of (d, e) August and (g, h) February for buoyancy components of the diabatic contribution to sea surface PV flux (J_z^{Bh} and J_z^{Bs}). (a, d, g) J_z^{Bh}, (b, e, h) J_z^{Bs}, and (c, f, i) the difference (i.e, $J_z^{Bh} - J_z^{Bh}$). Climatological sea surface density of each month is superimposed with contour lines (kg m^{-3}).
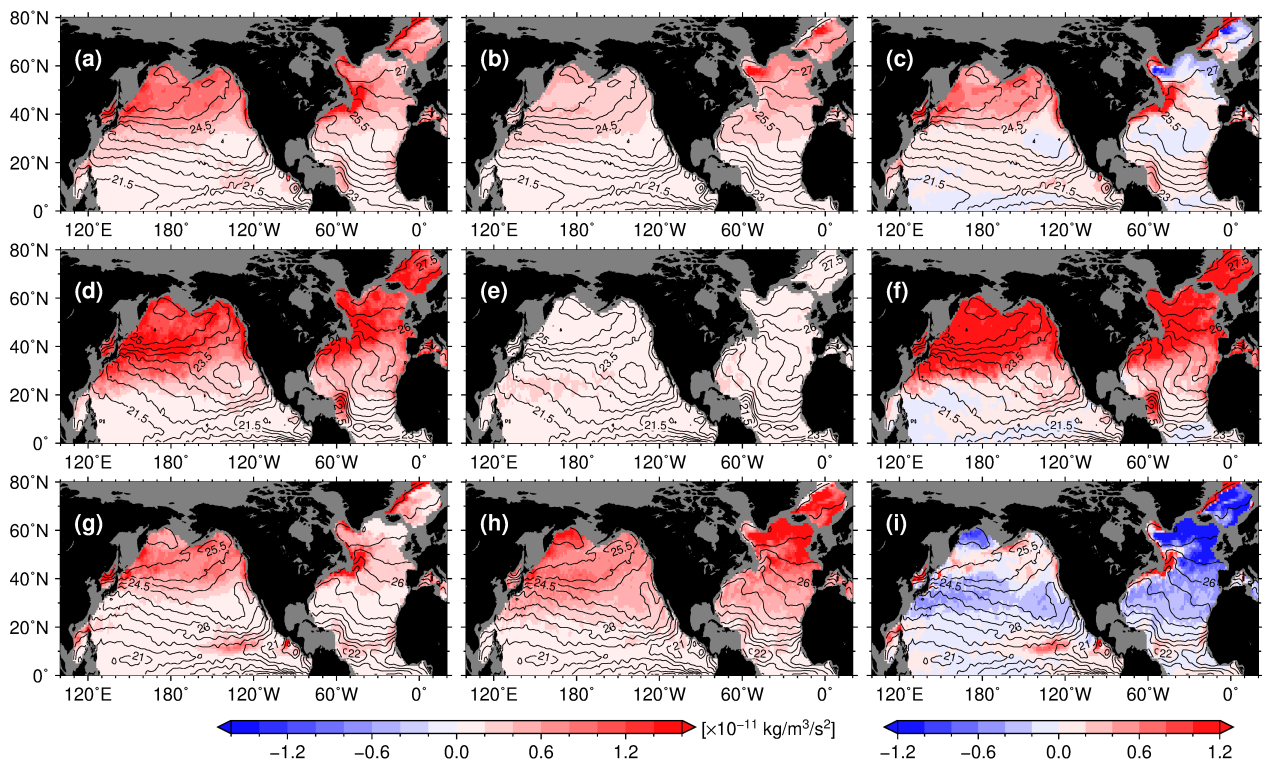
Figure 3.2. (a, b) Annual mean and monthly climatology of (d, e) July and (g, h) November for diabatic contributions due to wind mixing and entrainment to sea surface PV flux (J_z^W and J_z^E). (a, d, g) J_z^W, (b, e, h) J_z^E, and (c, f, i) the difference (i.e, $J_z^W - J_z^E$). Climatological sea surface density of each month is superimposed with contour lines (kg m^{-3}).
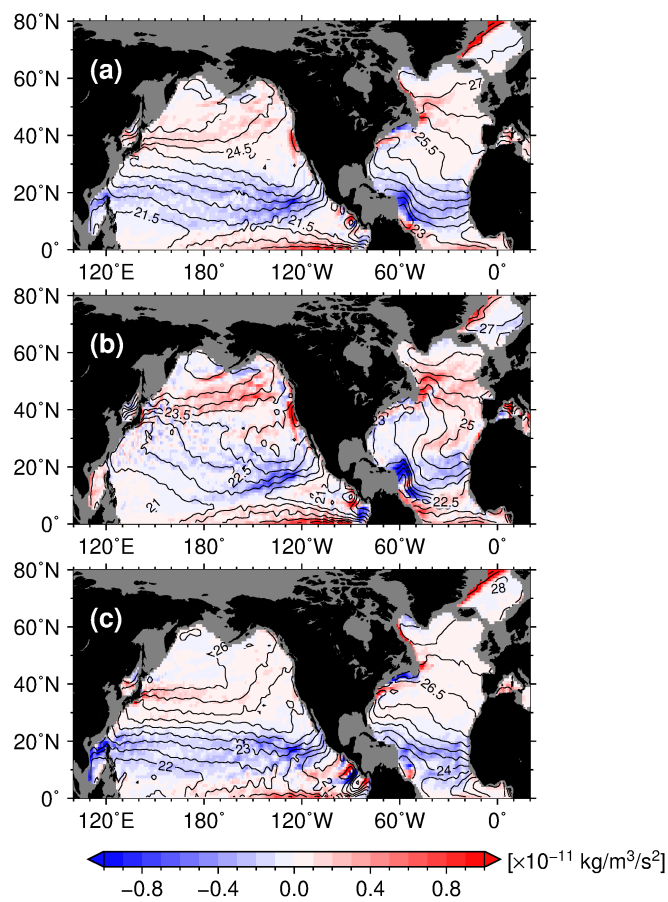
Figure 3.3. (a) Annual mean and (b) August and (c) February climatology of mechanical contribution to sea surface PV flux (J_z^F). Climatological sea surface density of each month is superimposed with contour lines (kg m^{-3}).
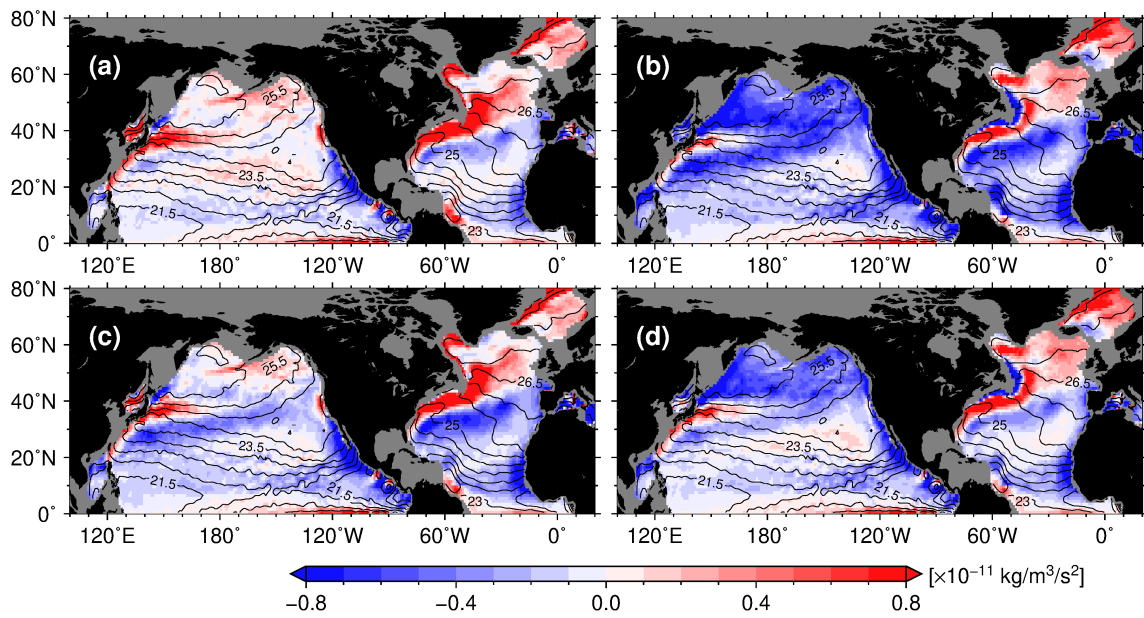
Figure 3.4. Annual mean net surface PV flux averaged from 2004 to 2017. (a) is an estimate that two alternatives are performed ($J_z^{Bh} + J_z^W + J_z^F$), (b) is an estimate by previous methodology ($J_z^{Bs} + J_z^E + J_z^F$), and (c, d) are estimates that one of the two alternatives are not performed ($J_z^{Bs} + J_z^W + J_z^F$ and $J_z^{Bh} + J_z^E + J_z^F$).
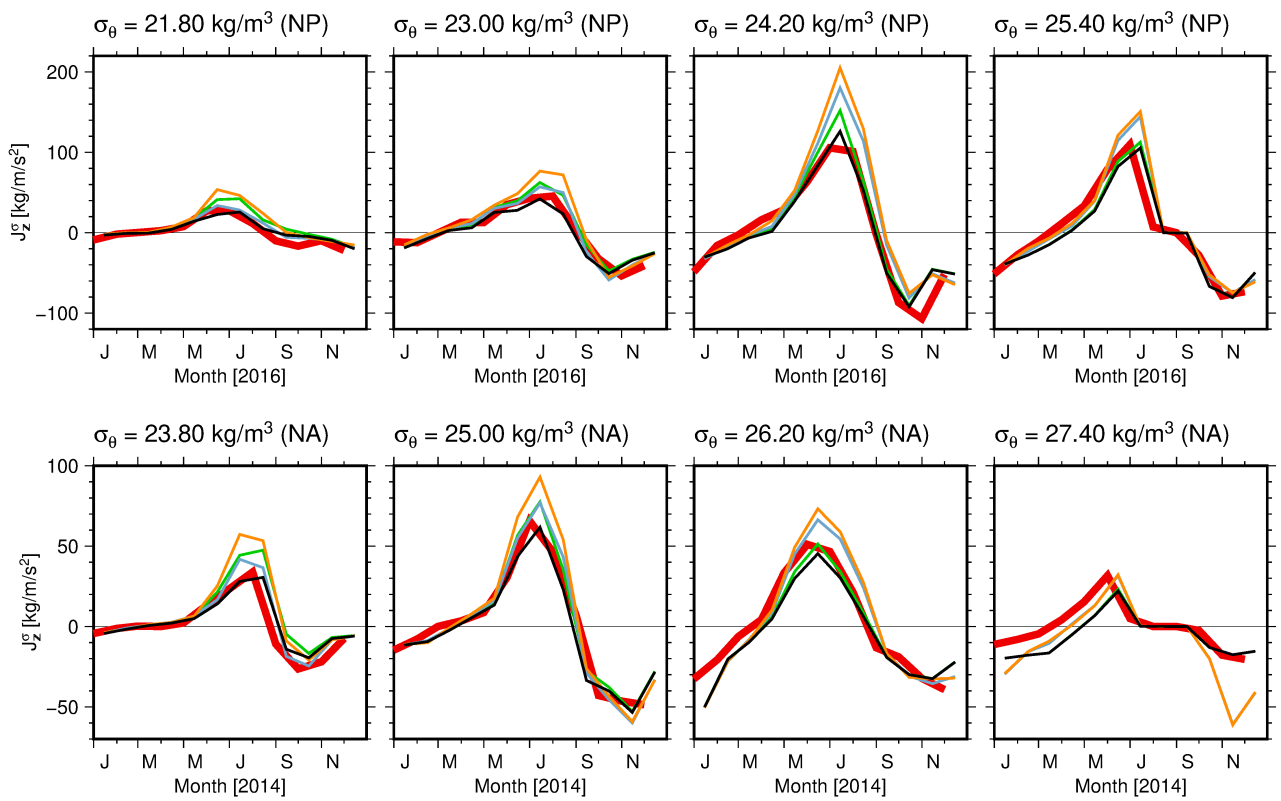
Figure 3.5. Climatological time rate of change in integrated PV in isopycnal layers (red lines) and estimated PV fluxes from the outcrop window for representative isopycnals (upper panels) in the North Pacific and (lower panels) in the North Atlantic. Black, orange, green, and blue lines indicate flux of this study's estimation ($J_z^{Bh} + J_z^W + J_z^F$), previous methodology ($J_z^{Bs} + J_z^E + J_z^F$), and estimation that one of the two alternatives are not performed ($J_z^{Bs} + J_z^W + J_z^F$, and $J_z^{Bh} + J_z^E + J_z^F$), respectively.
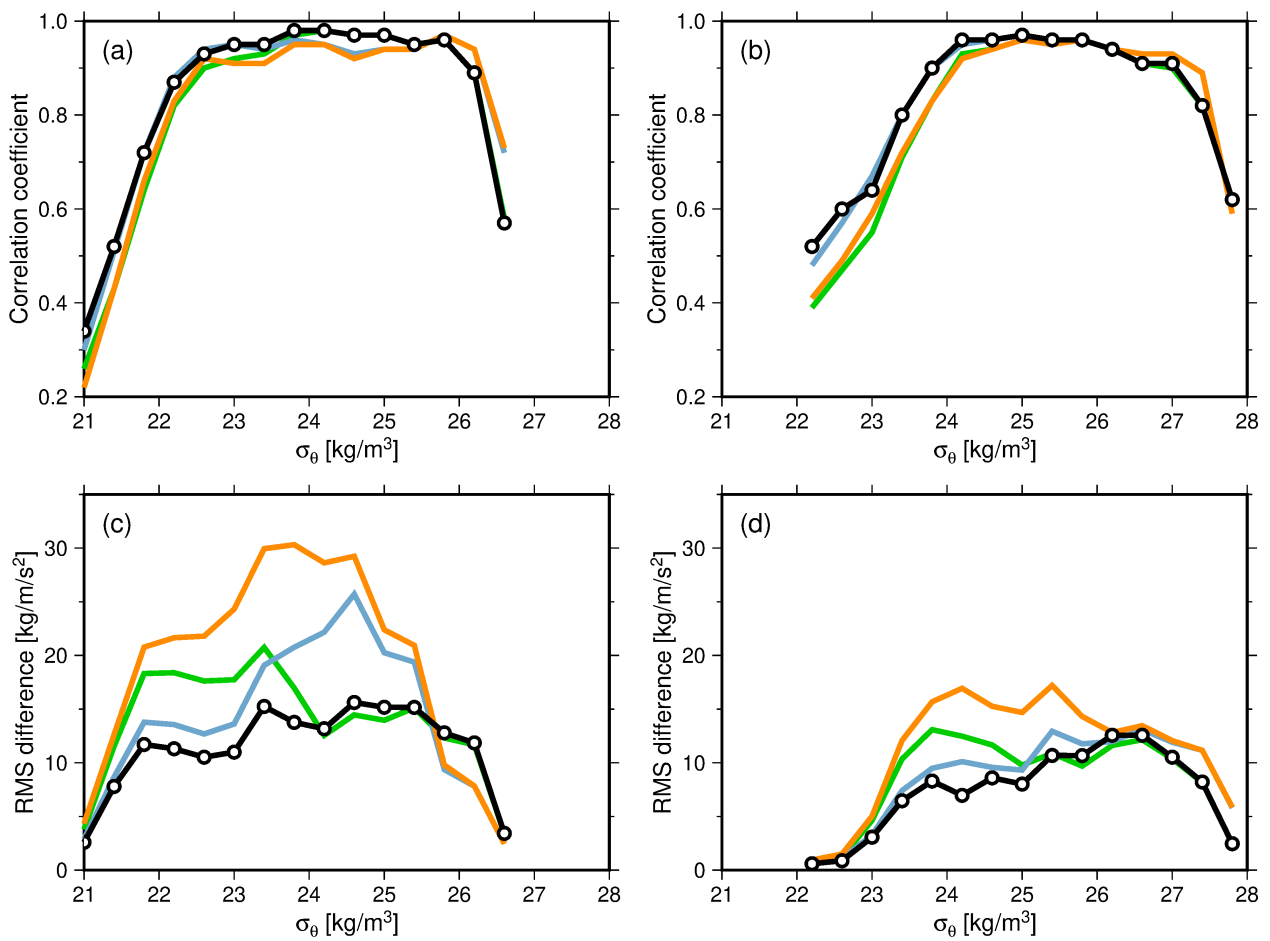
Figure 3.6. (a, b) Correlation coefficients and (c, d) root-mean-square (RMS) differences between estimated PV fluxes (J_z^σ) and the time rate of change in the integrated PV (Q^σ) over isopycnals in (left) the North Pacific and (right) the North Atlantic. Colors are same as Fig. 3.5.
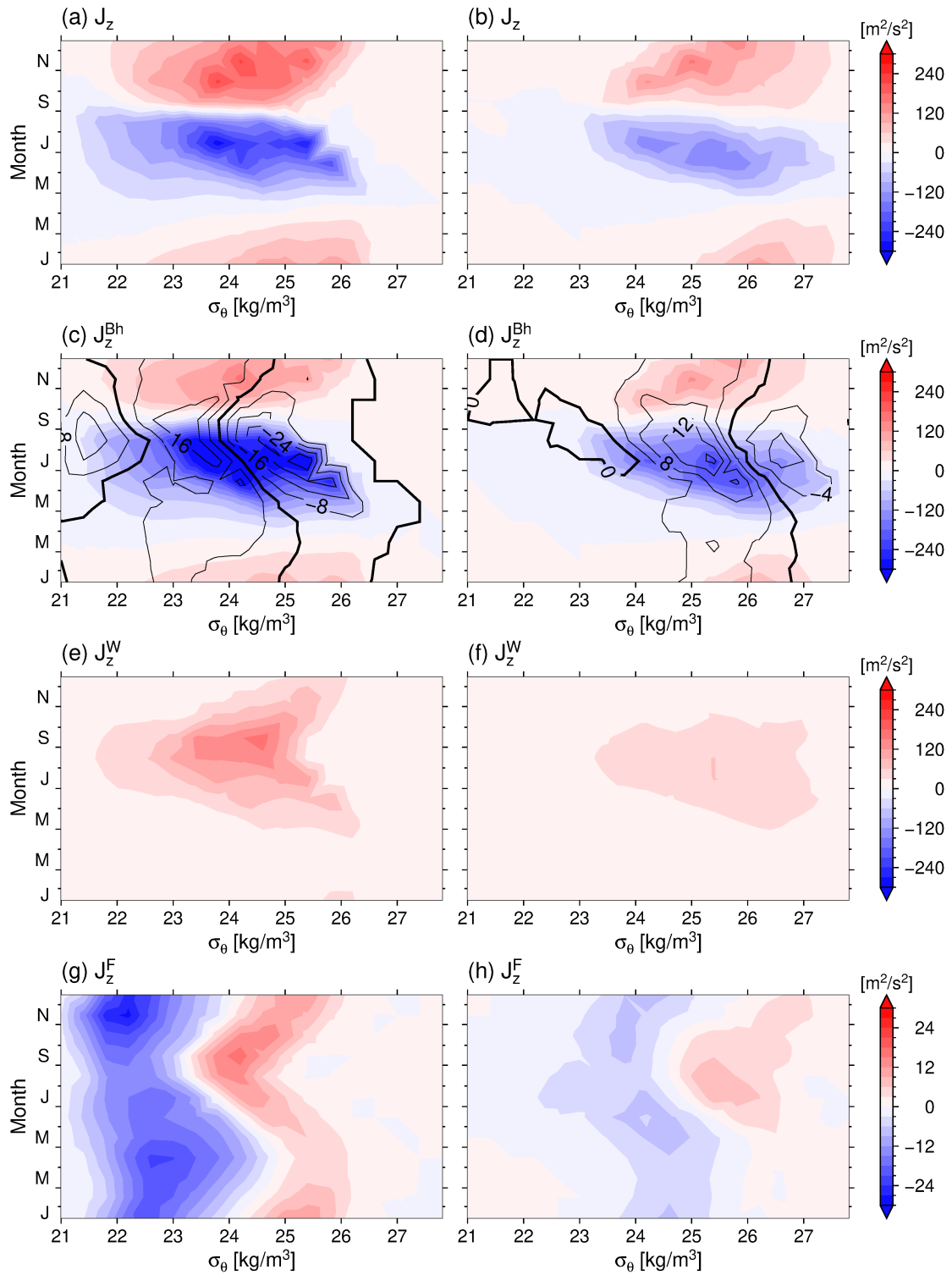
Figure 3.7. Annual cycle of net surface PV flux and its components averaged along isopycnal outcrops. Left (Right) panels are for the North Pacific (North Atlantic). Diabatic contribution due to the buoyancy flux (c, d) is shown separately: colors (contours) indicate heat (freshwater) component.
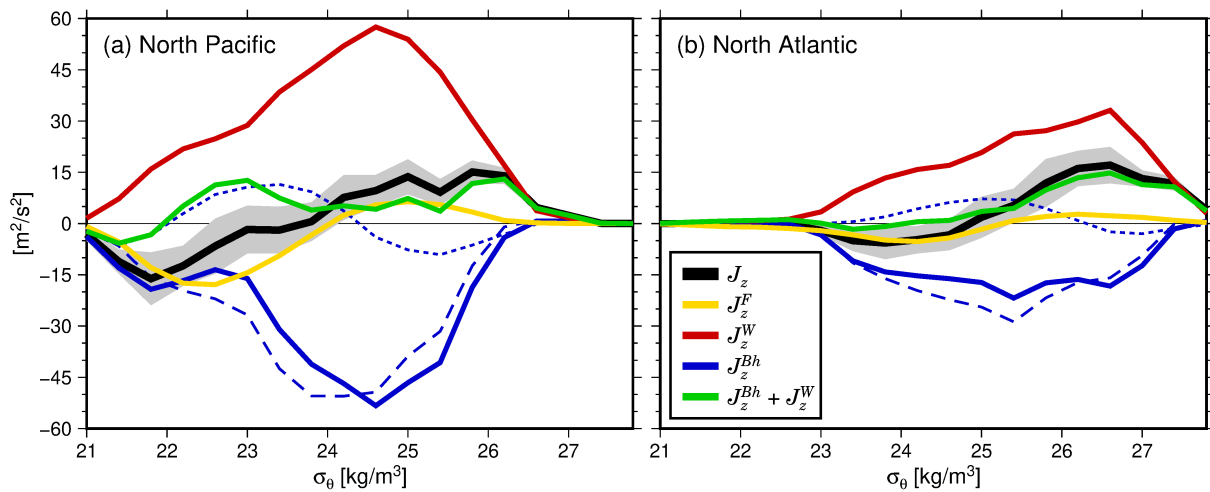
Figure 3.8. Annual mean net surface PV flux and its three components averaged along isopycnal outcrops. Blue dashed (dotted) lines indicate heat (freshwater) component of diabatic contribution from buoyancy flux. Gray shade shows the interannual standard deviation of the net surface PV flux.
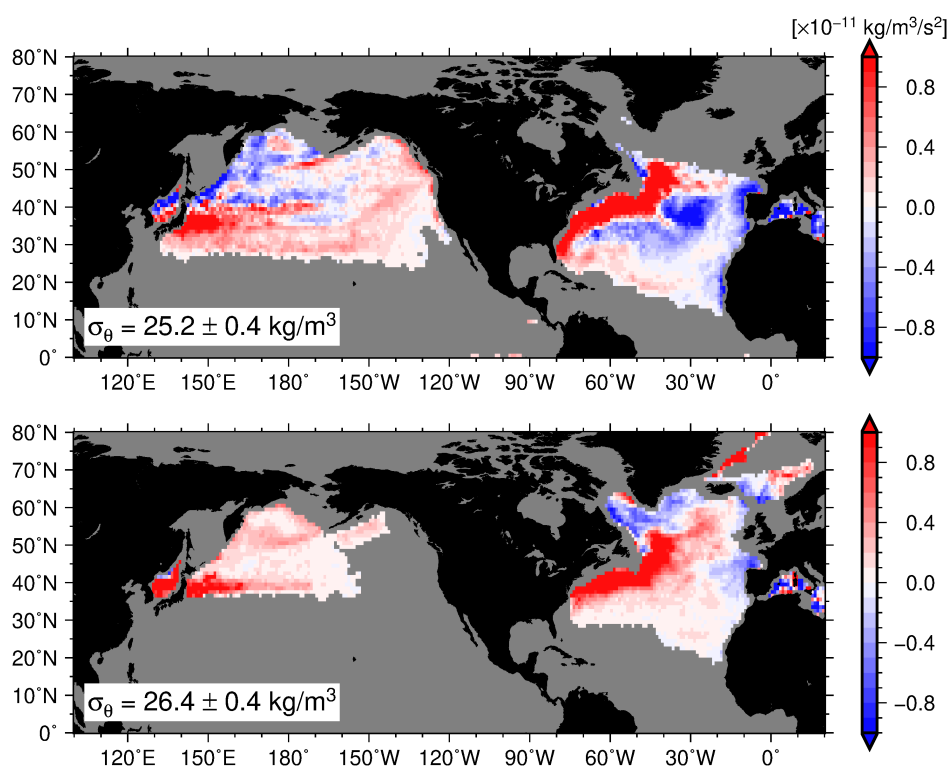
Figure 3.9. Spatial distribution of annual mean net surface PV flux averaged along specific isopycnal outcrop window. The PV flux at given a geographical point is calculated by summing climatological monthly flux over one year if the point is included in the outcrop window, and then the sum is divided by 12 months.
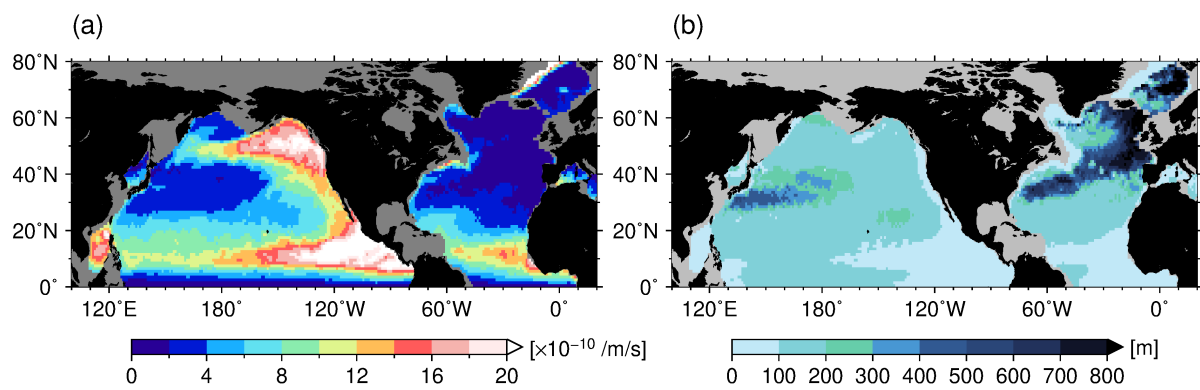
Figure 3.10. Spatial distribution of (a) maximum PV in March and (b) its depth, computed from monthly climatology of RG Argo.
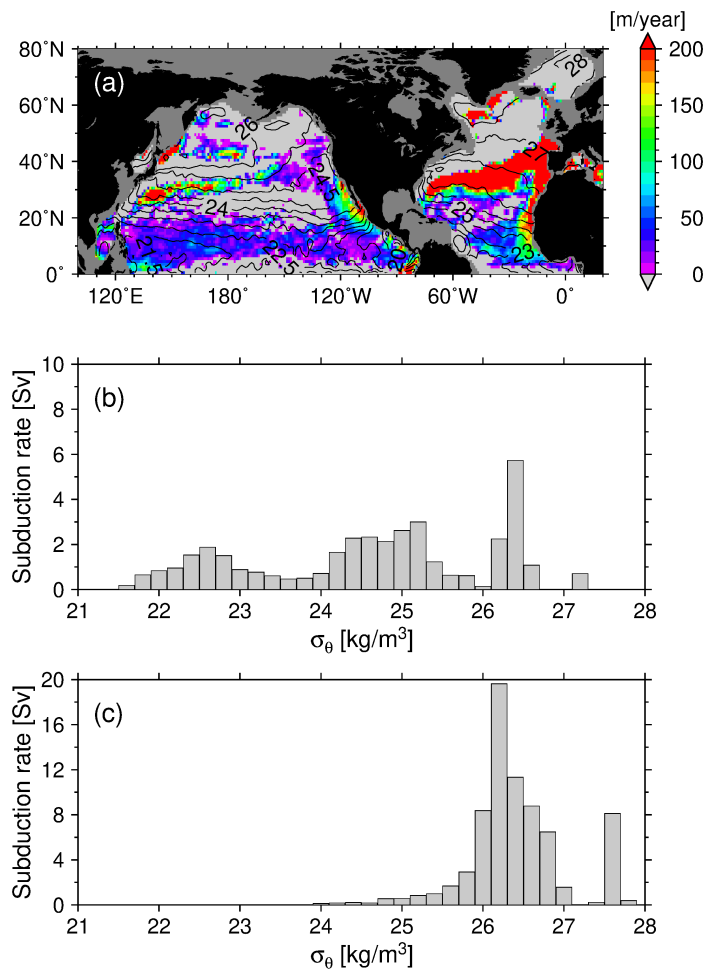
Figure 3.11. (a) Estimated Eulerian annual subduction rate (color) and climatological sea surface density in March. (b, c) Subduction rate integrated in winter outcrop area for (b) the North Pacific and (c) the North Atlantic.
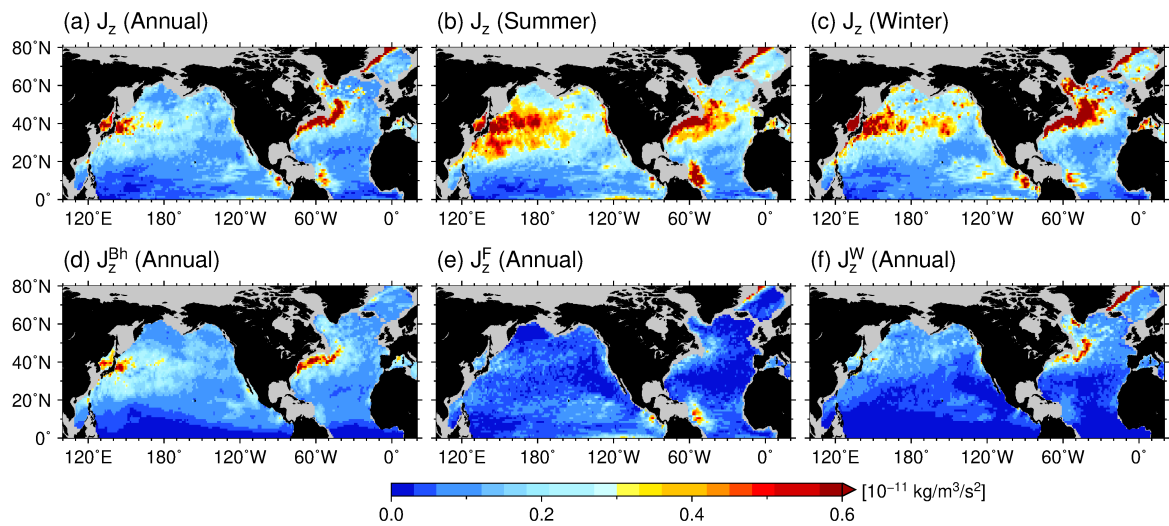
Figure 3.12. Interannual standard deviations of (a) annual, (b) summertime (April–August), and (c) wintertime (September–March) mean net surface PV flux anomalies and (d–f) those for three components of the net surface PV flux.
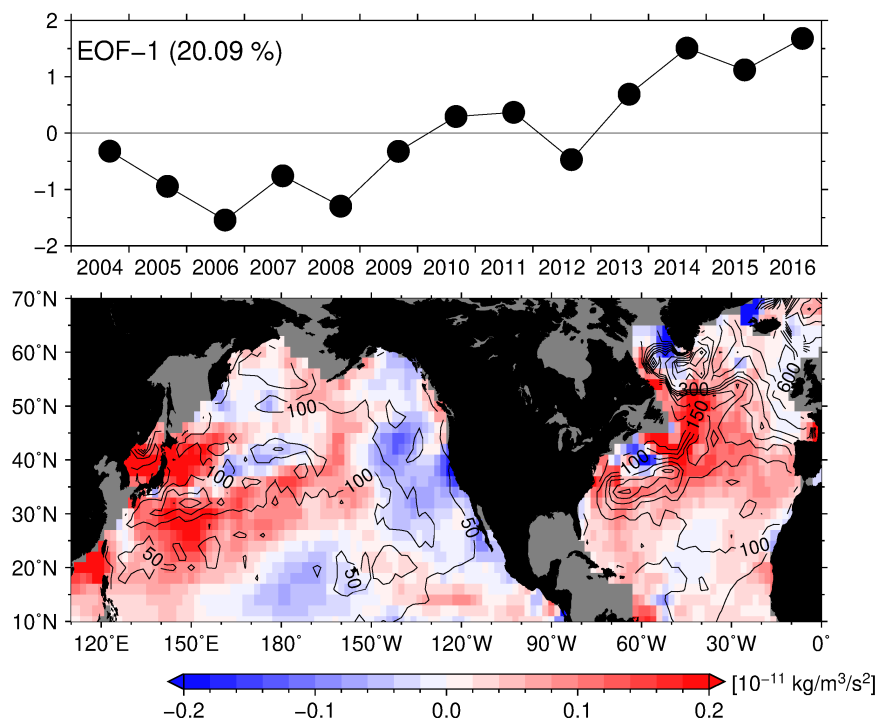
Figure 3.13. (upper) Normalize time coefficients of the first EOF mode of annual mean surface PV flux anomaly and (lower) the regression coefficients. Black contours indicate climatological mixed layer depth in March.
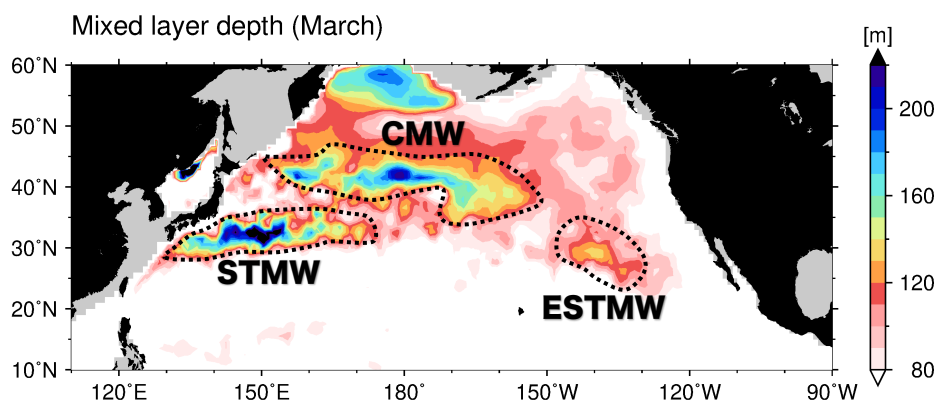
Figure 3.14. Formation regions of the Mode Water (Subtropical Mode Water (STMW), Central Mode Water (CMW), and Eastern Subtropical Mode Water (ESTMW)) superimposed on a map of climatological winter mixed layer depth from RG Argo.
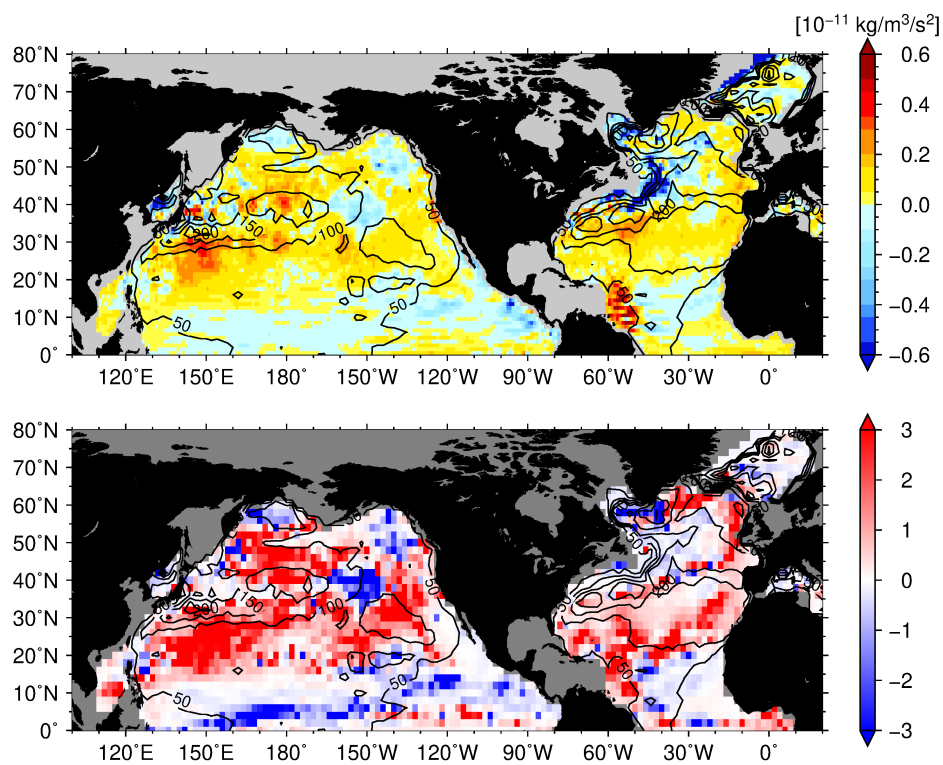
Figure 3.15. (upper) Differences in the interannual standard deviations of summer and winter mean net surface PV flux anomaly (i.e., Fig. 3.12b minus 3.12c). (lower) The difference divided by the annual mean net surface PV flux. Figures are superimposed on a map of climatological winter mixed layer depth from RG Argo.

Chapter 4
Observed long-term trend and variability in global upper-ocean stratification

4.1 Introduction

Upper-ocean stratification plays an important role in the climate system and in many oceanic biogeochemical processes. The strength of near-surface density stratification controls the intensity of vertical mixing (e.g., Cronin et al., 2013; Qiu et al., 2004), which in turn affects the development of the surface mixed layer (ML) and the entrainment process at the base of the ML. The ML depth directly modulates the oceanic response to atmospheric forcing and the ocean ventilation process that involves the subduction of water masses into the ocean interior, accompanied by heat, carbon, and oxygen. The upper-ocean stratification can also have a direct impact on the biogeochemistry by regulating components of the upper-ocean environment that are crucial for biological productivity, such as light availability for photosynthesis and nutrient supply from the subsurface ocean.

As a consequence of the global warming that has already occurred, global-average upper-ocean thermal stratification has been enhanced due to the surface intensification of the warming signal (Rhein et al., 2013). In addition, many studies on future climate projection using climate models in the Coupled Model Intercomparison Project (CMIP) phases 3 and 5 point out that upper-ocean stratification will strengthen in this century (e.g., Capotondi et al., 2012). While strengthened stratification may produce better light availability for the phytoplankton community, it will also prevent vertical nutrient supply to the euphotic zone (Doney, 2006). Studies in limited ocean regions in the North Pacific using repeat hydrographic cruise data have reported decreases in biological productivity and nutrients in the ML, probably due to increased stratification (Chiba et al., 2004; Watanabe et al., 2005). CMIP5 projections also suggest that the global average of oceanic primary production will decrease, although there is a large uncertainty due to the range of projected changes in density stratification (Fu et al., 2016). Therefore, understanding the change in the strength of the upper-ocean stratification is necessary not only for understanding the oceanic response to the radiative forcing that causes global warming but also for assessing accurately the impact on biogeochemical processes.

Unfortunately, observational evidence of the long-term trend of increasing stratification is limited about the global-averaged temperature field and limited in few ocean regions so far. The strengthening of the stratification that has been reported in the globally averaged temperature field

71

may not occur homogeneously, as the results of CMIP projection studies indicate spatially nonuniform changes in the stratification (e.g., Cabré et al., 2015). Indeed, Somavilla et al. (2017) reported that the stratification north of Hawaii decreased with a large amplitude of decadal variability from the 1990s, although the sea surface temperature (SST) increased. And, a recent investigation over large areas of the low- and mid-latitude Pacific oceans using profile data from 1997 to 2010 reported a trend of decreasing stratification (Dave & Lozier, 2013). These results also suggest that the simplest relation, namely that ocean warming is intensified near the surface and will result in increases in the local stratification, does not always hold in any ocean region and there are some other drivers of the change in stratification. Therefore, there are still large uncertainties of the observed long-term change in upper-ocean density stratification and its driver that may be due to spatial nonuniformity and/or decadal or longer variability. Observational description, with as great a spatial and temporal coverage as possible, about the long-term density stratification change itself and about what is the drivers (i.e. surface/subsurface temperature and salinity change) is needed.

In the study of this chapter, we aim at giving a global description of the long-term change in the upper-ocean stratification at this present time using only unprocessed historical observational profiles as many as we are available. The remainder of this paper is organized as follows. The dataset and processing methods are outlined in section 4.2. In section 4.3, we present the trends in density stratification and the contributions of thermal and/or haline stratification to these trends. The relationship between interannual to decadal variability of the stratification and climate mode in the respective ocean region is investigated in section 4.4.

4.2 Data and methods

We use historical in situ observed temperature (T) and salinity (S) profiles archived in the World Ocean Database 2013 (WOD13; Boyer et al., 2013) for 1960–2017. To quantify the strength of the upper-ocean stratification, we use here a metric defined as the potential density difference between the surface and 200 m depth ($\Delta\rho200$). This simple metric is not necessarily optimal for representing the characteristics of the stratification or for quantitative analysis (e.g. Somavilla et al., 2017); however, since it has been widely used in both model and observational studies, it allows us to compare our results with those of previous studies, to assess their reliability. Moreover, the simplicity of $\Delta\rho200$ means it is not affected by changes in observational instrument and its vertical resolution (Fig. 4.1g; see also Appendix 4A).

To calculate the metric representing the strength of upper-ocean stratification ($\Delta\rho200$), we

only use profiles with maximum observation depth greater than 200 m and identified by the quality control (QC) procedures of WOD as "Accepted value (passed through value range, density inversion, and gradient check)" over the whole profile. This gave us 2,178,542 profiles in total from five observational platforms (Fig. 4.1). All T/S profiles are linearly interpolated onto the surface (assigned at 10 m) and 200 m depth, and then the potential density and stratification ($\Delta\rho 200$) are calculated. In addition, using a linearized equation of state, we evaluated the contributions of thermal and haline stratification to the density stratification, as follows:

$$\Delta\rho 200 \sim \Delta\rho_T 200 + \Delta\rho_S 200,$$

where

$$\Delta\rho_T 200 = -\alpha\rho\big(T(200\text{m}) - T(10\text{m})\big), \tag{4.1}$$

and

$$\Delta\rho_S 200 = \beta\rho\big(S(200\text{m}) - S(10\text{m})\big),$$

where α and β are the thermal expansion and haline contraction coefficients of seawater, respectively. Note that the discrepancy between $\Delta\rho 200$ and the sum of $\Delta\rho_T 200$ and $\Delta\rho_S 200$ is very small in the T/S ranges of this analytical procedure, so that Eq. 1 provides good estimates of T/S contributions (c. f., Fig. 4.2b–d, 4.3a–c). To further control the data quality, in addition to the WOD QC procedure for T/S profiles, we exclude individual $\Delta\rho 200$ values that depart from the monthly mean by three standard deviations in each of 1° (latitude) × 1° (longitude) grid cell. The monthly climatology is obtained by averaging the quality-controlled $\Delta\rho 200$ values in each of 1° (latitude) × 1° (longitude) grid cell.

In general, there is the predominant seasonal cycle in the upper ocean, consisting mainly of the ML deepening during the net surface cooling season and seasonal thermocline development during the net surface heating season, especially in mid- and high-latitude regions. In the study of this chapter, the seasons are defined using the maximum density stratification at each of grid cell. We defined "season I" on each of grid as three consecutive months centered on the month with maximum density stratification determined from the monthly climatology (Fig. 4.2a). Then, season II (III and IV) is defined as the next three months of the season I (II and III). To avoid artificial variability due to seasonal sampling bias, we first calculated anomalies by subtracting the monthly climatology from individual profile values. Furthermore, to remove mesoscale or smaller-scale signals, these anomalies are yearly or seasonally averaged over 5° (latitude) × 10° (longitude) (hereafter, refer to annual or seasonal anomaly). Long-term trends in each of grid cell are calculated from the annual anomalies using a least-squares fit. We assessed the statistical

significance using a Mann–Kendall rank statistic for linear trends and using Student's t-test for correlation and regression coefficients of regional-averaged time series, with estimates of the degree of freedom based on the zero-crossing correlation timescale.

To investigate the relationship between the interannual variability of the stratification and climate mode in the pespective ocean region, we used the SST based Niño 3.4 index (Trenberth, 1997), the empirical orthogonal function (EOF)-based Pacific Decadal Oscillation (PDO) index (Mantua et al., 1997), and the station-based North Atlantic Oscillation (NAO) index (Hurrell, 2003). In order to examine the well-known spatial distribution of the T/S variability associated with the above climate modes, we also used the Hadley Centre Sea Ice and Sea Surface Temperature data set (HadISST; Rayner et al. 2003) and Hadley Centre objectively analyzed T/S fields (EN4; Good et al. 2013).

4.3 Long-term changes in upper-ocean stratification

Linear trends of upper-ocean density stratification ($\Delta\rho200$) estimated from the annual anomalies show the strengthening of stratification from the 1960s in many regions of the global ocean (Fig. 4.3a). The strongest trends occur in the tropical Pacific–Indian warm pool region. Statistically significant trends are also detected in the subarctic and along the eastern boundary of the North Pacific, and from the equator to the subtropical and subpolar North Atlantic. The density stratification trends are relatively weak and less statistically significant south of 40°S. Remarkably, this spatial distribution is similar to that of future projection obtained by CMIP models (Capotondi et al., 2012, their fig. 15), which can be thought of as the oceanic response to the radiative forcing that causes global warming. Moreover, the spatial pattern and the values of the trends calculated with different starting years converge to those calculated from the 1960s as the analytical period becomes longer (Fig. 4.4). These suggest that we can capture the oceanic response to the radiative forcing associated with global warming. As shown by previous studies using relatively shorter-term observational data (e.g., Dave & Lozier, 2013), the trends from the 1990s, 2000s, and 2010s are less statistically significant for both enhancement and even weakening (in some places). The reason is likely because of the prevailing long-term variability on decadal and/or interannual timescales.

Decomposing the density stratification into thermal and haline stratification components using Eq. 4.1, we estimated the contributions of the changes in temperature and salinity to the density trends (Fig. 4.3a–c). The thermal stratification trends contribute most to the density stratification trends; i.e., the spatial distribution of the density stratification trend is caused mainly

by changes in the vertical thermal structure. On the other hand, salinity stratification trends show contributions to the density stratification trend comparable to those from the thermal stratification trend, especially in regions where there are significant salinity components of the density stratification in the climatological field (c.f., Fig. 4.2), such as the subarctic North Pacific and the Southern Ocean near Antarctica. The salinity stratification changes also contribute to a reduction in the density stratification in the subtropical South Atlantic, part of the subtropical North Atlantic, and the central North and South Pacific.

In accordance with the definition of density stratification, thermal and haline stratification components can be further decomposed into density trends due to changes in temperature and salinity at the surface (10 m) and subsurface (200 m). Relatively spatially uniform negative surface density trends caused by SST warming contribute to the strengthening of density stratification (Fig. 4.3e). The spatial pattern corresponds well with the SST warming from the 1960s, which shows weaker warming in the central Pacific and Southern Ocean (Huang et al., 2018).

Strong positive density trends due to subsurface cooling contribute to the strengthening of density stratification in the tropics (Fig. 4.3h). In the equatorial region, because the subsurface cooling trends are located around the western part of the tropical Pacific and eastern part of the tropical Indian Ocean, it is suggested that the equatorial part of the subsurface cooling is associated with weakening of the Walker circulation from the mid-twentieth century onward (Tokinaga et al., 2012). The weakening of the easterlies (westerlies) in the tropical Pacific (Indian Ocean) flattens the equatorial thermocline and results in subsurface cooling anomalies in the western (eastern) part of the tropical Pacific (Indian Ocean).

Subsurface density trends are also evident in the western part of the North Pacific and North Atlantic subtropical gyres, with reductions in density that contribute to the weakening of density stratification (Fig. 4.3g, h). These regions roughly correspond to the formation and subduction sites of the North Pacific subtropical and central mode water (NPSTMW and CMW, respectively; e.g., Oka & Qiu, 2012) and North Atlantic subtropical mode/eighteen-degree water (NASTMW/EDW; e.g., Joyce, 2012), respectively. These subducted water masses enhance the global warming signals in the subsurface relative to the surrounding regions (Sugimoto et al., 2017). Consequently, the enhanced subsurface warming that is comparable to the surface warming mitigates the increasing trends of density stratification in those regions. Contrary to the well-documented intuitive view that the upper-ocean density stratification is enhanced due to the surface intensification of the global warming signal, the regions where the subsurface contribution

surpasses that of the surface account for ~36% of the regions of strengthened density stratification (Fig. 4.5).

The trend field of the surface density due to the change in the sea surface salinity (SSS) reveals the regions showing systematic SSS contribution, although the regions with statistically significant trends are somewhat small (Fig. 4.3f). Negative surface density trends caused by decreased salinity occur in the subarctic North Pacific and the tropical warm pool region. Positive trends due to salinification occur in the subtropical North Pacific and Atlantic. These trends are consistent with the reported tendency of near-surface salinity associated with intensification of the global water cycle, which is characterized by SSS salinification (freshening) in regions of net evaporation (precipitation) (Durack & Wijffels, 2010; Hosoda et al., 2009). Subsurface salinity components of density change show significant negative trends, contributing to weakening density stratification, in the central North Pacific and the equatorial margins of the Pacific and Atlantic subtropical gyre (Fig. 4.3i). Because the freshening trends along the equatorial margins of the subtropical gyre are accompanied by subsurface cooling trends (Fig. 4.3h), it is consistent with the poleward displacement of the mean meridional temperature and salinity structures (Levitus et al., 2009; Rhein et al., 2013). On the other hand, the negative density trends due to subsurface freshening in the central North Pacific appear to correspond to the freshening of the North Pacific central water, as shown in Durack & Wijffels (2010).

Table 4.1 lists the regional trends in density stratification estimated from the yearly time series of annual $\Delta\rho200$ anomaly averaged over ocean regions (Fig. 4.6a) with no spatial interpolation; i.e., using only grid cells where data exist for regional averaging (missing grid cells are neglected). As expected from the results in Fig. 4.3, significant strengthening of the upper-ocean stratification has continued from the 1960s in all regions except the Arctic Ocean. Note that the regional trend over the Arctic Ocean is based almost entirely on the trends in the Atlantic sector of the Arctic Ocean, given the lack of observations in other sectors. The largest change occurs in the tropical Pacific, at a rate of 0.0881 kg m^{-3} decade^{-1}, followed by the Indian Ocean. In the global average, the density stratification is strengthening at a rate of 0.0365 kg m^{-3} decade^{-1} and has thus increased by ~0.21 kg m^{-3} over these 58 years. This strengthening corresponds to ~11.8% of the climatological annual mean stratification (1.80 kg m^{-3}). This global average rate of strengthening of the upper-ocean stratification is equivalent to 74% of that estimated by the ensemble-mean of CMIP 5 models following the RCP 8.5 scenario (Fu et al., 2016), although the period of analysis differs between the studies.

To take account of the seasonal variability of the upper ocean, the trends estimated from the

yearly time series of seasonally averaged $\Delta\rho200$ anomalies (seasonal anomalies) are also listed in Table 4.1. The trends in each of ocean region seem to show seasonal dependencies. The seasonal variations of the trends, however, do not exceed the range of the uncertainties in any ocean region, except for the North Atlantic where the winter ML becomes deeper than 200 m over most of the region.

4.4 Detrended variability and climate mode

For regions with relatively dense data coverage and spatiotemporally unbiased observations (i.e., the North Pacific, North Atlantic, and tropical Pacific), we investigated the relationship between the detrended variability of the density stratification and the prevailing climate mode in the respective region. We use normalized and detrended yearly time series of the density stratification obtained by averaging annual anomalies over each of ocean region with no spatial interpolation.

In the tropical Pacific region, the upper-ocean density stratification is highly significantly correlated with the Niño 3.4 index that represents the occurrence of the El Niño/La Niña (Fig. 4.6b). When the Niño3.4 index is positive (negative), indicating the occurrence of El Niño (La Niña), the SSTs are higher (lower) in the eastern tropical Pacific and thus the density stratification is intensified (weakened), while in the western tropical Pacific the subsurface cooling (warming) anomalies due to the zonally flattened (tilted) thermocline strengthen (weaken) the density stratifications (Fig. 4.7). Freshening anomalies in SSS during El Niño, which have the maxima in the western part (Singh et al. 2011), also contribute to strengthening the density stratification (Fig. 4.7). It is well-known that the El Niño and La Niña phenomena are closely related to the weakening and strengthening of the Walker circulation on an interannual timescale, named as the Southern Oscillation (e.g., Trenberth & Hoar, 1996). Thus, this correlation is interpreted as being analogous to the explanation in section 3 of the increasing trends of density stratification due to a weakened Walker circulation in the tropical warm pool region.

In the North Atlantic, the variability in density stratification has no simultaneous correlations with any prevailing climate mode such as the NAO or Atlantic Multi-decadal Oscillation (AMO). However, the detrended time series shows a statistically significant lagged correlation ($R= -0.57$) with the leading NAO index (Fig. 4.6c). The positive NAO phase is characterized by warmer SST south of the Gulf Stream and cooler SST north of 40°N due to stronger westerly winds (Visbeck et al., 2003). The negative correlation between the density stratification and the NAO index is qualitatively consistent with the cooler (warmer) SST and stronger (weaker) near-surface mixing induced by enhanced (weakened) westerly winds to the

north of 40°N during positive (negative) NAO. On the other hand, the warmer SST south of the Gulf Stream during positive NAO is inconsistent with this negative correlation. The regions of the warmer SST signal roughly correspond to and/or include the sites of water mass formation and subduction. The variability in density stratification associated with the SST changes may have a smaller signal in these regions because the anomalous SST signals can be carried well below the surface due to the subduction process, thereby weakening the anomalous density stratification.

Note that the correlation between variabilities in the density stratification and NAO reaches its maximum with an NAO lead of 2 years and is still significant ($R = -0.68$) in low-pass filtered time series (Fig. 4.6c). This feature supports the explanation of SST-driven stratification variability because cool SST anomalies induced by positive NAO extend over the wider region of the North Atlantic with a 2-year lag (Fig. 4.8; see also Visbeck et al., 2003). Therefore, it is suggested that the lagged negative correlation of the density stratification in the North Atlantic with the NAO is largely explained by its SST variability.

Averaged time series over the whole of the North Pacific do not have a statistically significant correlation with the PDO index (data not shown). However, the SST pattern of the PDO, which shows the prevailing variance on interannual to decadal timescales over the entire basin, has a spatial pattern of two poles of the opposite sign in the mid-latitude region (e.g., Newman et al. 2016). To examine the possibility that the opposite signals cancel each other when averaging over a large area, we divide the North Pacific into two regions corresponding to the two poles of PDO SST variation: one is the southwestern North Pacific and the other includes the northern North Pacific and the region along the North American coast (Fig. 4.6a, Fig. 4.8). We then find the significant positive correlation in the northern and eastern regions, and significant negative correlation in the southwestern regions covering the subtropical gyre (Fig. 4.6d). These relationships are qualitatively consistent with cooler SSTs associated with stronger westerly winds in the southwestern region and relatively warmer SSTs in the northern and eastern region for a positive PDO phase, and vice versa. The correlation coefficients, however, are relatively small especially in the southwestern region ($R = -0.43$), although it is statistically significant. This suggests that subsurface variability is also an important factor on the interannual variation of the stratification.

In the present study, we could not analyze the variability in stratification and its relationship to the climate mode in oceans of the Southern Hemisphere and polar regions because the observational data were not able to resolve the year-to-year variability over long periods. Regionally averaged time series over the Indian Ocean and tropical Atlantic show no correlation

with the Indian Ocean Dipole Mode index (Saji et al., 1999) and a weak but significant negative correlation with the NAO index ($R = -0.37$, $p = 0.05$), respectively, although these correlations are estimated from time series with a few gaps.

4.5 Summary and discussion

We have investigated the long-term trends and variability in upper-ocean stratification starting from the 1960s using only observational profiles. Strengthening of the stratification is detected over most of the global ocean, except for the Arctic Ocean, and the spatial distribution resembles future projections by CMIP climate models. In the global average, rapid strengthening is evident, amounting to an increase of 11.8% over 58 years with respect to the mean stratification. This estimate appears to be higher than the ~4% increase in density stratification from 1971 to 2010 provided by the Intergovernmental Panel on Climate Change (IPCC) Fifth Assessment Report (Levitus et al., 2009; Rhein et al., 2013). Although there are some subtle differences in the two analyses such as the periods and areal coverage, the main cause of the discrepancy seems to be whether the anomalies are spatially interpolated. Generally, widely used objective interpolation methods tend to attenuate anomalies, especially where data are relatively sparse, such as for the 1960s/1970s and in the Southern Hemisphere. Spatial interpolation is not used in the present study, so the present estimate may represent the upper limit of the range that includes the true value. Indeed, the same analysis with the assumption that grid cells with missing data have zero anomalies showed a smaller increase in global density stratification (~6.6%).

Regional stratification trends are spatially nonuniform. The region with the fastest strengthening trend is the tropical Pacific, followed by the Indian Ocean. In addition to the contribution of warming SST to strengthening the density stratification, subsurface cooling due to weakening of the Walker circulation also contributes to the strengthening in the tropical warm pool region, while the strengthening is reduced by enhanced subsurface warming associated with water mass subduction in the western parts of the subtropical gyre in the Northern Hemisphere. In addition to the well-documented explanation of strengthening stratification, it is revealed that subsurface changes are also important for the estimation of the trends. Moreover, the haline stratification changes due to the intensification of the global water cycle and changes in ocean circulation also have significant impacts on the changes in density stratification.

In each basin, the variability in stratification associated with each particular climate mode is evident from the detrended yearly time series. The region-averaged variability indicates a positive correlation with the Niño 3.4 index in the tropical Pacific, a negative lagged correlation

with the NAO index in the North Atlantic, and correspondence with SST variations related to the PDO in the North Pacific. Since the climate modes are closely related to variability in large-scale atmospheric circulation, oceanic circulation, and biogeochemical processes (e.g., Mantua et al., 1997), these significant correlations in each basin raise the possibility that the variability in density stratification mediates the impact of large-scale atmospheric changes on biogeochemical processes, as suggested by Behrenfeld et al. (2006).

In this chapter, the use of the simplest metric representing stratification may have limited our ability to conduct more quantitative analysis. Therefore, results in the present study provide an only descriptive view of long-term change and variability in the stratification and further studies are needed to clarify the mechanisms causing the variability. It is important to describe the long-term stratification changes quantitatively from observational data using more appropriate metrics such as potential energy (e.g., Burchard & Hofmeister, 2008), employing globally and sustained vertical profile observations of uniform quality, such as those from the international Argo program. Moreover, adding biogeochemical properties (oxygen, chlorophyll, etc.) to regular high-vertical-resolution T/S observations by enhancing the Biogeochemical Argo network, we hope that future investigations will advance our understanding of physical-biogeochemical interactions in the upper ocean.

Appendix 4A: Increase in the upper-ocean stability

In Chapter 2, we used the Potential Energy Anomaly (PEA) to represent the strength of the upper-ocean seasonal stratification. Using the PEA, we can describe the upper-ocean condition as the "difficulty in mixing (i.e., stability)". The stability of the upper ocean is important for biogeochemical processes in the same context mentioned in introduction (Section 4.1).

Long-term trend of the upper-ocean PEA estimated from same dataset as that used for $\Delta\rho 200$ (c.f., Section 4.2) is shown in Figure A 4.1. The PEAs are computed from profiles vertically linear interpolated into 1-m intervals and the lower limit of the vertical integration (H in Eq. 2.1) is uniformly assigned to 200 m depth. The long-term trend of annual mean PEA is calculated and evaluated by same procedures as that for $\Delta\rho 200$. Spatial distribution of the estimated trends of the PEA seem to be consistent with that of $\Delta\rho 200$ (Fig. 4.3a), although the regions with statistically significant trends are somewhat small. This suggests that the strengthening of the upper-ocean stratification visualized by the increase in $\Delta\rho 200$, which is simplest indicator of the stratification, is indeed accompanied by the increase in the upper-ocean stability.

However, this result should be interpreted just as a reference because of the data qualities.

As we mentioned at Section 4.2, the vertical resolutions of the observational data used in this Chapter largely change depending on the year (Fig. 4.1g). It is suggested that the change in the vertical resolution has large impact for the calculation of the vertical integration. In Figure A 4.2, we show the two examples of the PEA calculations for the same profiles but different vertical resolutions (i.e., the raw CTD profile that has the vertical resolution of 1-m interval and reconstructed profile by linear interpolation from the values at standard depths). Fig. A 4.2 shows the possibility that errors that is comparable to the estimated trends of the PEA occur in case that there is sharp stratification at the point of coarse resolution.
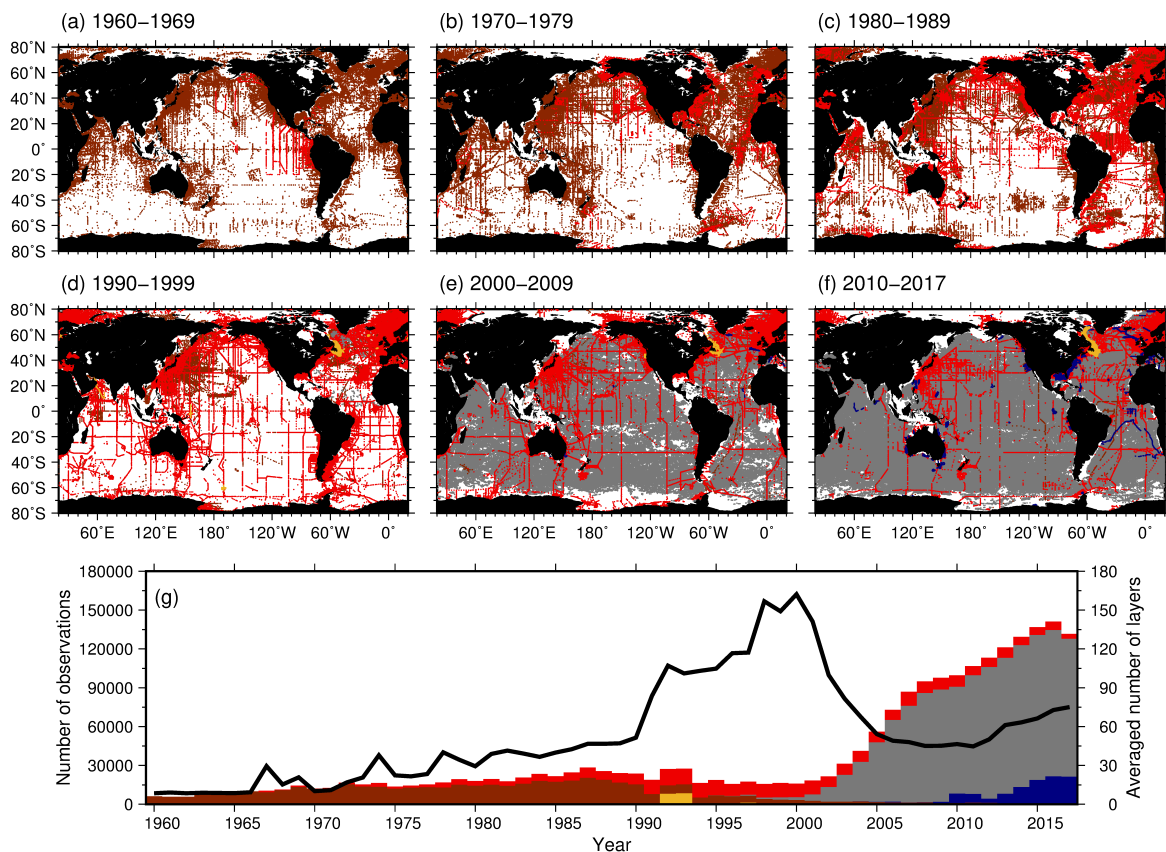
Figure 4.1. (a–f) Spatial distribution of T/S profiles used in this study and (g) the temporal change in the number (bars) and vertical resolution (black curve) of the profiles. The coloring follows the WOD13 dataset categories: Ocean Station Data (OSD, brown, including low-resolution CTD/XCTD data), Conductivity–Temperature–Depth data (CTD, red, including high-resolution XCTD data), Undulating Oceanographic Recorder data (UOR, yellow), Profiling Float data (PFL, grey), and Glider data (GLD, blue). The vertical resolution is defined as the number of observation layers in each profile from the surface to 200 m depth. In (g), "Average number of layers = 100" means there are 100 observations from the surface to 200 m depth in a profile and thus the vertical resolution of the profile is roughly 2 m.
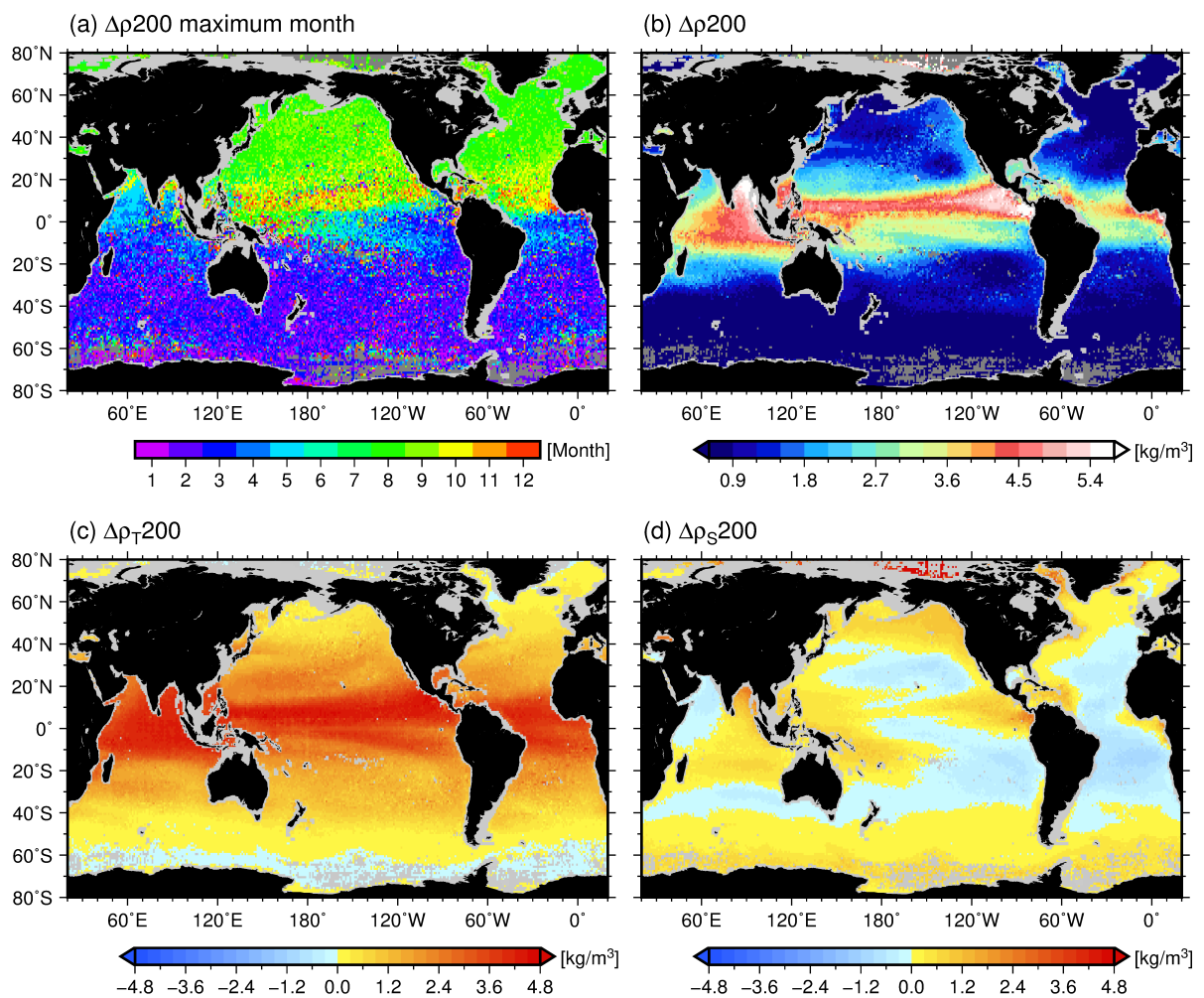
82

Figure 4.2. (a) Months of maximum upper-ocean stratification (Δρ200, defined here as the density difference between the surface and 200 m depth) determined from the monthly climatology. (b) Annual mean of the monthly climatology of Δρ200. Contributions of thermal (c) and haline (d) stratification to the annual mean density stratification (b) are shown.
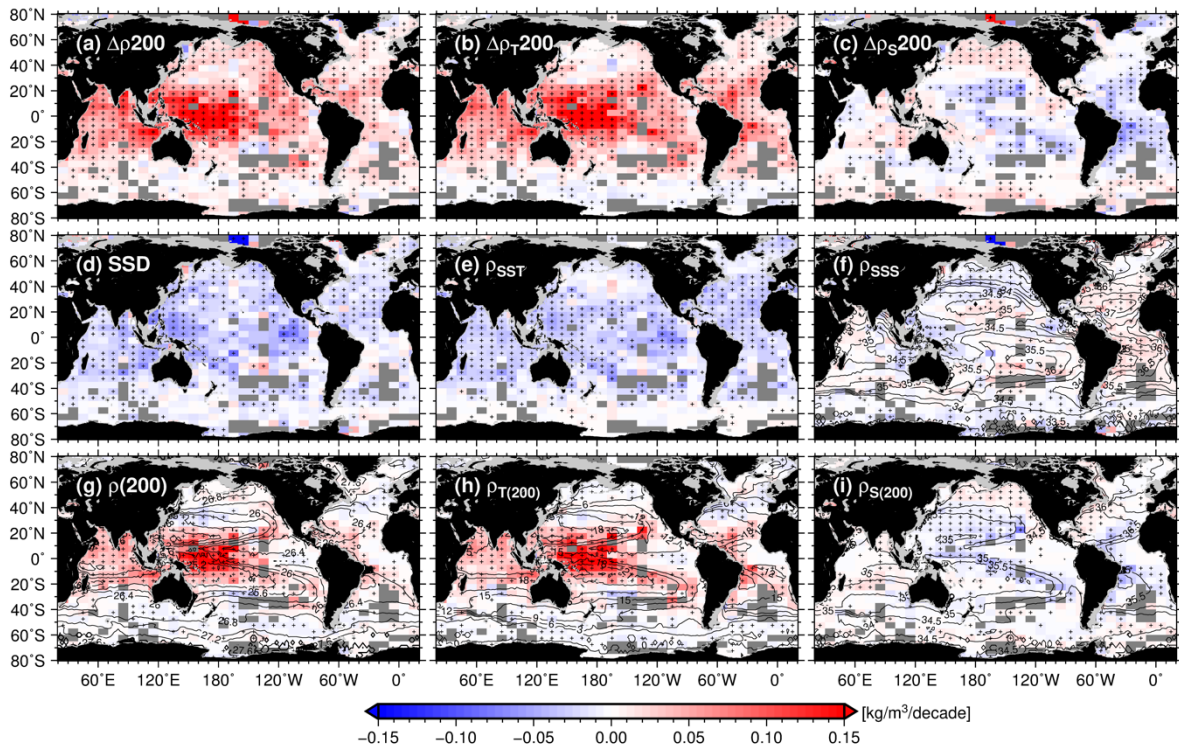
Figure 4.3. (a) Distribution of upper-ocean stratification (Δρ200) trends, starting from the 1960s. (b, c) Decompositions of the density stratification trends into the contributions of thermal and haline stratification. Surface and subsurface trends are shown for the density changes (d, g), for the density changes due to temperature changes (e, h), and for the density changes due to salinity changes (f, i). Climatological mean fields are shown by black contours for sea surface salinity (SSS) (f), potential density at 200 m (g), temperature at 200 m (h), and salinity at 200 m (i). Grid cells with missing values due to a lack of observations are shaded gray. The '+' symbols indicate statistically significant trends exceeding the 90% confidence level.
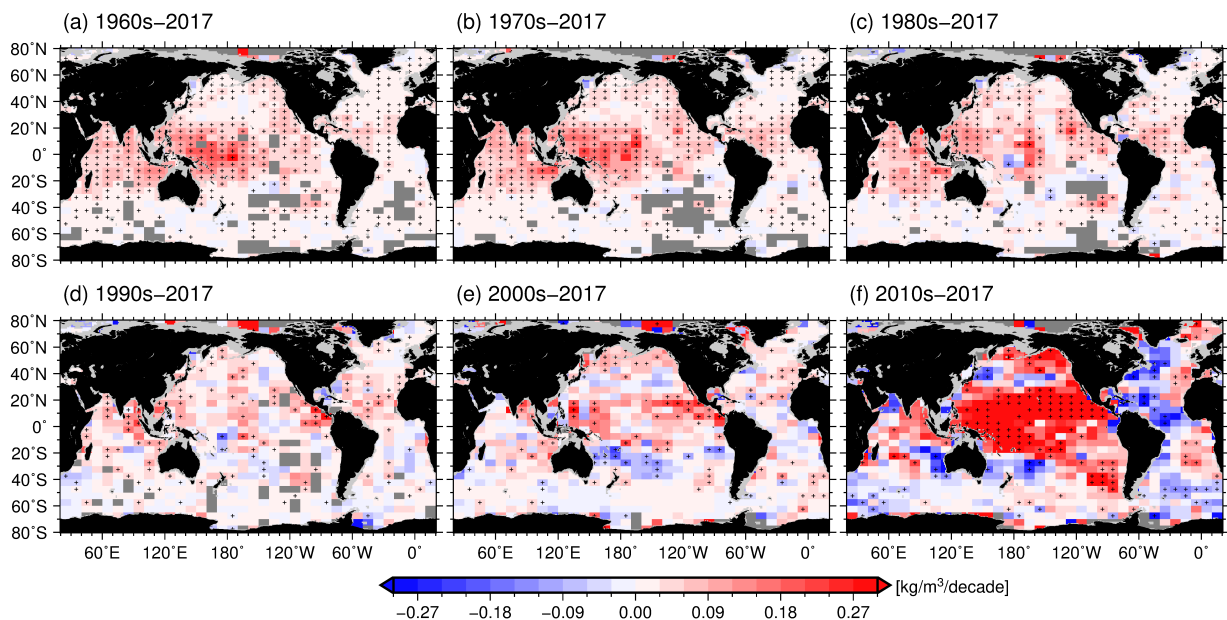
Figure 4.4. Distribution of upper-ocean stratification trends calculated for the different starting years: 1960s (a; same as Figure 3a), 1970s (b), 1980s (c), 1990s (d), 2000s (e), and 2010s (f). Grid cells with missing values due to a lack of data are shaded gray. The '+' symbols indicate statistically significant trends exceeding the 90% confidence level.
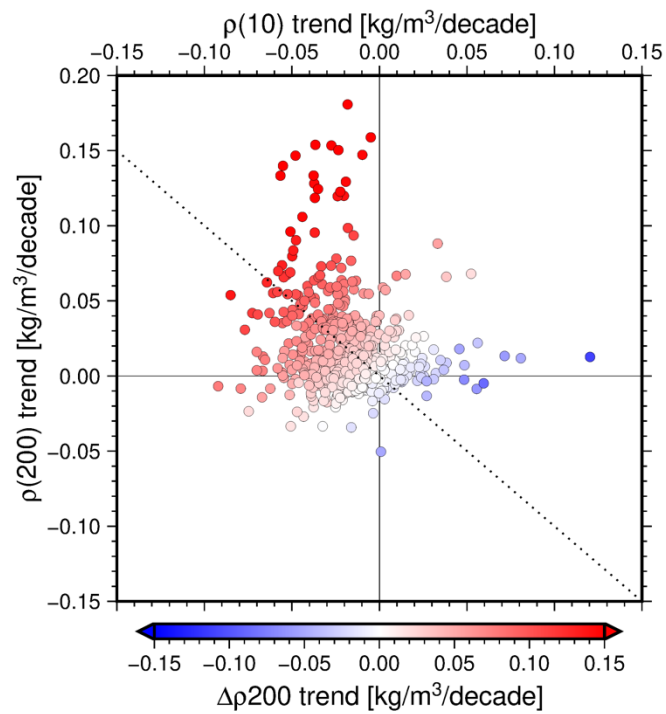
Figure 4.5. Relative contributions of sea surface density ($\rho(10)$) and subsurface density ($\rho(200)$) changes to upper-ocean stratification ($\Delta\rho200$) trends from the 1960s. The dotted line indicates equal contributions from an increase in subsurface density and decrease in surface density.

Table 4.1. Regionally Averaged Annual Mean Climatology of Density Stratification, Regional Trends Estimated from Annual and Seasonal Anomalies, and p-values (Student's t-test).

Ocean region	Annual mean $\Delta\rho200$ [kg/m^3]	Annual Trend ± standard error [kg/m^3/decade]		p	Season I Trend ± standard error [kg/m^3/decade]		p	Season II Trend ± standard error [kg/m^3/decade]		p	Season III Trend ± standard error [kg/m^3/decade]		p	Season IV Trend ± standard error [kg/m^3/decade]		p
North Pacific	1.56	0.0268 ± 0.0037		<0.01	0.0294 ± 0.0058		<0.01	0.0322 ± 0.0036		<0.01	0.0301 ± 0.0034		<0.01	0.0273 ± 0.0048		<0.01
Tropical Pacific	3.24	0.0881 ± 0.0092		<0.01	0.0849 ± 0.0113		<0.01	0.0934 ± 0.0130		<0.01	0.0911 ± 0.0115		<0.01	0.0883 ± 0.0106		<0.01
South Pacific	1.11	0.0167 ± 0.0044		<0.01	0.0124 ± 0.0069		0.08	0.0200 ± 0.0052		<0.01	0.0218 ± 0.0060		<0.01	0.0287 ± 0.0065		<0.01
North Atlantic	1.01	0.0170 ± 0.0025		<0.01	0.0158 ± 0.0041		<0.01	0.0231 ± 0.0035		<0.01	0.0138 ± 0.0023		<0.01	0.0143 ± 0.0027		<0.01
Tropical Atlantic	2.76	0.0232 ± 0.0061		<0.01	0.0260 ± 0.0071		<0.01	0.0211 ± 0.0090		0.02	0.0193 ± 0.0071		<0.01	0.0273 ± 0.0070		<0.01
South Atlantic	0.96	0.0161 ± 0.0055		<0.01	0.0150 ± 0.0090		0.10	0.0189 ± 0.0052		<0.01	0.0113 ± 0.0063		0.08	0.0097 ± 0.0072		0.18
Indian Ocean	2.72	0.0559 ± 0.0045		<0.01	0.0598 ± 0.0075		<0.01	0.0594 ± 0.0064		<0.01	0.0552 ± 0.0062		<0.01	0.0613 ± 0.0059		<0.01
Southern Ocean	0.40	0.0075 ± 0.0011		<0.01	0.0085 ± 0.0018		<0.01	- ± -		-	- ± -		-	0.0066 ± 0.0022		<0.01
Arctic Ocean	1.69	−0.0088 ± 0.0068		0.20	−0.0206 ± 0.0098		0.04	- ± -		-	- ± -		-	- ± -		-
Global average	1.80	0.0365														

Note: Global-average trend and mean $\Delta\rho200$ are obtained by area-weighted averaging of the listed regional trends and mean $\Delta\rho200$. Trends are not estimated for regions and seasons with insufficient observations to calculate the yearly time series.
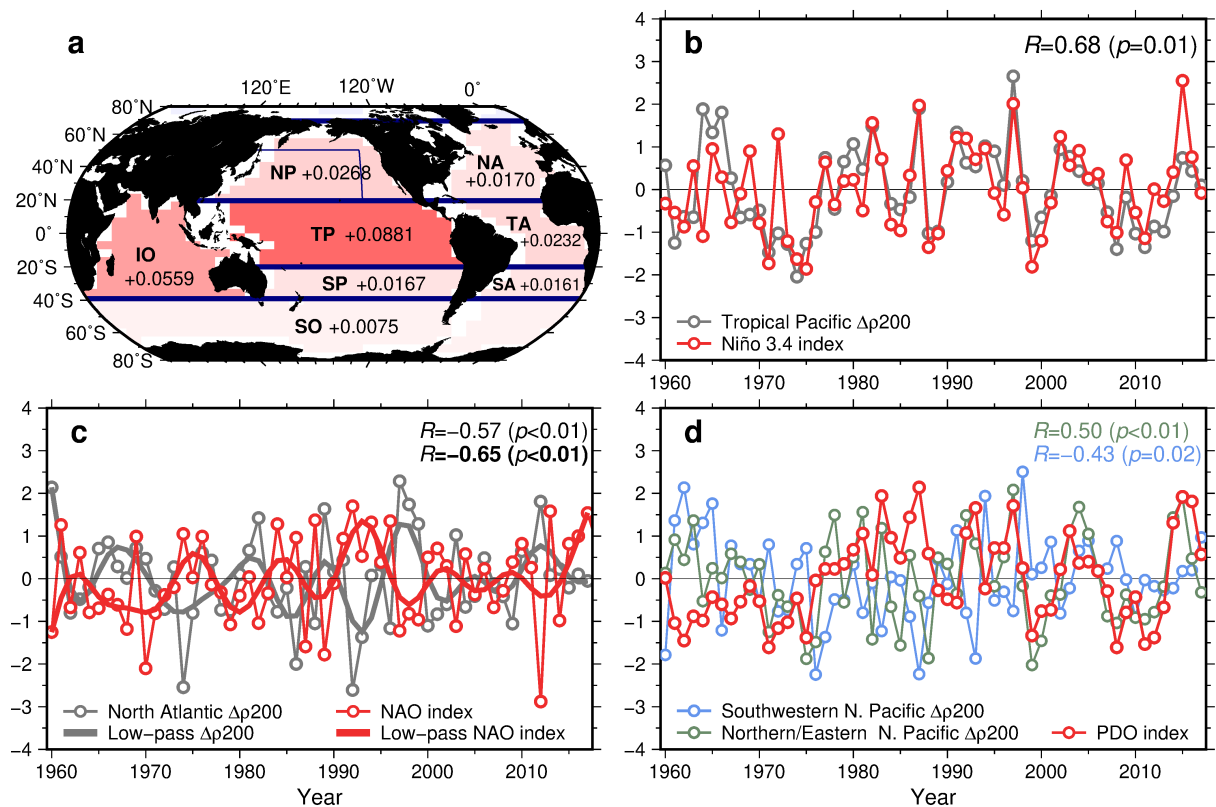
Figure 4.6. (a) Regional trends (same as Table 1) and definitions of the regions used to calculate the regional trends and regional averaged yearly time series. (b–d) Normalized and detrended yearly time series of the annual anomaly of the upper-ocean density stratification ($\Delta\rho200$) and climate mode indices are shown for the tropical Pacific (b), North Atlantic (c), and North Pacific (d). The NAO index is shown with a lead of two years. The blue rectangle in the North Pacific in (a) is used to divide the region into the two poles of the PDO SST variation (see text).
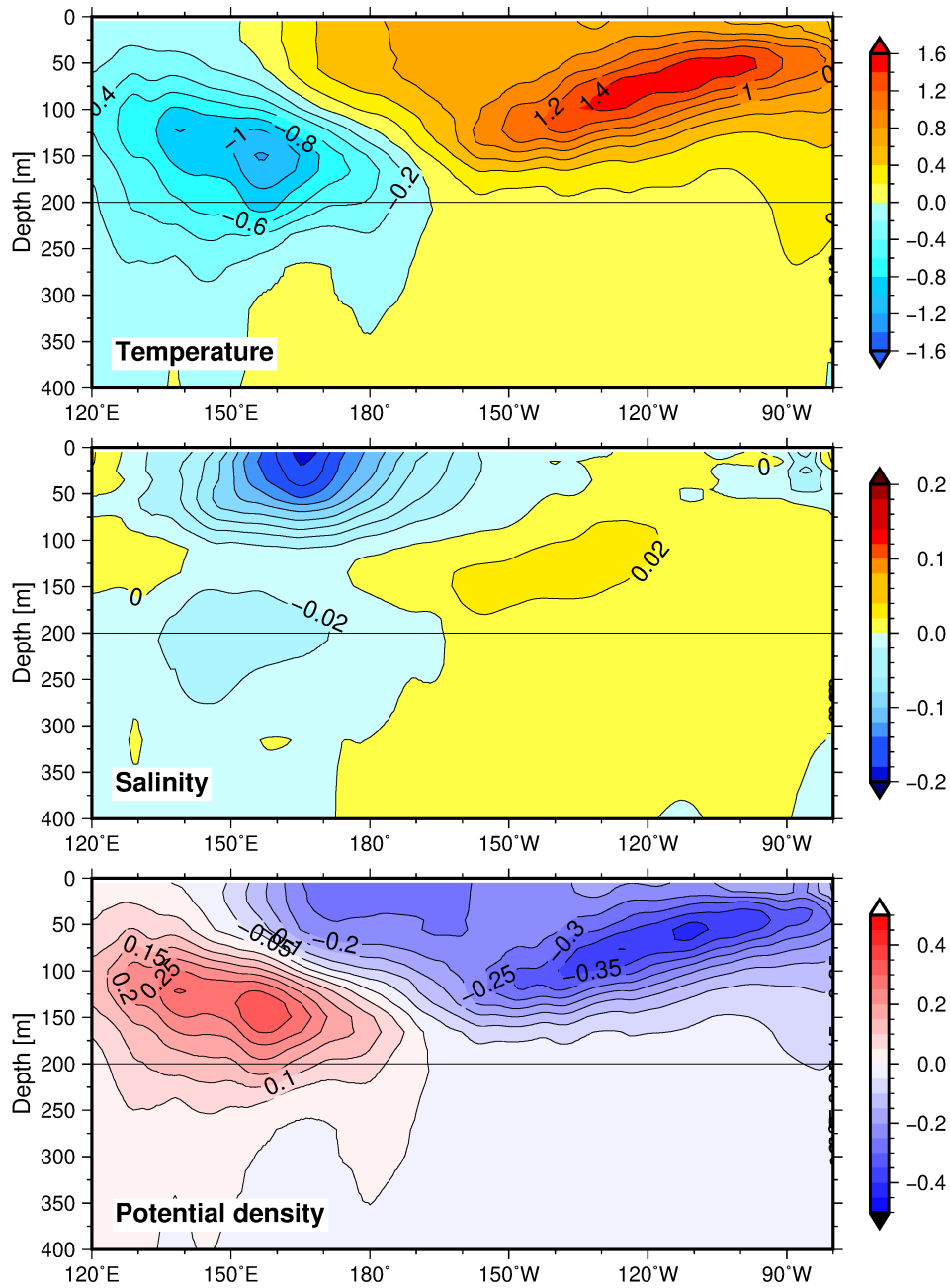
Figure 4.7. Regression of the temperature (°C), salinity (PSU), and potential density (kg m^{-3}) on the normalized Niño3.4 index computed from the EN4 T/S fields (1960–2017).

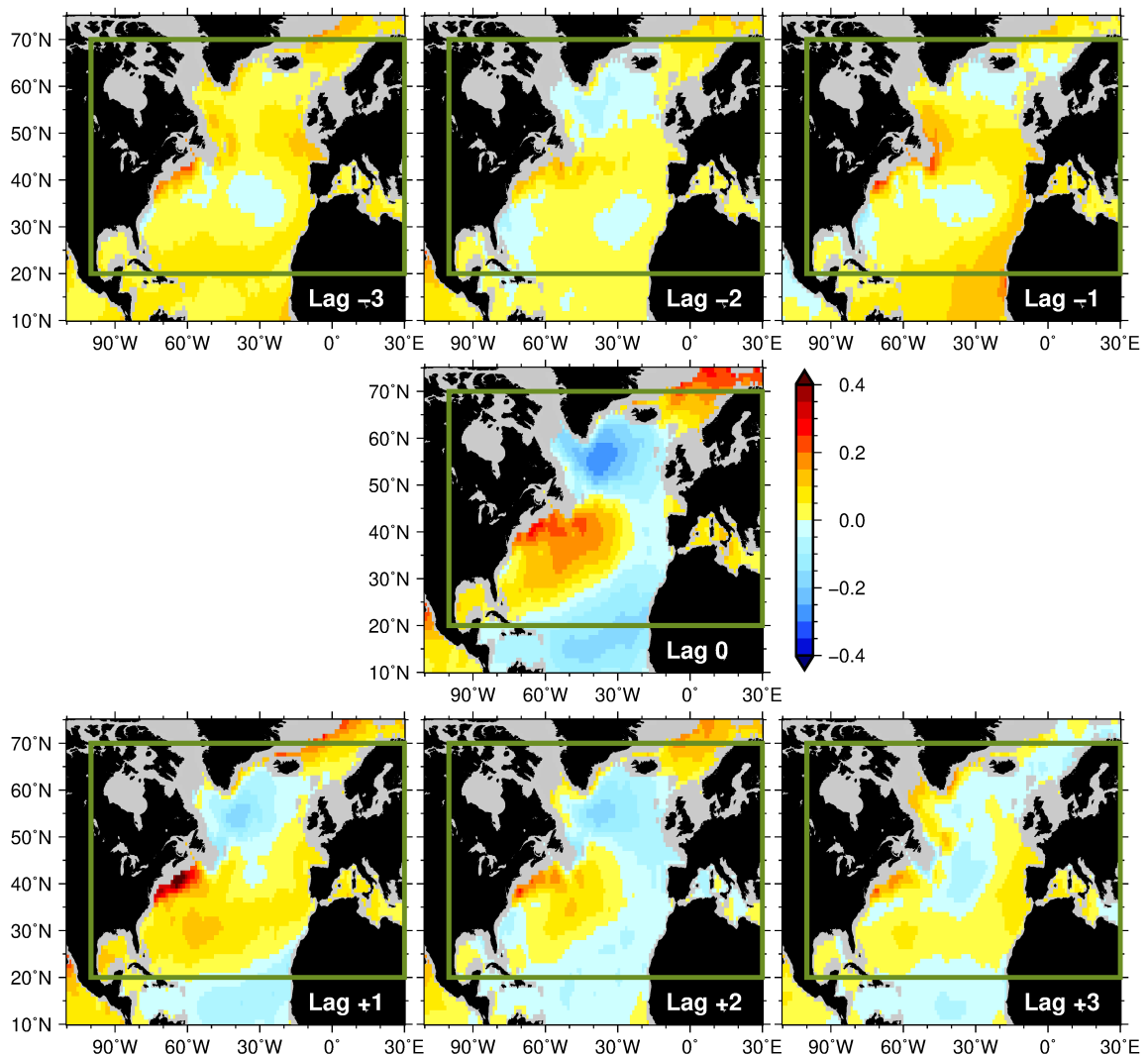Figure 4.8. Spatial distribution of the lagged regression coefficient (℃) of the annual mean SST onto the normalized NAO index. The regressions are computed from the HadISST (1960–2017). Positive lags indicate the lead of the NAO index. Green rectangle shows the region used to average $\Delta\rho200$ anomaly in Fig. 4.6c.
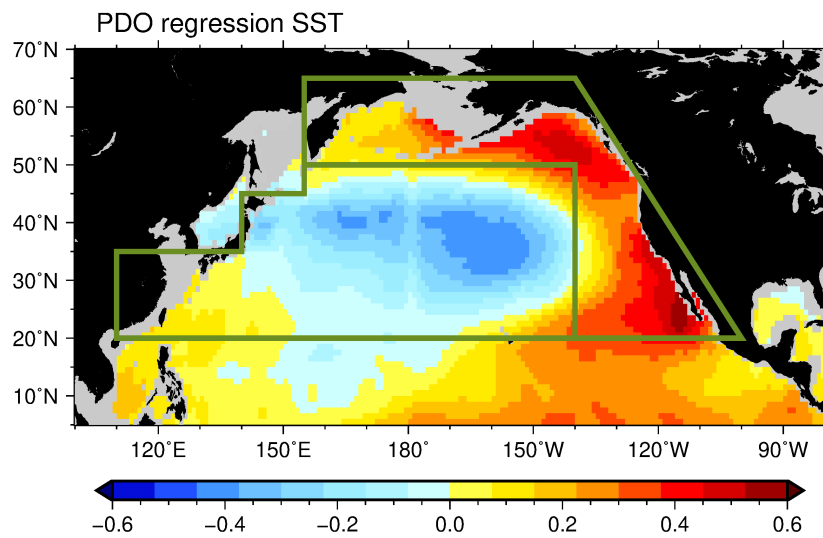
Figure 4.9. Spatial distribution of the regression coefficient (℃) of the annual mean SST onto the normalized PDO index. The regressions are computed from the HadISST (1960–2017). The two regions surrounded by green lines indicates the definitions used to obtain the time series in Fig. 4.6d.
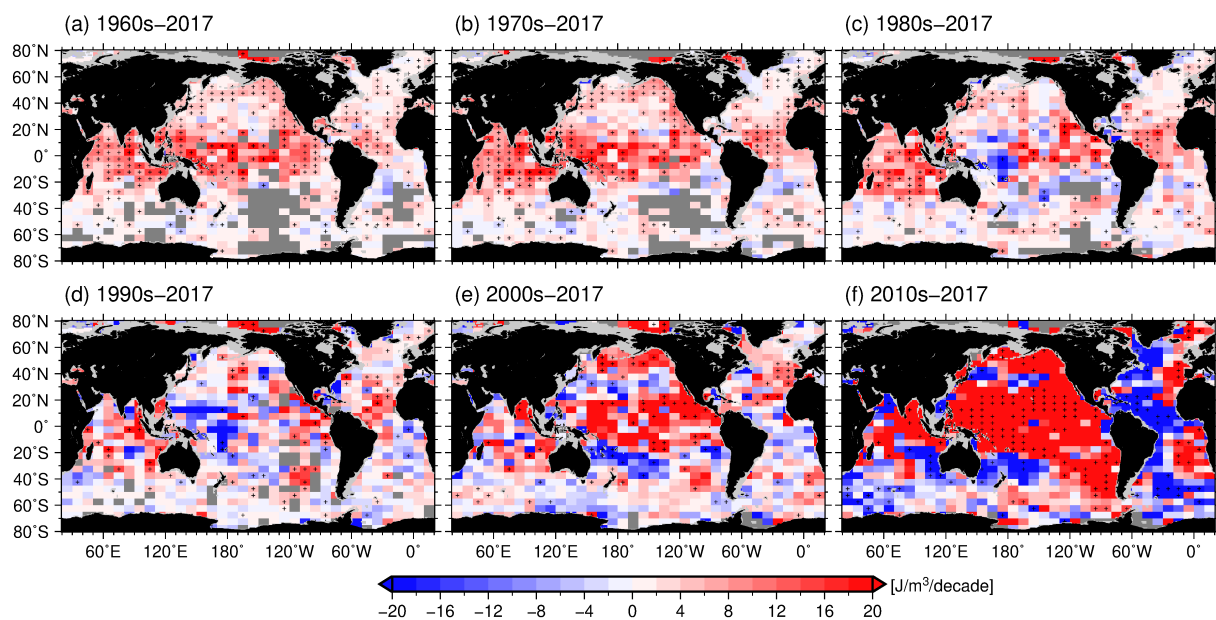
Figure A 4.1. Distribution of upper-ocean PEA trends calculated for the different starting years: 1960s (a), 1970s (b), 1980s (c), 1990s (d), 2000s (e), and 2010s (f). Grid cells with missing values due to a lack of data are shaded gray. The '+' symbols indicate statistically significant trends exceeding the 90% confidence level.
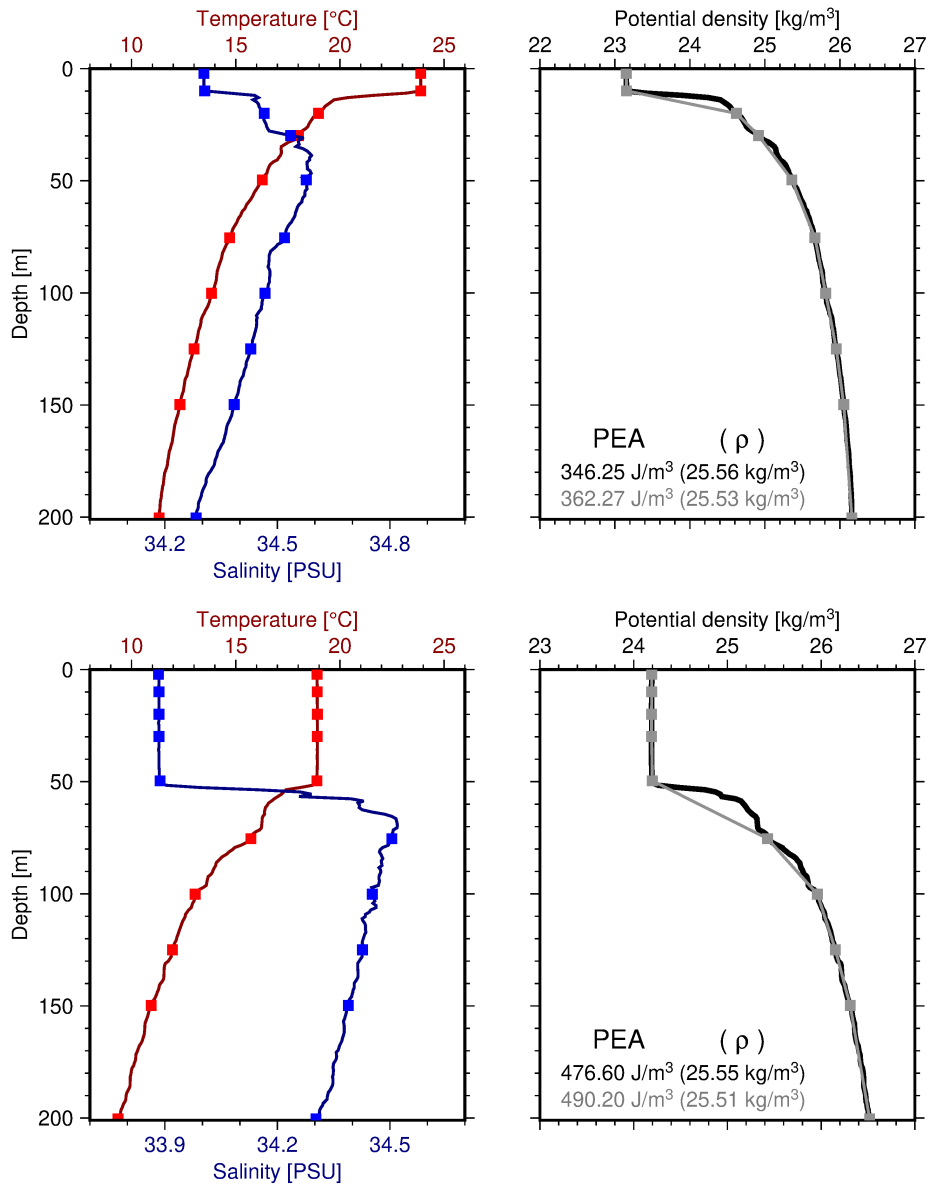
Figure A 4.2. Examples of CTD profiles of the 1-m vertical intervals from WOD13 at 169°E, 40°N on August 25, 2012 (uppers), and at 144°E, 37°N on November 12, 2008 (lowers). Squares on the lines show the T/S and density values at the standard depths. Grey lines in right panels indicate vertical linear interpolation of the standard depth observations. The PEA values are calculated from the raw profile (black line) and vertically interpolated standard depth profile (grey squares with line).

Chapter 5
General conclusion

Studies in the present dissertation were done with our main focus of clarifying the mechanism of the development of the seasonal stratification quantitatively from the observational dataset. We also aimed to obtain a better understandings of roles of the upper-ocean stratification on the climate systems through investigating the long-term change and interannual/decadal variability. We summarize the main results as follows.

In Chapter 2, through quantification of the strength of the seasonal stratification as potential energy required to make the density stratified water column vertically homogeneous (PEA), we described the development of the stratification quantitatively with use of the time-dependent equation of PEA. We also discussed the causes of the regional differences of the development and the vertical structure of the seasonal stratification. In the North Pacific, the PEA computed from temperature and salinity profiles collected by Argo float from 2006 to 2016 show the regional differences in the amplitude and phase of the development of the seasonal stratification in the North Pacific. The spatial distribution of PEA also differs from the well-known distribution of the mixed layer depth.

To clarify which processes dominantly contribute to the development and how their processes are balanced, we performed the PEA budget analysis based on the satellite-based atmospheric dataset. As a result, we found that the seasonal stratification develops, in a large part of the North Pacific, under a vertical one-dimensional balance between the creation by the atmospheric buoyancy forcing and the destruction by the vertical mixing in the water column. In the warming season when the vertical mixing is commonly considered to be relatively weaker than the cooling season, estimated vertical diffusivity of the water column from the budget reaches to the order of 10^{-4} m^2 s^{-1}. The diffusivity shows significant spatial and seasonal variability, suggesting its dependence on the strength of local wind forcing.

On the other hand, the contribution from lateral processes, which have been difficult to quantify so far, are shown in some limited regions of the North Pacific. Throughout the warming season, vertical shear of horizontal velocity caused by the northward Ekman velocity in the region of trade wind contributes, but is not dominant, to the development of the seasonal stratification, because of carrying relatively warm and thus light southern water on cool and dense northern water. In the Kuroshio Extension region, advection of PEA also significantly contributes to the development of the seasonal stratification, which is comparable to the atmospheric buoyancy

forcing and corresponds up to 40% of the time rate of change in PEA.

In order to discuss the reason for the regional difference of the development of the seasonal stratification, we compared the PEA budgets in two regions which have the same total buoyancy gain from the beginning of the warming season. As a result, we showed that spatial distribution of the "composition" of buoyancy forcing, in addition to the "total magnitude" as generally thought, is important for producing the regional difference in the development of the seasonal stratification. In the case of the North Pacific, it is found that the condition, satisfied in its northern part, that both the penetrating component (shortwave radiation) and the non-penetrating components (other buoyancy fluxes) contribute to the total buoyancy gain is more favorable for the formation of more intense PEA (i.e. sharper) stratification.

In Chapter 3, we introduced the PV framework to understand the impact of summertime preconditioning by the seasonal stratification on the development of the winter mixed layer. We firstly addressed formalization for estimation of the sea surface net PV flux from the observational dataset and then the description of its climatological feature in the northern oceans. To reduce previously reported bias of oceanic PV gain, we revised the scaling laws with consideration of the penetration of the shortwave radiation at the base of the mixed layer and wind-driven mixing even in the warming season (c.f. Chapter 2). Newly estimated net surface PV flux was significantly improved, being more consistent with independently calculated variation in the PV of ocean interior. The net surface PV flux consists of the dominant and seasonal varying diabatic contribution from the buoyancy flux and vertical mixing and relatively small mechanical contribution by the surface wind friction. In the annual mean field, well-known classical pictures of air-sea PV exchange are shown: the PV gain (loss) occurs in low (high) latitude in both the North Pacific and the North Atlantic. On the other hand, we found that the balance between the contributions is different between the ocean regions: The mechanical contribution is more important in the North Pacific, and the diabatic contribution is dominant in the high latitude region of the North Atlantic.

The annual mean PV fluxed averaged along the density outcrop windows also show two peaks (a peak) of the PV loss at the denser density of the North Pacific (the North Atlantic). These three peaks occur in the density ranges of the major water masses (STMW and CMW in the North Pacific and EDW in the North Atlantic), as reflecting that the water mass formation closely relates to the oceanic PV loss. We then estimated the Eulerian annual subduction rate from the net surface PV flux. Although we found some features differed from previously estimated Lagrangian subduction rate, further investigations are needed for examining the robustness of the results.

Improved net surface PV flux shows significant interannual variability exceed 20% of the climatological mean values and its variability is mainly caused by dominant buoyancy component of the flux. Performing the EOF analysis to the annual mean PV flux anomaly of the entire basin of the North Pacific and North Atlantic, the PDO-like decadal variability is detected as the first mode, explaining ~20 % of the total variance. In order to investigate which season (summertime PV input or wintertime PV extraction) contributes to the interannual variability in the annual mean PV flux, we computed their interannual variabilities separately and compared them, at the end of Chapter 3. As a result, we found that the interannual variability in summertime PV forcing (input) are significantly larger than that of winter (extraction) in the previously reported regions where the summertime atmospheric forcing has an impact as preconditioning on the interannual variability in the winter ML depth.

In Chapter 4, we investigated globally the long-term change and variability in the upper-ocean stratification. To be able to consider influences of the regional difference of the trends and decadal variability on detecting the long-term changes, we used temperature and salinity observations with spatial and temporal coverage as wide as possible. As a result, strengthening trends of the upper-ocean stratification from the 1960s were detected over most of the global ocean, except for the Arctic Ocean. In the global average, the speed of strengthening is 0.0365 kg/m^3/decade, corresponding to an increase of 6.6–11.8% over 58 years with respect to the mean stratification. The spatial distribution resembles the future projections by CMIP climate models and the speed is comparable to 74% of that estimated by the RCP 8.5 scenario. We would like to emphasize that, in addition to the well-mentioned effect of surface intensification of the warming signal, the subsurface temperature changes and haline stratification changes also have significant impacts on the long-term changes in density stratification.

In each ocean region, the decadal/interannual variabilities in the upper-ocean stratification associated with each particular climate mode are detected from the detrended yearly time series. We indicated that these time series indicate a positive correlation with the Niño 3.4 index in the tropical Pacific, a negative lagged correlation with the NAO index in the North Atlantic, and correspondence with SST variations related to the PDO in the North Pacific.

In the present dissertation, we described the seasonal cycle of the upper ocean from two different perspectives with the use of newly introduced concepts. In Chapter 2, we applied the concept of PEA to the seasonal stratification in the open ocean for the first time and shows its utility for quantitative analysis. Although this analysis was done on the monthly time scale and 1° × 1° spatial scale, the contributions from shorter time and smaller spatial scale (e.g., the physics

of the vertical mixing in the seasonal stratification) have to be examined by in situ time series observations in the future works. However, a methodology of the PEA budget analysis shown in Chapter 2 can be utilized for quantifying and understanding of the impacts of physical variability on the upper-ocean biogeochemical phenomena. Moreover, the estimate of the surface PV flux improved in this study has the potential to be used not only for the description of the upper-ocean seasonal cycle but also for understanding the fundamental ocean dynamics including the mechanism of the atmosphere-ocean coupled variability. The results of Chapter 4 are expected to be used as information for interpreting observed biogeochemical change and variability associated with global warming and climate mode.

Ten-odd years after the start of the International Argo program of the 2000s, numerous profiles obtained and accumulated by the program show us the many new pictures of the ocean and provide us many findings and knowledge. Recently, Biogeochemical Argo (BGC Argo: Johnson et al. 2009) floats that added biogeochemical property sensors (oxygen, chlorophyll, etc.) to regular temperature/conductivity sensors is becoming widespread. In the next decade, as the drastic increase in the biogeochemical data due to the establishment of BGC Argo observation web, it is expected that we will be able to know and investigate the physical-biogeochemical interactions with denser and broader spatiotemporal coverage about from observational data. We believe, in the near future, that the present results are facilitate advances in understanding of not only the ocean's thermal role in the climate system but also its roles in the ecological system and material cycle in the earth system.

References

Akima, H. (1970). A new method of interpolation and smooth curve fitting based on local procedures. Journal of the Association for Computing Machinery, 17, 589–602. https://doi.org/10.1145/321607.321609

Argo (2000). Argo float data and metadata from Global Data Assembly Centre (Argo GDAC). SEANOE. http://doi.org/10.17882/42182

Behrenfeld, M. J., O'Malley, R. T., Siegel, D. A., McClain, C. R., Sarmiento, J. L., Feldman, G. C., Milligan, A. J., Falkowski, P. G., Letelier, R. M., & Boss, E. S. (2006). Climate-driven trends in contemporary ocean productivity. Nature, 444, 752–755. https://doi.org/10.1038/nature05317

Bonjean, F., & Lagerloef, G. S. E. (2002). Diagnostic Model and Analysis of the Surface Currents in the Tropical Pacific Ocean. Journal of Physical Oceanography, 32, 2938–2954. https://doi.org/10.1175/1520-0485(2002)032<2938:DMAAOT>2.0.CO;2

Boyer, T. P., Antonov, J. I., Baranova, O. K., Coleman, C., Garcia, H. E., Grodsky, A., Johnson, D. R., Locarnini, R. A., Mishonov, A. V., O'Brien, T. D., Paver, C. R., Reagan, J. R., Seidov, D., Smolyar, I. V., & Zweng, M. M. (2013). World Ocean Database 2013. S. Levitus, Ed.; A. Mishonov, Technical Ed.; NOAA Atlas NESDIS, 72, 209 pp.

Burchard, H., & Hofmeister, R. (2008). A dynamic equation for the potential energy anomaly for analysing mixing and stratification in estuaries and coastal seas. Estuarine, Coastal and Shelf Science, 77, 679–687. https://doi.org/10.1016/j.ecss.2007.10.025

Cabré, A., Marinov, I., & Leung, S. (2015). Consistent global responses of marine ecosystems to future climate change across the IPCC AR5 earth system models. Climate Dynamics, 45, 1253–280. https://doi.org/10.1007/s00382-014-2374-3

Capotondi, A., Alexander, M. A., Bond, N. A., Curchitser, E. N., & Scott, J. D. (2012). Enhanced upper ocean stratification with climate change in the CMIP3 models. Journal of Geophysical Research; Oceans, 117, C04031. http://doi.org/10.1029/2011JC007409

Chen, D., Busalacchi, A. J., & Rothstein, L. M. (1994). The roles of vertical mixing, solar radiation, and wind stress in a model simulation of the sea surface temperature seasonal cycle in the tropical Pacific Ocean. Journal of Geophysical Research: Oceans, 99, 20345–20359. https://doi.org/10.1029/94JC01621

Chiba, S., Ono, T., Tadokoro, K., Midorikawa, T., & Saino, T. (2004). Increased stratification and decreased lower trophic level productivity in the Oyashio region of the North Pacific: A 30-year retrospective study. Journal of Oceanography, 60, 149–162. https://doi.org/10.1023/B:JOCE.0000038324.14054.cf

Cronin, M. F., Bond, N. A., Farrar, J. T., Ichikawa, H., Jayne, S. R., Kawai, Y., Konda, M., Qiu, B., Rainville, L., & Tomita, H. (2013). Formation and erosion of the seasonal thermocline in the Kuroshio Extension recirculation gyre. Deep Sea Research, Part II, 85, 62–74. https://doi.org/10.1016/j.dsr2.2012.07.018

Cronin, M. F., Pelland, N. A., Emerson, S. R., & Crawford, W. R. (2015). Estimating diffusivity from the mixed layer heat and salt balances in the North Pacific. Journal of Geophysical Research: Oceans, 120, 7346–7362. https://doi.org/10.1002/ 2015JC011010

Czaja, A., & Hausmann, U. (2009). Observations of entry and exit of potential vorticity at the sea surface. Journal of Physical Oceanography, 39, 2280–2294. https://doi.org/10.1175/2009JPO4024.1

Dale, T., Rey, F., & Heimdal, B. R. (1999). Seasonal development of phytoplankton at a high latitude oceanic site. Sarsia, 84, 419–435. https::/doi.org/10.1080/00364827.1999.10807347

Dave, A. C., & Lozier, M. S. (2013). Examining the global record of interannual variability in stratification and marine productivity in the low-latitude and mid-latitude ocean. Journal of Geophysical Research; Oceans, 118, 3114–3127. https://doi.org/10.1002/jgrc.20224

Dee, D. P., Uppala, S. M., Simmons, A. J., Berrisford, P., Poli, P., Kobayashi, S., Andrae, U., Balmaseda, M. A., Balsamo, G., Bauer, P., Bechtold, P., Beljaars, A. C. M., van de Berg, L., Bidlot, J., Bormann, N., Delsol, C., Dragani, R., Fuentes, M., Geer, A. J., Haimberger, L., Healy, S. B., Hersbach, H., Hólm, E. V., Isaksen, L., Kållberg, P., Köhler, M., Matricardi, M., McNally, A. P., Monge-Sanz, B. M., Morcrette, J.-J., Park, B.-K., Peubey, C., de Rosnay, P., Tavolato, C., Thépaut, J.-N., & Vitart, F. (2011). The ERA-Interim reanalysis: Configuration and performance of the data assimilation system.Quarterly Journal of the Royal Meteorological Society,137,553–597. https://doi.org/10.1002/qj.828

Deremble, B., & Dewar, W. K. (2012). First-order scaling law for potential vorticity extraction due to wind. Journal of Physical Oceanography, 42, 1303–1312. https://doi.org/10.1175/JPO-D-11-0136.1

Deremble, B., Wienders, N., & Dewar, W. K. (2014). Potential vorticity budgets in the North Atlantic Ocean. Journal of Physical Oceanography, 44, 164–178. https://doi.org/10.1175/JPO-

D-13-087.1

Doney, S. C. (2006). Plankton in a warmer world. Nature, 444, 695–696. https://doi.org/10.1038/444695a

Durack, P. J., & Wijffels, S. E. (2010). Fifty-year trends in global ocean salinities and their relationship to broad-scale warming. Journal of Climate, 23, 4342–4362. https://doi.org/10.1175/2010JCLI3377.1

Fu, W., Randerson, J. T., & Moore, J. K. (2016). Climate change impacts on net primary production (NPP) and export production (EP) regulated by increasing stratification and phytoplankton community structure in the CMIP5 models. Biogeosciences, 13, 5151–5170. https://doi.org/10.5194/bg-13-5151-2016

Furuichi, N., Hibiya, T., & Niwa, Y. (2008). Model-predicted distribution of wind-induced internal wave energy in the world's oceans. Journal of Geophysical Research: Oceans, 113, C09034. https://doi.org/10.1029/2008JC004768

Giglio, D., & Roemmich, D. (2014). Climatological monthly heat and freshwater flux estimates on a global scale from Argo. Journal of Geophysical Research: Oceans, 119, 6884–6899. https://doi.org/10.1002/2014JC010083

Goh, G., & Noh, Y. (2013). Influence of the Coriolis force on the formation of a seasonal thermocline. Ocean Dynamics, 63, 1083–1092. https://doi.org/10.1007/s10236-013-0645-x

Good, S. A., Martin, M. J., & Rayner, N. A. (2013). EN4: quality controlled ocean temperature and salinity profiles and monthly objective analyses with uncertainty estimates. Journal of Geophysical Research: Oceans, 118, 6704–6716. https://doi.org/10.1002/2013JC009067

Gronholz, A., Gräwe, U., Paul, A., & Schulz, M. (2017). Investigating the effects of a summer storm on the North Sea stratification using a regional coupled ocean-atmosphere model. Ocean Dynamics, 67, 211–235. https://doi.org/10.1007/s10236-016-1023-2

Haynes, P. H., & McIntyre, M. E. (1987). On the evolution of vorticity and potential vorticity in the presence of diabatic heating and frictional or other forces. Journal of the Atmospheric Science, 44, 828–841. https://doi.org/10.1175/1520-0469(1987)044%3C0828:OTEOVA%3E2.0.CO;2

Hosoda, S., Suga, T., Shikama, N., & Mizuno, K. (2009). Global surface layer salinity change detected by Argo and its implication for hydrological cycle intensification. Journal of Oceanography, 65, 579–586. https://doi.org/10.1007/s10872-009-0049-1

Hosoda, S., Nonaka, M., Tomita, T., Taguchi, B., Tomita, H., & Iwasaka, N. (2015). Impact of downward heat penetration below the shallow seasonal thermocline on the sea surface temperature. Journal of Oceanography, 46, 1–16. https://doi.org/10.1007/s10872-015-0275-7

Huang, Y., Li, T., & Wu, B. (2018). Why SST trend in North Pacific is peculiarly negative against warming trend elsewhere since 1958. Climate Dynamics, (in press). https://doi.org/10.1007/s00382-018-4389-7

Huffman, G. J., Adler, R. F., Morrissey, M. M., Bolvin, D. T., Curtis, S., Joyce, R., McGavock, B., & Susskind, J. (2001). Global precipitation at one-degree daily resolution from multisatellite observations. Journal of Hydrometeorology, 2, 36–50. https://doi.org/10.1175/1525-7541(2001)002<0036:GPAODD>2.0.CO;2

Hughes, W. C., & de Cuevas, B. A. (2001). Why western boundary currents in realistic oceans are inviscid: A link between form stress and bottom pressure torques. Journal of Physical Oceanography, 31, 2871–2885. https://doi.org/10.1175/1520-0485(2001)031<2871:WWBCIR>2.0.CO;2

Hurrell, J. W. (2003). NAO Index Data provided by the Climate Analysis Section, NCAR, Boulder, USA, Updated regularly. Accessed 20 August 2018 [Annual North Atlantic Oscillation Index (Station-based)].

Jerlov, N. G. (1968). Optical Oceanography. Elsevier, 194 pp.

Jochum, M., Briegleb, B. P., Danabasoglu, G., Large, W. G., Norton, N. J., Jayne, S. R., Alford, M. H., & Bryan, F. O. (2013). The impact of oceanic near-inertial waves on climate, Journal of Climate, 26, 2833–2844. https://doi.org/10.1175/JCLI-D-12-00181.1

Johnson, K.S., Berelson, W.M., Boss, E.S., Chase, Z., Claustre, H., Emerson, S.R., Gruber, N., Körtzinger, A., Perry, M.J., & Riser, S.C. (2009). Observing biogeochemical cycles at global scales with profiling floats and gliders: Prospects for a global array. Oceanography, 22, 216–225. https://doi:10.5670/oceanog.2009.81

Johnston, T. M. S., & Rudnick, D. L. (2009). Observations of the transition layer. Journal of Physical Oceanography, 39, 780–797. https://doi.org/10.1175/2008JPO3824.1

Joyce, T. M. (2012). New perspectives on eighteen-degree water formation in the North Atlantic. Journal of Oceanography, 68, 45–52. https://doi.org/10.1007/s10872-011-0029-0

Kako, S., & Kubota, M. (2007). Variability of mixed layer depth in Kuroshio/Oyashio Extension region: 2005–2006. Geophysical Research Letter, 34, L11612. https://doi.org/10.1029/2007GL030362

Lee, E., Noh, Y., Qiu, B., & Yeh, S.-W. (2015). Seasonal variation of the upper ocean responding to surface heating in the North Pacific. Journal of Geophysical Research: Oceans, 120, 5631–5647. https://doi.org/10.1002/2015JC010800

Lee, Z., Du, K., Arnone, R., Liew, S., & Penta, B. (2005). Penetration of solar radiation in the upper ocean: A numerical model for oceanic and coastal waters. Journal of Geophysical Research: Oceans, 110, C09019. https://doi.org/10.1029/2004JC002780

Levitus, S., Antonov, J. I., Boyer, T. P., Locarnini, R. A., Garcia, H. E., & Mishonov, A.V. (2009). Global ocean heat content 1955–2008 in light of recently revealed instrumentation problems. Geophysical Research Letters, 36, L07608. https://doi.org/10.1029/2008GL037155

Luyten, J. R., Pedlosky, J., & Stommel, H. (1983). The ventilated thermocline. Journal of Physical Oceanography. 13, 292–309. https://doi.org/10.1175/1520-0485(1983)013%3C0292:TVT%3E2.0.CO;2

Maes, C., & O'Kane, T. J. (2014). Seasonal variations of the upper ocean salinity stratification in the Tropics. Journal of Geophysical Research: Oceans, 119, 1706–1722. https://doi.org/10.1002/2013JC009366

Mantua, N. J., Hare, S. R., Zhang, Y., Wallace, J. M., & Francis, R. C. (1997). A Pacific interdecadal climate oscillation with impacts on salmon production. Bulletin of the American Meteorological Society, 78, 1069–1079. https://doi.org/10.1175/1520-0477(1997)078<1069:APICOW>2.0.CO;2

Marshall, J. C. (1984). Eddy-mean flow interaction in a barotropic ocean model. Quarterly Journal of the Royal Meteorological Society, 110, 573–590. https://doi.org/10.1002/qj.49711046502

Marshall, J. C., Jamous, D., & Nilsson, J. (2001). Entry, flux, and exit of potential vorticity in ocean circulation. Journal of Physical Oceanography, 31, 777–789. https://doi.org/10.1175/1520-0485(2001)031%3C0777:EFAEOP%3E2.0.CO;2

Marshall, J. C., & Nurser, A. J. G. (1992). Fluid dynamics of oceanic thermocline ventilation. Journal of Physical Oceanography, 22, 583–595. https://doi.org/10.1175/1520-0485(1992)022%3C0583:FDOOTV%3E2.0.CO;2

Maze, G., Forget, G., Buckley, M., Marshall, J., and Cerovecki, I. (2009). Using transformation and formation maps to study the role of air–sea heat fluxes in North Atlantic Eighteen Degree

Water formation. Journal of Physical Oceanography, 39, 1818–1835. https://doi.org/10.1175/2009JPO3985.1

Maze, G., & Marshall, J. (2011). Diagnosing the observed seasonal cycle of Atlantic subtropical mode water using potential vorticity and its attendant theorems. Journal of Physical Oceanography, 41, 1986–1999. https://doi.org/10.1175/2011JPO4576.1

Moisan, J. R., & Niiler, P. P. (1998). The seasonal heat budget in the North Pacific: net heat flux and heat storage rates (1950–1990). Journal of Physical Oceanography, 28, 401–420. https://doi.org/10.1175/1520-0485(1998)028<0401:TSHBOT>2.0.CO;2

Monterey, G., & Levitus, S. (1997). Seasonal Variability of Mixed Layer Depth for the World Ocean. NOAA Atlas NESDIS, 14, 100 pp.

NASA Goddard Space Flight Center, Ocean Ecology Laboratory, Ocean Biology Processing Group (2014). Moderate-resolution Imaging Spectroradiometer (MODIS) Aqua Inherent Optical Properties Data; 2014 Reprocessing. NASA OB.DAAC, Greenbelt, MD, USA. https://doi.org/10.5067/AQUA/MODIS/L3B/IOP/2014

Newman, M., Alexander, M. A., Ault, T. R., Cobb, K. M., Deser, C., Di Lorenzo, E., Mantua, N. J., Miller, A. J., Minobe, S., Nakamura, H., Schneider, N., Vimont, D. J., Phillips, A. S., Scott, J. D., & Smith, C. A. (2016). The Pacific Decadal Oscillation, revisited. Journal of Climate, 29, 4399–4427. https://doi.org/10.1175/JCLI-D-15-0508.1

Oka, E., & Qiu, B. (2012). Progress of North Pacific mode water research in the past decade. Journal of Oceanography, 68, 5–20. https://doi.org/10.1007/s10872-011-0032-5

Oka, E., Qiu, B., Takatani, Y., Enyo, K., Sasano, D., Kosugi, N., Ishii, M., Nakano T., & Suga, T. (2015). Decadal variability of subtropical mode water subduction and its impact on biogeochemistry. Journal of Oceanography, 71, 389–400. https://doi.org/10.1007/s10872-015-0300-x

Olsina, O., Wienders, N., & Dewar, W. K. (2013). An estimate of the climatology and variability of Eighteen Degree Water potential vorticity forcing. Deep Sea Research, Part II, 91, 84–95. https://doi.org/10.1016/j.dsr2.2013.02.018

Paulson, C. A., & Simpson, J. J. (1977). Irradiance measurements in the upper ocean. Journal of Physical Oceanography, 7, 952–956. https://doi.org/10.1175/1520-0485(1977)007<0952:IMITUO>2.0.CO;2

Qiu, B., & Chen, S. (2006). Decadal variability in the formation of the North Pacific Subtropical

Mode Water: Oceanic versus atmospheric control. Journal of Physical Oceanography, 36, 1365–1380. https://doi.org/10.1175/JPO2918.1

Qiu, B., Chen, S., & Hacker, P. (2004). Synoptic-scale air–sea flux forcing in the western North Pacific: Observations and their impact on SST and the mixed layer. Journal of Physical Oceanography, 34, 2148–2159. https://doi.org/10.1175/1520-0485(2004)034<2148:SAFFIT>2.0.CO;2

Qiu, B., Hacker, P., Chen, S., Donohue, K. A., Watts, D. R., Mitsudera, H., Hogg, N. G., & Jayne, S. R. (2006). Observations of the Subtropical Mode Water evolution from the Kuroshio Extension System Study. Journal of Physical Oceanography, 36, 457–473. https://doi.org/10.1175/JPO2849.1

Qiu, B., & Huang, R.X. (1995). Ventilation of the North Atlantic and North Pacific: subduction versus obduction. Journal of Physical Oceanography, 25, 2374–2390. https://doi.org/10.1175/1520-0485(1995)025%3C2374:VOTNAA%3E2.0.CO;2

Qiu, B., & Kelly, K.A. (1993). Upper ocean heat balance in the Kuroshio Extension region. Journal of Physical Oceanography, 23, 2027–2041. https://doi.org/10.1175/1520-0485(1993)023<2027:UOHBIT>2.0.CO;2

Rayner, N. A., Parker, D. E., Horton, E. B., Folland, C. K., Alexander, L. V., Rowell, D. P., Kent, E. C., Kaplan, A. (2003). Global analyses of sea surface temperature, sea ice, and night marine air temperature since the late nineteenth century. Journal of Geophysical Research: Atmospheres, 108, D14, 4407. https://doi.org/10.1029/2002JD002670

Ren, L., & Riser, S. C. (2009). Seasonal salt budget in the northeast Pacific Ocean. Journal of Geophysical Research: Oceans, 114, C12004. https://doi.org/10.1029/2009JC005307

Rhein, M., Rintoul, S. R., Aoki, S., Campos, E., Chambers, D., Feely, R. A., Gulev, S., Johnson, G. C., Josey, S. A., Kostianoy, A., Mauritzen, C., Roemmich, D., Talley, L. D., & Wang, F. (2013). Observations: Ocean. In Stocker, T.F. et al. (Eds.), Climate Change 2013: The Physical Science Basis. Contribution of Working Group I to the Fifth Assessment Report of the Intergovernmental Panel on Climate Change. Cambridge University Press, Cambridge, United Kingdom and New York, NY, USA.

Riser, S. C., Freeland, H. J., Roemmich, D., Wijffels, S., Troisi, A., Belbeoch, M., Gilbert, D., Xu, J., Pouliquen, S., Thresher, A., Le Traon, P.-Y., Maze, G., Klein, B., Ravichandran, M., Grant, F., Poulain, P.-M., Suga, T., Lim, B., Sterl, A., Sutton, P., Mork, K.-A., Velez-Belchi,

P. J., Ansorge, I., King, B., Turton, J., Baringer, M., & Jayne, S. (2016) Fifteen years of ocean observations with the global Argo array, Nature Climate Change, 6, 145–153. https://doi.org/10.1038/nclimate2872

Roemmich, D., & Gilson, J. (2009). The 2004–2008 mean and annual cycle of temperature, salinity, and steric height in the global ocean from the Argo Program. Progress in Oceanography, 82, 81–100. https://doi.org/10.1016/j.pocean.2009.03.004

Saji, N. H., Goswami, B. N., Vinayachandran, P. N., & Yamagata, T. (1999). A dipole mode in the tropical Indian Ocean. Nature, 401, 360–363. https://doi.org/10.1038/43854

Schulenberger, E., & Reid, J. L. (1981). The Pacific shallow oxygen maximum, deep chlorophyll maximum, and primary productivity reconsidered, Deep Sea Research, Part A, 28, 901–919. https://doi.org/10.1016/0198-0149(81)90009-1

Singh, A., Delcroix, T., & Cravatte, S. (2011). Contrasting the flavors of El Niño and Southern Oscillation using sea surface salinity observations. Journal of Geophysical Research; Oceans, 116, C06016. https://doi.org/10.1029/2010JC006862

Simpson, J. H. (1981). The shelf-sea fronts: implications of their existence and behavior. Philosophical Transactions of the Royal Society A, 302, 531–546. https://doi.org/10.1098/rsta.1981.0181

Somavilla, R., González-Pola, C., & Fernández-Diaz, J. (2017). The warmer the ocean surface, the shallower the mixed layer. How much of this is true? Journal of Geophysical Research: Oceans, 122, 7698–7716. https://doi.org/10.1002/2017JC013125

Suga, T., Aoki, Y., Saito, H., & Hanawa, K. (2008). Ventilation of the North Pacific subtropical pycnocline and mode water formation. Progress in Oceanography, 77, 285–297. https://doi.org/10.1016/j.pocean.2006.12.005

Suga, T., & Hanawa, K. (1995). Interannual variations of North Pacific Subtropical Mode Water in the 137°E section. Journal of Physical Oceanography, 25, 1012–1017. https://doi.org/10.1175/1520-0485(1995)025%3C1012:IVONPS%3E2.0.CO;2

Suga, T., Hanawa, K., and Toba, Y. (1989). Subtropical mode water in the 137°E section. Journal of Physical Oceanography, 19, 1605–1618. https://doi.org/10.1175/1520-0485(1989)019%3C1605:SMWITS%3E2.0.CO;2

Suga, T., Motoki, K., Aoki, Y., & MacDonald, A. M. (2004). The North Pacific climatology of winter mixed layer and mode waters. Journal of Physical Oceanography, 34, 3–22. https://doi.org/10.1175/1520-0485(2004)034<0003:TNPCOW>2.0.CO;2

Sugimoto, S., Hanawa, K., Watanabe, T., Suga, T., & Xie, S.-P. (2017). Enhanced warming of the subtropical mode water in the North Pacific and North Atlantic. Nature Climate Change, 7, 656–658. https://doi.org/10.1038/nclimate3371

Sugimoto, S., & Kako, S. (2016) Decadal variation in winter mixed layer depth south of the Kuroshio Extension and its influence on winter mixed layer temperature. Journal of Climate, 29,1237–1252. https://doi.org/10.1175/JCLI-D-15-0206.1

Sukigara, C., Suga, T., Saino, T., Toyama, K., Yanagimoto, D., Hanawa, K., & Shikama, N. (2011). Biogeochemical evidence of large diapycnal diffusivity associated with the Subtropical Mode Water of the North Pacific. Journal of Oceanography, 67, 77–85. https://doi.org/10.1007/s10872-011-0008-5

Talley, L. D. (1988). Potential vorticity distribution in the North Pacific. Journal of Physical Oceanography, 18, 89–106. https://doi.org/10.1175/1520-0485(1988)018%3C0089:PVDITN%3E2.0.CO;2

Tokinaga, H., Xie, S.-P., Timmermann, A., McGregor, S., Ogata T., Kubota, H., & Okumura, Y. M. (2012). Regional patterns of tropical Indo-Pacific climate change: Evidence of the Walker circulation weakening. Journal of Climate, 25, 1689–1710. https://doi.org/10.1175/JCLI-D-11-00263.1

Tomita, H., Hihara, T., Kako, S., Kubota, M., and Kutsuwada, K. (2018). An introduction to J-OFURO3, a third-generation Japanese ocean flux data set using remote-sensing observations. Journal of Oceanography, (in press). https://doi.org/10.1007/s10872-018-0493-x

Tomita, H., Kako, S., Cronin, M. F., & Kubota, M. (2010). Preconditioning of the wintertime mixed layer at the Kuroshio Extension Observatory. Journal of Geophysical Research: Oceans, 115, C12053. https://doi.org/10.1029/2010JC006373

Toyoda, T., Awaji, T., Masuda, S., Sugiura, N., Igarashi, H., Mochizuki, T., & Ishikawa, Y. (2011). Interannual variability of North Pacific eastern subtropical mode water formation in the 1990s derived from a 4-dimensional variational ocean data assimilation experiment. Dynamics of Atmospheres and Oceans, 51, 1–25. http://dx.doi.org/10.1016/j.dynatmoce.2010.09.001

Trenberth, K. E. (1997). The definition of El Niño. Bulletin of the American Meteorological Society, 78, 2771–2777. https://doi.org/10.1175/1520-0477(1997)078<2771:TDOENO>2.0.CO;2

Trenberth, K. E., & Hoar, T. J. (1996). The 1990–1995 El Niño-Southern Oscillation event:

Longest on record. Geophysical Research Letters, 23, 57–60. https://doi.org/10.1029/95GL03602

Vallis, G. K. (2006). Atmospheric and Oceanic Fluid Dynamics. Cambridge University Press, 745 pp.

Visbeck, M., Chassignet, E. P., Curry, R. G., Delworth, T. L., Dickson, R. R., & Krahmann, G. (2003). The ocean's response to North Atlantic Oscillation variability. In J. W. Hurrell et al. (Eds.), The North Atlantic Oscillation: Climatic Significance and Environmental Impact (pp. 113–145). Washington, DC: American Geophysical Union. https://doi.org/10.1029/134GM06

Vivier, F., Kelly, K. A., & Thompson, L. (2002). Heat budget in the Kuroshio Extension Region: 1993–99. Journal of Physical Oceanography, 32, 3436–3454. https://doi.org/10.1175/1520-0485(2002)032<3436:HBITKE>2.0.CO;2

Watanabe, Y., Ishida, H., Nakano, T., & Nagai, N. (2005). Spatiotemporal decreases of nutrients and chlorophyll-a in the surface mixed layer of the western North Pacific from 1971 to 2000. Journal of Oceanography, 61, 1011–1016. https://doi.org/10.1007/s10872-006-0017-y

Xiu, P., & Chai, F. (2014). Connections between physical, optical and biogeochemical processes in the Pacific Ocean. Progress in Oceanography, 122, 30–53. https://doi.org/10.1016/j.pocean.2013.11.008

Yamaguchi, R. (2016). Evolution and spatiotemporal variations of seasonal pycnocline in the North Pacific (Japanese). Master thesis in Tohoku university, 102pp.

Yoshikawa, Y. (2015). Scaling surface mixing/mixed layer depth under stabilizing buoyancy flux. Journal of Physical Oceanography, 45, 247–258, https://doi.org/10.1175/JPO-D-13-0190.1

Yu, L., Jin, X., & Weller, R. A. (2008). Multidecade global flux datasets from the objectively analyzed air-sea fluxes (OAFlux) project: Latent and sensible heat fluxes, ocean evaporation, and related surface meteorological variables. Woods Hole Oceanographic Institution OAFlux Project Technical Report OA-2008-01, Wood Hole, MA: Woods Hole Oceanographic Institution.

Zhang, R-H, Chen, D., & Wang, G. (2011). Using Satellite ocean color data to derive an empirical model for the penetration depth of solar radiation (H_p) in the Tropical Pacific Ocean. Journal of Atmospheric and Oceanic Technology, 28, 944–965. https://doi.org/10.1175/2011JTECHO797.1

Zoffoli, M. L., Lee, Z., Ondrusek, M., Lin, J., Kovach, C., Wei, J., & Lewis, M. (2017). Estimation of transmittance of solar radiation in the visible domain based on remote sensing: Evaluation of models using in situ data. Journal of Geophysical Research: Oceans, 122, 9176–9188. https://doi.org/10.1002/2017JC013209